

©2009

Sombun Reantragoon

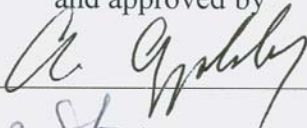
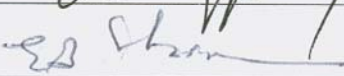
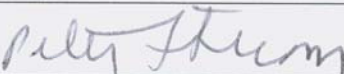
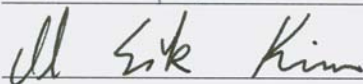
ALL RIGHTS RESERVED

RADON DETECTION :
THE INFLUENCE OF HUMIDITY
By SOMBUN REANTRAGOON

A dissertation submitted to the
Graduate School – New Brunswick
Rutgers, The State University of New Jersey
In partial fulfillment of the requirements
for the degree of
Doctor of Philosophy
Graduate Program in Environmental Sciences

Written under the direction of
Professor Alan Appleby

and approved by

New Brunswick, New Jersey

January, 2009

ABSTRACT OF THE DISSERTATION

Radon Detection: the influence of Humidity

by SOMBUN REANTRAGOON

Dissertation Director: Professor Alan Appleby

The fundamental aim of this doctoral research was to determine the influence of water in the form of Humidity (% of water in air) on Radon detection. The basic hypothesis assumes that the amount of water molecules present in the air, attached to the radon molecules, has an influence on radon detection. A correlation can be determined between the model of water behavior and the level of radon detection - the higher the correlation the higher the influence, the lower the correlation the lower the influence.

In order to control, change and measure the input variables and accurately measure the data output, the research was conducted in the laboratory, in a closed loop environment. The equipment used was modified to ensure the integrity of the collected data and multiple experiments were conducted over a period of time. Radon was measured by a fiber-optic scintillating detector and radon ion (+) was measured by air-ion counters. The amount of radon ion attached to the wall of the detector compartment ranged from 1.38 – 5.74% of the initial total flow through the system.

The data produced by the experiments of count per minute of radon, relative humidity, temperature and dew-point was analyzed using SYSTAT software. Several analytical approaches were applied and it was determined that graphs gave the best fit. The data was normalized to minimize variations (such as the different time of the build up of the radon in

the source), between the experiments. In this way experimental data could be compared, collated and analyzed.

A model of the water behavior was needed as a base for the research. The One Function X, One Function Y Standard Subset Equation was selected, with $z = a + b \ln x + cy$, because it has a best degree of fitness equal to 0.995. The same equation, applied to the experimental data produced a degree of best fitness of 0.137. The research indicates that radon measurement is significantly influenced by water, in the form of humidity.

ACKNOWLEDGEMENTS

Completion of this dissertation would not have been possible without the tremendous support and valuable insight of my supervisors. I am truly indebted to these special mentors and to the Environmental and Radiation Science Department at Rutgers University.

I would like to express my sincere gratitude to Professor Alan Appleby. His many years of experience in the field of Radiation Science enabled him to provide expert guidance and to make suggestions on research development. Professor Appleby was a constant adviser and his dedication was demonstrated by the fact that, although he retired from the position of Head of the Radiation Science Department prior to the completion of my work, he continued to be an active and engaged supervisor. During our meetings he always had positive encouragement and constructive suggestions.

Special thanks are also given to Professor Edward Christman for inspiring me to continue to focus time and energy on this research. Whilst the challenges were demanding Professor Christman was confident that the results would prove significant. He always had kind words and was totally supportive of me continuing to achieve my goals.

I very much appreciated the support and well-thought through suggestions provided by Professor Peter Strom. He was always generous with his time and willingness to accommodate this research. When Professor Appleby retired, Professor Strom readily assumed the responsibility for administration and compliance, for which I am very grateful.

I am also deeply indebted to Dr IL Sik Kim for his feedback and valuable time. The late night hours we spent together in the laboratory, working on enhancements and repairs to the equipment, significantly progressed the research. His knowledge of the topic and his first-hand experience of the detector was a huge benefit. I am grateful for his advice and expertise in this specific field.

In addition, because of the care and sacrifice of my father and mother - Mr Dao T Lim and Mrs Lun Lim, I had the opportunity to further my education and study abroad. This is a priceless gift. I would also like to thank my sister, Mrs Nuansmorn R Hwang, for her initial support of my studies abroad.

Finally I would like to thank my wonderful wife, Annette, who has the patience of a saint and who supported me throughout the time spent on my experiment and the writing of this dissertation. Without her understanding I would not have been able to dedicate time and energy into this research.

TABLE OF CONTENTS

	Page
Title	i
Abstract	ii
Acknowledgements	iv
Table of Contents	vi
List of Tables	x
List of Figures	xi
CHAPTER 1 Introduction	
1.1 Outline of the dissertation	1
1.2 Interaction of radon and water	3
1.3 Hypothesis statement	10
CHAPTER 2 Radon and Its Progeny Coefficients	
2.1 Radon diffusion coefficients	13
2.2 Radon exhalation rate	16
2.3 Radon permeability coefficient	18
2.4 Radon emanation coefficient	20
CHAPTER 3 Properties of Radon Affected by Temperature and Humidity	
3.1 Basic equations of temperature, humidity and dew point temperature	29
3.2 Radon solubility in water	31
CHAPTER 4 Biological Effects of Radon and Radon Progeny	
4.1 Mechanisms of airborne particles	38
4.2 Radon in the respiratory system	42
4.3 ICRP model of radon particle size distribution in the respiratory system	47

CHAPTER 5 Measurement of Radon by the Fiber Optic Scintillating Detector	
5.1 The fiber optic scintillating detector	52
5.2 The radon source (Pylon), the Humidity flask, & the Dryer (Dehumidifier)	54
5.3 The MultiChannel Analyzer (MCA)	54
5.4 Preamplifier for the PM of the Detector	56
5.5 The connection of the system	57
5.6 Operational and Data Collection	60
5.7 Modeling and Data Analysis	62
CHAPTER 6 Air Ions Measurement	
6.1 The basic design of the Gerdien tube detector	69
6.2 Operation and data collection	74
6.3 Data Analysis	75
CHAPTER 7 Discussion and Conclusions	
7.1 Discussion	80
7.2 Conclusions	86
Appendix A Basic Information of Radon	89
Figure A.1 Gas Transmission Path of Rn (pressure =155.14)	91
Figure A.2 Ionization enery (eV) of the outer electron in various elements	91
Figure A.3 Henry's constant of Inert Gases vs Temperature °C	92
Figure A.4 Solubility of Inert Gases vs Temperature °C	92
Figure A.5 Atomic diameter and eV of Inert Gases	93
Figure A.6 Decomposition of hydrate forming in Inert gas-water system	93

Appendix B The Diffusive Transport	94
Table B.1 Gaussian error function erf(z) & Complimentary error function erfc (z)	97
Figure B.1 Gaussian error function erf(z) & Complimentary error function erfc (z)	98
Appendix C Scattering angle and impact parameter (b) of the alpha particle (5.489MeV)	
Table C.1 Scattering angle of the alpha particle (5.489MeV)	99
Figure C.1 Alpha Scattering Impact Parameter as a function of Scattering Angle	100
Appendix D Van der Waal force by Lennard-Jones 6-12 Potential for small non-polar	
Molecules	101
Appendix E Properties of Inert Gases and water	
Table E.1 Properties of inert gas and water	106
Appendix F Properties of water	
Table F.1 Water vapor in air per dry air weight (Engineering Toolbox 2005)	108
Figure F.1 Water density as a function of Temperature in different humidities	109
Figure F.2 Water density as a function of Temperature (°C) 0 / 100 °C	110
Figure F.3 Water density as a function of Temperature (°C)	110
Figure F.4 4-D Pyramid of water vapor weight in grain per lb of air as a Function of relative humidity (%) temperature (°C) and dew point (°C)	111
Appendix G Command File and Output for Calculation of area under the peak of radon ion	
Figure G.1 Command File for calculation of are under the curve of radon ion	112
Figure G.2 Output for Calculation of area under the peak of radon ion	113
References	117
Vita	121

LIST OF TABLES

Table

2.1	The radon diffusion coefficients with different relative humidity (%)	18
2.2	The radon permeability coefficient of different materials	19
4.1	Lung $W_{T\text{ in}}$ from ICRP60 and Apportionment factors from ICRP66	48
4.2	SR_0 (Insoluble and non-reactive), SR_1 (Soluble or reactive), and SR_2 (Highly soluble or reactive) parameters	49
4.3	F, M and S Parameters	50
5.1	The setup parameter of ASA-100 in the PAMS software	55
5.2	Values of best fit (r^2) of water and radon	63
6.1	Area under the curve peak of radon ion	76
6.2	Adsorption of radon ion on the wall of the detector and passage	77

LIST OF FIGURES

Figure

1.1	Adsorption and Desorption of water	11
3.1	Radon Solubility change (%) per Temperature change (°C)	34
3.2	Ostwald Coefficient (K) vs Temperature (°C)	35
3.3	Radon Solubility in Water	37
5.1	Schematic of the equipment used in Radon measurement	58
5.2	Circuit of the Power Supply for the Preamplifier of the PM	59
5.3	Radon Measurement in different temperatures	65
5.4	Radon (cpm) by the fiber optic detector and ions (sec^{-1}) by the air ion counters in time (min)	66
5.5	Maximum Peak and Saturation Perk of Radon (cpm) at the beginning	67
5.6	Flow Diagram of Model	68
6.1	The basic design of the Gerdien Tube Method	69
6.2	The basic circuit of the Gerdien Tube Method	71
6.3	Distribution of radon measured by air ion counters	78

CHAPTER 1

Introduction

1.1 Outline of the dissertation

Radon can be measured using its ability to attach to scintillating glass fibers (Kim et al., 1995), but factors such as temperature, humidity, or solubility over the size and activity distribution of radon and its progeny, are not clearly correlated to the amount of radon being detected. The basic mechanism of this method of radon detection is such that radon attaches to water molecules in the air and it also adsorbs to the surface of materials such as the compartment walls of the detector. But the degree of attachment or the amount of adsorption depends on the amount of water in the air (see Figure 1.1, page 11). Based on this it can therefore be postulated that any detection or measurement of radon is influenced by humidity (the amount of water in the air).

Radon and the radon progeny are attached preferentially to the large aerosol particles present in the air, and under high humidity conditions the nucleation process can be shown to be facilitated by the presence of the positively charged radon progeny. A study on the measurement of growth in aerosol size and the change of activity distribution, by using kerosene combustion aerosol to change the aerosol sizes, showed that there was no change of aerosol size or activity distribution of radon and its progeny due to high humidity (Khan, Phillips and Duport, 1988). This is contradicted by the findings reported by Wilson (1900). Wilson suggested that the initiation of nucleation was reduced in the presence of ions in the supersaturated system.

An understanding of the properties and characteristics of radon behavior - such as solubility, diffusivity, the emanation coefficient and the exhalation rate of radon, is useful

as a basis for this research, for example in selecting the butyl rubber tubing for the experiment and knowing its diffusion length ($2 \times 10^{-3} \text{ m}$) (see section 2.1). These coefficients and parameters are reported in various literature and are described in Chapters 2 and 3.

In Chapter 2 the solubility of radon in water, or the Ostwald Coefficient, is confirmed to decrease by about 3% per °C (Surbeck, 1996), and it decreases with increasing temperature due to a hydrophobic effect (Kolomeisky and Widom, 1999). In Chapter 3 the fundamentals of humidity and temperature, based on dew points of air and details of radon solubility in water, are covered. The solubility of radon in water compared to the other inert gases is shown in Appendix E.

The biological effects of radon and the basic calculation of damages are considered, and the recommendation of the lung model by International Commission on Radiological Protection (ICRP), are reported in Chapter 4.

The increased awareness of radon ($^{222}\text{Rn}_{86}$) as a significant threat to public health makes it important to investigate the influences on detection further. Full details of the radon detection experiment are described in Chapter 5. The experiment, using a sensitive fiber optic scintillation detector (originally designed by Kim et al., 1995) in a closed system, is set up to measure radon in this research. The goal is to determine the influence of humidity (water in the air) and temperature on the measurements recorded by the scintillation detector.

Water behavior, based on the data of water vapor in dry air (Appendix F) was mathematically modeled [$Z = a + b \ln(X) + cY$] to get a best fit close to 1.0 (actual fit was $r^2 = 0.995$). The same mathematical model was then applied to the data from the

experiment, to determine the best degree of fitness. By comparison, the influence of humidity (water in air) and temperature could be determined.

Chapter 6 describes the measurement of radon ion by the Gerdien Tube method, using three air ion counters. Radon-laden air was measured at three locations within the closed loop: at the entrance to the fiber optic detector, at the exit of the fiber optic detector and at the entrance to the radon source. The amount of radon ion adsorbed to the wall and the inner surface of the fiber optic tubing and the varying amount of radon build-up over different time periods, could then be quantified.

Discussion and Conclusions are presented in Chapter 7. A four parameter, pyramid graph was utilized to show the results with radon measurement as a function of relative humidity, temperature and dew point temperature.

Basic information on radon is found in Appendix A. Appendix B details diffusive transport, based on Fick's Law. Appendix C gives the parameters of the alpha scattering. Appendix D summarizes the van der Waal force calculation for the interaction of small non-polar molecules (Lennard-Jones 6-12 potential) and the properties of inert gas and water are listed in Appendix E. Properties of water are summarized in Appendix F. The command file presented in Appendix G is for calculation of area under the curve (air ion counter).

1.2 Interaction of Radon and Water

An understanding of radon interaction with water is needed to determine the parameters which influence the measurements, or the means of measuring. The physical properties of radon are also required to understand the mechanism of radon behavior.

Some investigators suggest that the level of radon emerging from the ground depends upon the lunar period of the months, or the position of the earth's magnetic rotation.

Radon ($^{222}\text{Rn}_{86}$), shows unique chemical and physical properties, being the only member of the uranium-series that is an inert gas. Radon can be trapped in the lattice of the host substance during crystallization (Stein, 1983), even though there are no chemical bonds between radon and the surrounding host atoms. Radon can escape from the host lattice when the host crystal melts or dissolves into the solution due to the weakness of the van der Waals forces. The radon gas then randomly disperses into dry air.

The two most dominant diatomic components in dry air are oxygen (16 atomic unit mass) and nitrogen (14 atomic unit mass). The molecular mass of oxygen is 32 and the molecular mass of nitrogen is 28. Therefore dry air is denser than humid air, because the water vapor air is composed of one oxygen atom (16 atomic unit mass) and two hydrogen atoms (2 atomic unit mass). It can be shown that the density of water vapor per density of dry air has the factor of: $[1 + \text{specific humidity}] / [1 + 1.609(\text{Specific humidity})]$, at the same temperature (Engineering Toolbox, 2005). Radon atoms are experimentally shown to have very high solubility in water when compared with the other atoms of inert gases, at the same temperature and pressure. The solubility of radon in water decreases when the temperature is increased, due to the endothermic opening of a clathrate pocket in the water, and the exothermic placement of a molecule in that pocket by the multiple interaction of van der Waals interactions. The van der Waals interactions between the non-polar radon gas molecules and the large cluster of water provide the negative enthalpy change on dissolution (Chaplin, 2008). This results from attribution of the large negative entropy change by the structural enhancement of the water and the positive free

energy change. The structural enhancement factors include the fixing of the cluster center and the inner water shells surrounding the solute molecules. These interactions also cause the enhancement of the heat capacity (C_p) of the solution. Water is a polar molecule that tends to have a polarity shift which extensively opposes the alignment of the hydrogen-bonded network. This effect is known as permittivity of its dielectric constant which allows water to act as a solvent. On cooling, the water network strengthens and its dipole moments increase to compliment the dielectric of liquid water for the conversion to ice. The density increases as the temperature drops, reaching a maximum around 3-7°C, and then it decreases as the temperature drops below 4 °C (Figures F.2 and F.3 in Appendix F, page 110).

On heating, the dielectric constant of water decreases and liquid water becomes less polar and the density decreases due to broken hydrogen bonds or strong electric fields. A cluster of as many as 23-24 water molecules can attach to the radon atom in the first shell of solvation (Scharlin et al., 1998).

Radon is a colorless monatomic gas with a density of $9.727 \times 10^{-3} \text{ g/cm}^3$ under normal conditions in room temperature. Liquid radon is a colorless phosphorescent substance, with the density of 5.7 g/cm^3 (Avrorin et al., 1982). Radon has been studied and reported in the form of calthrate and hydrate compounds with 6 molecules of water. Radon can be in the form of clathrate compounds and complex halides (Stein, 1983) by reduction of oxidized radon in aqueous solutions. Radon can also be implanted into solids.

Radon is generally more soluble in organic liquids than in water. Theoretical calculations of the heat of formation of halides and oxides of the inert gases show that the other inert gases can not be formed into such compounds due to strongly endothermic

reactions that would be needed. Only radon fluoride is formed with a heat of formation of ~ 41.8 kJ/mole. A hydrate compound is formed in many inert gases (argon hydrate discovered by Villard P in 1896, and hydrates of krypton and xenon discovered by Forcrand R in 1925). In a similar way, hydrate formation between the molecules of radon and water was reported in the form of radon soluble in water. The solubility of radon in water was measured at low temperatures and found to be lowered with the presence of a variety of salts. The assumption of radon hydrate suggested that one molecule of radon was attached to 6 molecules of water as $\text{Rn}6\text{H}_2\text{O}$ with the dissociation pressure of 3.92×10^4 Pa.

The periodic table suggests that the Radon element is more ‘metallic’ than Xenon in terms of the ionic formation of radon difluoride. A quantum mechanical calculation also predicted the higher value of ionicity in the fluoride of $_{118}\text{Uuo}$ element (the next predicted inert gas) in comparison with the Radon ($_{86}\text{Rn}$). The observation of Radon halide suggested that radon is present as Rn^{+2} cations in the hydrolysis of halide compounds. The reaction of radon with the teflon, glass and metal material of the tube shows that the highest volatile product was teflon, and the next was glass, then lowest was metal. Treatment with electrical or microwave discharges caused fixation of radon on the walls of the quartz material possibly through the formation of very stable radonates or radon daughters.

Molecules or atoms of radon gas randomly travel within the volume and can be attached to the molecules of water by the van der Waal forces due to radon’s solubility property. Using a computerized program, based on the van der Waals radius, it was predicted that there would be up to 23.6 molecules of water (N) in the first solvation shell

surrounding the radon molecules from the solvent accessible surface (SAS) parameter (Scharlin et al., 1998). The parameters used in this model are surface areas (A_{ws} , A_{sas} , and A_{ses} in 10^{-20} m^2), and volumes (V_{ws} , V_{sas} , and V_{ses} in 10^{-30} m^3), which are derived from three surface models: van der Waals surface (WS), solvent accessible surface (SAS), and solvent-excluding surface (SES). The number of water molecules in the first solvation shell surrounding the gas molecules (N) is derived as the area of the Solvent accessible surface (A_{sas}) per the effective area occupied by a water molecule $(2r_w)^2$, where r_w is the van der Waals radius of water (0.14 nm or 1.4 Å). The regression equations of inert gases, below, are obtained between the thermodynamic parameters (changes in Gibbs energy ΔG° , enthalpy ΔH° , entropy ΔS° , and heat capacity ΔC_p° of gases in water) and the number of water molecules in the first solvation shell (N), as shown in kJ/mol

$$\Delta G^\circ = (-0.76 \pm 0.04)N + 39$$

$$\Delta H^\circ = (-2.0 \pm 0.3)N + 24 \quad (\text{using van't Hoff values and method})$$

$$T\Delta S^\circ = (-1.24 \pm 0.19)N - 16$$

The radon atoms can be packed into a fcc (face-centered cubic) type of lattice structure which are characterized by van der Waals molecular bonding. The average charge distribution in a single atom is spherically symmetric, which means the time-averaged dipole moment of the 1st radon atom is zero with respect to surrounding radon atoms or 2nd atom, $\langle \mu_1 \rangle = 0$, where $\langle \mu_1 \rangle$ is the time average of the dipole moment of the 1st radon atom (Tsymbal, 2008). There is a possibility that a non-zero dipole moment caused by fluctuations of the electronic charge distribution can take place at any moment of time. The dipole moment of the radon atom creates an electric field which also induces a dipole moment on the 2nd radon atom. This dipole moment is proportional to the electric field

(E) that is also inversely proportional to the cube of the separation distance between two radon atoms, r^3 , or $E \approx \frac{\mu_1}{r^3} \approx \mu_2$. Furthermore, the dipole moments of two radon atoms

interacting with each other causes the energy to be reduced from, $-\frac{\mu_1\mu_2}{r^3}$ to $-\frac{\mu_1^2}{r^6}$. The

coupling between the two dipoles results in 2 parts which are: the first part caused by a fluctuation, and the second part induced by the electric field, which is produced by the first one. This coupling provides the attractive force called the van der Waal force, even though $\langle \mu_1 \rangle$ is zero. The time averaged potential is determined by the average value of $\langle \mu_1^2 \rangle$ which does not vanish. Therefore the respective potential decreases with r^6 for a

relatively large separation between atoms, as $V \approx -\langle \frac{\mu_1^2}{r^6} \rangle \tilde{r} \approx \frac{-B}{r^6}$. At the small

separations a very strong repulsive force caused by the overlap of the inner electronic

shells start to dominate with the potential of the form $\frac{A}{r^{12}}$. The total potential energy of

two atoms can be represented as $V_{\text{total}} = 4\epsilon \left[\left(\frac{\sigma}{r} \right)^{12} - \left(\frac{\sigma}{r} \right)^6 \right]$, where $A = 4\epsilon\sigma^{12}$ and $B = 4\epsilon\sigma^6$.

This total potential energy is known as the Lennard-Jones potential (see Appendix D, page 101).

Water is a molecule composed of two atoms of hydrogen bonding with one oxygen atom in terms of sharing electrons, as a strong covalent bond H_2O . Water molecules as a whole have no net charge, but the hydrogen ends have a slight positive and the oxygen end has a slight negative charge caused by electrons on the side of the large oxygen nucleus. For this reason, water is a polar molecule with permanent dipole moment (μ , 1.85 Debye) because the oxygen atom has a higher electro-negativity than hydrogen. The

electrons are then more attracted to oxygen than to hydrogen so the partial charge distribution exists within the water molecules as a partial positive charge located at the center of two hydrogen atoms or positive charge called delta+ (δ^+). The partial negative charge called delta- (δ^-) is located on the oxygen atom. Therefore bonding between the molecules of water can occur as hydrogen bonds by the negative (oxygen) end of one water molecule bonding with the positive (hydrogen) end of another water molecule. Because of the bent nature of the water molecule, the center of the positive charge located at half way between the two hydrogen atoms does not coincide with the center of the negative charges of the oxygen atom. It is suggested that the molecular dipole moment between the center of the positive charge and the center of the negative charge is equivalent to a unit negative charge of one electron separated from a unit positive charge by 0.061 nm. The presence of this dipole moment in all water molecules causes its polar nature. The mean O-H length is about 0.097 nm with the mean H-O-H angle of 106° (Chaplin M, 2008). The mean negative charge on the oxygen atom is about 70% of an electron with each positively charged hydrogen atom sharing the neutralizing the charge. In general the angle between the hydrogen atoms of water is 104.45° and the distance between the oxygen and hydrogen atoms is 0.9584Angstrom.

The inter-molecular force is the result of δ^+ and δ^- interaction between hydrogen and oxygen molecules. This hydrogen bond is not as strong as the bonds holding the water molecule itself together, but the attraction of water molecules for each other is a very important factor in determining the properties of water. The attraction is very strong when the O-H bond from one water molecule aims directly at a nearby oxygen atom of

another water molecule to hold on to both O atoms (O-H O in the straight line called hydrogen bonding).

The intermolecular potential energy (V) as dipole-dipole interaction for water- water molecules is inversely proportional to $[\frac{3}{2kTr^6}]$, where k is the Boltzman constant, T is temperature, and r is the distance between the interacting particles or the distance between the particle and the center of the dipole.

The hydrogen bond strength, between the oxygen and hydrogen atoms in water, dictates the physical properties of water. As the strength reduces the viscosity and the density are decreased, but thermal conductivity and compressibility of water are increased. Adsorption (adhesion to the surface of the particle) and desorption (process of removing the sorbed substance) of water is illustrated in Figure 1.1 (page 11). At low water content and low water activity there is low water adsorption, the adsorption increases as the temperature and/or pressure increases. Desorption acts in reverse.

1.3 Hypothesis statement

The basic hypothesis assumes that the amount of water molecules present in the air, attached to the radon molecules, has an influence on radon detection. A correlation can be determined between the model of water behavior and the level of radon detection - the higher the correlation the higher the influence, the lower the correlation the lower the influence.

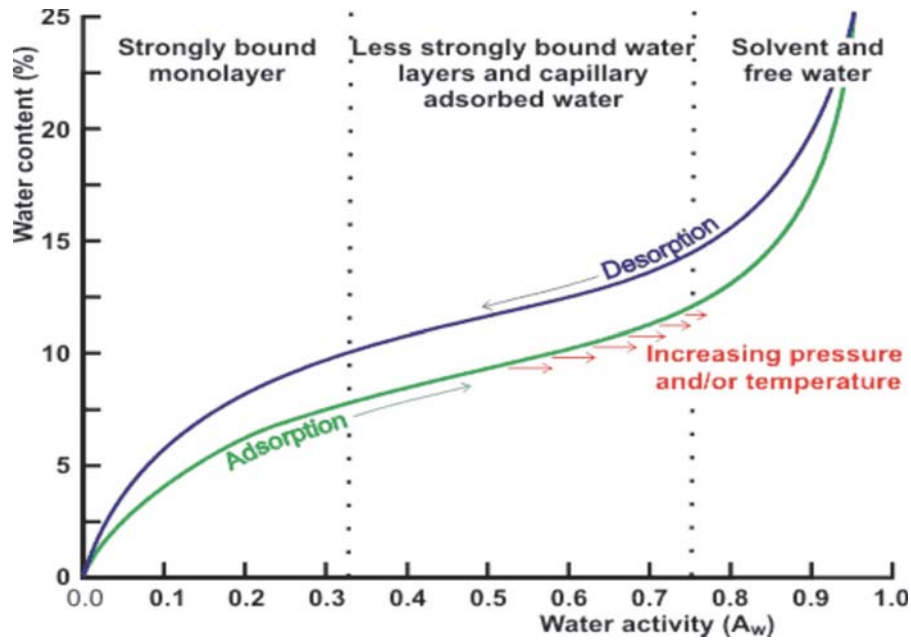


Figure 1.1: Adsorption and Desorption of water. (Chaplin M, 2008)

CHAPTER 2

Radon and its progeny coefficients

Radon is a naturally occurring radioactive noble gas. It has a variable distribution in the geological environment as a decay product of uranium, which is found in a wide range of rocks and soils and in building materials incorporating or manufactured from these sources. There are three naturally occurring isotopes of Radon: $^{222}\text{Rn}_{86}$, $^{220}\text{Rn}_{86}$, and $^{219}\text{Rn}_{86}$. Each radon is a decay product of a different radioactive source. $^{222}\text{Rn}_{86}$ with a half life of 3.823 days, is a direct product of $^{226}\text{Ra}_{88}$ in the $^{238}\text{U}_{92}$ decay-series. $^{220}\text{Rn}_{86}$ with a half life of 55.61 seconds, is the decay product of $^{232}\text{Th}_{90}$ decay series, and $^{219}\text{Rn}_{86}$ with a half life of 3.96 seconds, is the decay product of $^{235}\text{U}_{92}$ decay series. $^{222}\text{Rn}_{86}$ is most important because of its relatively longer half life. This enables it to migrate quite substantial distances within the geological environment and concentrate in the built environment such as in drinking water, in mines or in buildings, before decaying.

Ionizing radiation is well known to have adverse health effects. Inhalation/ ingestion of radon and its progeny $^{218}\text{Po}_{84}$ and $^{214}\text{Po}_{84}$ adsorbed onto atmospheric particles or in drinking water, is currently believed to be the cause of the majority of the cases of radiation doses to the respiratory system. This effect results in damage to the sensitive inner lining of the lungs, increasing the risk of cancer. Therefore the known biological effects are used in estimation of the annual mortality from exposure to radon and its progeny.

2.1 Radon diffusion coefficients

The process of radon migration in biological tissues is considered to be mainly diffusion or brownian motion in the form of passive transport along the concentration gradient. Diffusion is a thermodynamic effect which is the main deposition mechanism for small particle size. All particles with the same diameter below $0.1\mu\text{m}$ will have identical diffusion behavior, regardless of their density. The effect of diffusion is increased with the increasing size of the particle.

Radon likely travels in form of diffusion through the area as shown in simple form;

$$J = \frac{1}{A} \frac{\partial M}{\partial t} \quad (2.1)$$

where J = mass flux of substance or particle in $\text{kg}/\text{m}^2 \text{ s}$.

A = area in m^2

M = mass of substance or particle in kg

t = time in second

According to Fick's 1st law, the diffusion of particles is related to the concentration gradient;

$$J_x = -D \frac{\partial C}{\partial x} \quad (2.2)$$

where J_x = mass flux of substance or particle in x direction in $\text{kg}/\text{m}^2 \text{ s}$.

D = diffusivity coefficient, which is independent of composition, as a constant in m^2/s

C = concentration of substance or particle in kg/m^3

$\frac{\partial C}{\partial x}$ = concentration gradient of substance or particle in x direction (kg/m^4)

t = time in second

so $\frac{\partial C}{\partial x}$ must be constant in the steady state condition

(Glicksman and Lupulescu, 2007).

Therefore the increase in concentration, in cross section of unit area, with time is simply the difference between the flux into and the flux out of the relevant volume, as shown in Fick's 2nd law. The Fick's 2nd law is a fundamental conservation law for matter.

$$\frac{\partial C}{\partial t} = \frac{\partial J_x}{\partial x} = \frac{\partial}{\partial x} [D \frac{\partial C}{\partial x}] = D \frac{\partial^2 C}{\partial x^2} \quad (2.3)$$

By applying the some boundary conditions, (e.g. assumptions of $x=0$ at the surface at time $t=0$ instantly prior to initial diffusion, and also x increasing along into the volume of interest), the solution can be obtained as;

$$\frac{C_{(x,t)} - C_0}{C_s - C_0} = 1 - \operatorname{erf} \left[\frac{x}{\sqrt{4Dt}} \right] = \operatorname{erfc} \left[\frac{x}{\sqrt{4Dt}} \right] = \text{constant} \quad (2.4)$$

$$C_{(x,t)} = C_s - [C_s - C_0] \operatorname{erf} \left[\frac{x}{\sqrt{2Dt}} \right] \quad (2.5)$$

or
$$C_{(x,t)} = \frac{C}{2} \{ \operatorname{erfc} \left[\frac{x}{\sqrt{4Dt}} \right] \} = C_s \{ \operatorname{erfc} \left[\frac{x}{\sqrt{4Dt}} \right] \} \quad (2.6)$$

$$C_{(x,t)} = C_s \{ \operatorname{erfc} \left[\frac{x}{D_d} \right] \} = C_s \{ \operatorname{erfc} \left[\frac{\frac{x}{2}}{R_d} \right] \} \quad (2.7)$$

where C_s = the surface concentration as constant at $x=0$

C_0 = the concentration at $t=0$ and $0 \leq x \leq \infty$

$\operatorname{erf}(z)$ = gaussian error function $= \frac{2}{\pi} \int_0^z \exp(-n^2) dn$

$\operatorname{erfc}(z)$ = complementary error function $= 1 - \operatorname{erf}(z)$

$$t=0, C\{x, t=0\} = C_0 \text{ at } 0 \leq x \leq \infty$$

$$t>0, C\{x=0, t\} = C_s \text{ (the surface concentration as constant } C_s) \text{ at } x=0$$

$$\text{and } C = C_0 \text{ at } x = \infty$$

$$D_d = \text{diffusion displacement} = \sqrt{4Dt} \quad (2.8)$$

[Wikipedia encyclopedia (2007)]

$$R_d = \text{diffusion length} = \sqrt{\frac{D}{\lambda}} \quad (2.9)$$

$$D_d = 2 R_d = 2 \sqrt{\frac{D}{\lambda}} \quad (2.10)$$

$$\lambda = \text{the radon decay constant in (1/second)}$$

$$\text{and also } D = D_0 e^{-\frac{Q}{RT}} \quad (2.11)$$

where D_0 = initial diffusivity in m^2/s

Q = activation energy in J/mol or eV/mol

R = gas constant $8.31 \text{ J/mol} \cdot \text{K}$

T = temperature in $^\circ\text{K}$

Determination of the radon diffusion coefficient and the exhalation rate in solids were reported by Keller, Hoffmann, and Feigenspan (2001). Multi-channel analysis was used in alpha spectroscopy mode, to measure radon with the positive charged $^{218}\text{Po}_{84}$ -ions, electrostatically deposited on the detector surface. The sample of dry $^{226}\text{Ra}_{88}$, which was held between two chambers, produced $^{222}\text{Rn}_{86}$ until the level reached the steady state of 10^5 – 10^6 Bq/m^3 . The mean diffusion length (R_d) for building materials was determined from 0.7 mm for plastic foil to 1.1 m for gypsum. The diffusion length (R_d) = $\sqrt{\frac{D}{\lambda}}$,

where D is the diffusion coefficient. If the thickness of the material is more than 3 times

the diffusion length then it is called radon-tight. It was also concluded that when less than 3% of the available radon concentration can penetrate the material, the material is considered as radon-tight e.g. plastic coatings with a thickness of more than 2 mm with good sealing. Butyl rubber has a diffusion length of 2×10^{-3} m, but it is considered as radon permeable. This contrasts with the polymer concrete (PCC), which is radon-tight with the diffusion length (R_d) of 7×10^{-3} m.

In general the diffusion coefficient in porous media is a property of the diffusing species, the type of fluids filled within the pores, the pore structure, the fluid saturations, the adsorption properties of the solid matrix and the temperature.

2.2 Radon exhalation rate

The exhalation rate can be measured by placing a granular sample of the material into a glass bowl, which fits exactly into the opening of the detector (Yu et al., 1993a). The chamber of the detector was placed on one side of the sample, while the other side was placed on the plastic foil to avoid the radon penetration from the soil. The exhalation rate was determined and varied between 0.05 and 0.4 mBq/m²s. The diffusion coefficients (D) for the building materials were between 10^{-9} and 10^{-6} m²/s, which corresponds to diffusion lengths (R_d) of approximately 6 cm and 1 cm. The diffusion coefficient is independent of the material thickness but the calculated diffusion length was compared with the material thickness.

Radon migration can also be calculated in terms of the effective (or interstitial) radon diffusion coefficient (D_e) and the bulk radon diffusion coefficient (D_b). This calculation is based on the assumption that there is a diffusive density flux of radon activity (J_e) across

the pore area in unit of pCi/m²s and the concentration of radon activity in pCi/m³ (Yu et al., 1993a). The diffusions of radon in 1-D steady state condition are shown:

$$\frac{d^2}{dx^2} C - \frac{\lambda}{D_e} C = 0 \quad (2.12)$$

$$J_e = -D_e \left(\frac{d}{dx} C \right) \quad (2.13)$$

and $\left(\frac{d}{dx} \right) J_e = -\lambda C \quad (2.14)$

The bulk and the effective radon diffusion coefficients in soil, D_b and D_e , respectively, are correlated by the total soil porosity P_t as shown;

$$D_b = P_t D_e \quad (2.15)$$

$$D_b = \gamma(P_t)^\mu D_0 \text{ for only **dry** porous material} \quad (2.16)$$

$$D_e = \lambda d \left(\frac{C_0}{J_{e0}} \right) = \left(\frac{d}{R_d} \right) \left[\frac{(1 - e^{-\left(\frac{2d}{R_d}\right)})}{(1 + e^{-\left(\frac{2d}{R_d}\right)})} \right] \quad (2.17)$$

$$R_d = \sqrt{\frac{D_e}{\lambda}} \quad (2.18)$$

where

D_b = the bulk radon diffusion coefficients in soil

D_e = the effective radon diffusion coefficients in soil

P_t = the total soil porosity

D_0 = the radon diffusion coefficient in open air = $1.1 \times 10^{-5} \text{ m}^2/\text{s}$

C = the concentration of radon activity

λ = the radon decay constant in (1/second)

μ, γ = measures of pore shape of the soil materials

d = the thickness of the sample soil.

R_d = the radon diffusion length or relaxation length within porous medium

C_o = the concentration of radon activity in air within the chamber

J_{eo} = the effective flux density of radon at the bottom of the test soil column

$\frac{d}{R_d}$ = parameter ratio, which is independent of C_o and J_{eo}

Kotrappa et al. (1976) reported the dependence of the diffusion coefficient of radon/thoron decay products on the relative humidity of the atmosphere. The variations of relative humidity were 5% to 90% with a ventilation rate about 90 air change/hours and thoron about 10,000 pCi/liters, as shown in Table 2.1. The maximum value of diffusion coefficient occurs at 20-80%, with lower coefficients at both lower and higher relative humidities.

Relative humidity (%)	diffusion coefficient (cm ² /sec)
5-10	0.0535 ± 0.0014
10-20	0.0524 ± 0.0018
20-80	0.0604 ± 0.0023
80-90	0.0540 ± 0.0013

Table 2.1: The radon diffusion coefficients with different relative humidity (%).

2.3 Radon permeability coefficient

Radon gas is known to permeate through membranes of organic materials. The permeability coefficient of some plastic membranes can be determined by the equation shown below and the values in Table 2.2 (Jha, Raghavayya, and Padmanabhan, 1982).

membrane types	ratio R $(\frac{C_m}{C_0})$	membrane thickness (cm)	permeability coefficient (cm ² /sec)
Natural rubber	0.812	0.00508	6.36x10 ⁻⁶
Mylar	0.00162	0.00178	8.36x10 ⁻¹⁰
Polyvinyl chloride	0.00323	0.0533	5.00x10 ⁻⁸
Cellulose nitrate	0.219	0.00153	1.24x10 ⁻⁷
Polyester	0.0044	0.00152	1.95x10 ⁻⁹
Polycarbonate	0.00517	0.00254	3.82x10 ⁻⁹
All materials with effective membrane area of 1.13 cm ²			

Table 2.2: The radon permeability coefficient of different materials

$$R = \frac{C_m}{C_0} = \frac{1}{1 + \left[\frac{\lambda T V_1 V_2}{k A (V_1 + V_2)} \right]} \quad (2.19)$$

where R = the ratio of the count rate with the membrane (C_m) to the count rate without the membrane (C_0)

R_f = the discrimination factor radon as a barrier against the radon

($R_f > 0.9$ for ²²²Rn or $R_f < 0.01$ for ²²⁰Rn)

λ = the decay constant of the radon gas in (1/second)

T = the thickness of the membrane in cm

V_1 = the volume of the source container in cm³

V_2 = the volume of the detection chamber in cm³

A = the area of the membrane through which the radon gas permeates in cm²

k = the permeability coefficient of the membrane for the radon gas.

$$\text{If the } V_1 \gg V_2 \text{ or } 5(V_2) \leq V_1, \text{ then } R_f = \frac{C_m}{C_0} = \frac{1}{1 + \frac{\lambda T V_2}{kA}} \quad (2.20)$$

It is suggested that mylar is an effective barrier against radon, by using R_f as the discrimination factor in the determination.

2.4 Radon emanation coefficient

The emanation power or coefficient (ϵ) can be considered as the fraction of the radioactive inert gas atoms (such as radon) that escaped from the solid medium over the inert gas atoms formed within the solid medium. The emanation coefficient consists of the sum of the probabilities of the escape of the inert gas atom from the solid medium, as the result of the radioactive recoil process (ϵ_{recoil}), and the diffusion process ($\epsilon_{\text{diffusion}}$).

The emanation power depends on the mineral composition, crystal structure, specific surface area, temperature, moisture, and water content (Satomi and Kruger, 1982).

The emanation coefficient (ϵ_{recoil} or ϵ_r) due to the recoil effect of the radon atom, is the result of the radium decays by alpha particle emission. The radon atom must recoil in the opposite direction to conserve momentum. The recoil energy is sufficient to disperse the radon into the surroundings. The theory is based on assumptions of the model that the spherical grain of the radon (atom) is of sufficient age and the rate of inert gas formation (or radon) is equal to its decay rate within the radon atoms in the homogenous and isotropic grain of the parent radionuclide. The spherical grain of radius (r_0) is large when compared to the recoil range ($R_{\text{recoil}} = R$). The recoil range of radon is between 20- 70 nm in homogenous minerals. The assumption is valid since the grain sizes are typically of the order of $\geq 1 \mu\text{m}$.

The geometric loss $P(x)$ for the recoil atom is defined as the ratio of the surface area of the spherical plane beyond the boundary, to the surface area of the sphere with radius (R).

$$P(x) = \frac{2\pi R(R-x)}{4\pi R^2} = \frac{R-x}{2R} \quad (2.21)$$

where $x = (r_o^2 - R^2 - r^2)$ = the distance of radon movement

$$\text{and } P(x=r) = P(r) = \frac{2Rr - (r_o^2 - R^2) + r^2}{4Rr} \quad (2.22)$$

If the parent atom is located on the surface of a grain ($x=0$), the geometric loss $P(x)$ is 0.5. But if $x \geq R$, the radium atom is located within that region, it can not contribute to the emanation power of the grain. By assumption of the initial decay, the production rate of the daughter atoms per unit volume of radium can be $C_{\text{radium}} \lambda_{\text{radium}} \approx C_{\text{radon}} \lambda_{\text{radium}}$ due to the $\lambda_{\text{radium}} \ll \lambda_{\text{radon}}$ and the secular equilibrium ($\lambda_1 N_1 = \lambda_2 N_2 = \lambda_3 N_3 \dots$)

Therefore the production rate of escaped recoil radon atom ($N_{\text{radon escaped recoil}}$) can be

$$\text{derived as, } N_{\text{radon escaped recoil}} = C_{\text{radon}} \lambda_{\text{radium}} 4\pi \int_{r_o-R}^{r_o} P(r) r^2 dr \quad (2.23)$$

$$= C_{\text{radon}} \lambda_{\text{radium}} \pi (R r_o^2 - \frac{1}{12} R^2) \quad (2.24)$$

where C_{radon} = the radon concentration

λ_{radium} = the decay constant of radium

and the production rate of daughter atoms per unit volume is $C_{\text{radon}} \lambda_{\text{radium}}$

The total production rate of recoil radon atom ($N_{\text{total radon recoil}}$) is

$$N_{\text{total radon recoil}} = \left(\frac{4}{3}\right) \pi r_o^3 C_{\text{radon}} \lambda_{\text{radium}} \quad (2.25)$$

$$\epsilon_{\text{recoil}} = \frac{N_{\text{escaped radon recoil}}}{N_{\text{total radon recoil}}} \quad (2.26)$$

$$\epsilon_{\text{recoil}} = \left(\frac{3}{4}\right)\left(\frac{R}{r_o}\right) - \left(\frac{1}{16}\right)\left(\frac{R}{r_o}\right)^3 \quad \text{for } 2 r_o \geq R \quad (2.27)$$

$$\text{and} \quad \epsilon_{\text{recoil}} = \left(\frac{3}{4}\right)\left(\frac{R}{r_o}\right) \quad \text{for } r_o \geq R \quad (2.28)$$

$$\text{or} \quad \epsilon_{\text{recoil}} = \frac{1}{4} R \left[\frac{\text{grain surface area}}{\text{grain volume}} \right] \quad (2.29)$$

It is reported that a grain of 1 μm radius containing ^{226}Ra , with a radon recoil range of 36 nm, the emanation power due to recoil (ϵ_{recoil}) will be 2.7%.

Similarly for the emanation power due to diffusion, the flux of diffusing radon molecules (J_{radon}) can be defined as,

$$J_{\text{radon}} = -D \frac{\partial}{\partial x} C \quad (2.30)$$

$$\text{and also} \quad J_{\text{radon}} = \epsilon_d C_{\text{radon}} \lambda_{\text{radium}} \left[\frac{\text{particle volume}}{\text{particle surface area}} \right] \quad (2.31)$$

$$\text{therefore} \quad \epsilon_d C_{\text{radon}} \lambda_{\text{radium}} \left[\frac{\text{particle volume}}{\text{particle surface area}} \right] = -D \left[\frac{\partial}{\partial r} C \right]_{r=r_o} \quad (2.32)$$

where J_{radon} = the flux of the diffusing radon molecules ($\text{kg/m}^2 \text{ s}$)

C = the concentration of the diffusing radon molecules (kg/m^3)

D = the diffusion coefficient (m^2/s)

$\left[\frac{\partial}{\partial r} C \right]_{r=r_o}$ = the concentration gradient of radon at the particle surface

The mass balance equation based on the Fick's 2nd law can be derived as,

$$\frac{\partial}{\partial t} C_{\text{radon}} = [\text{diffusion rate of radon}] + [\text{production rate of radon}] + [\text{decay rate of radon}] + [\text{geometric loss } q(r) \text{ due to the particle size}(r)] \quad (2.33)$$

$$D \nabla^2 C_{\text{radon}} + C_{\text{radium}} \lambda_{\text{radium}} - C_{\text{radon}} \lambda_{\text{radon}} - C_{\text{radium}} \lambda_{\text{radium}} q(r) = \frac{\partial}{\partial t} C_{\text{radon}} \quad (2.34)$$

where
$$q(r) = \frac{Rr + r^2 - r_0^2 + R^2}{4Rr} \quad \text{for } r_0 - R \leq r < r_0 \quad (2.35)$$

$$= 0 \quad \text{for } 0 < r \leq r_0 - R \quad (2.36)$$

$$D\nabla^2 C_{\text{radon}} + C_{\text{radium}} \lambda_{\text{radium}} - C_{\text{radon}} \lambda_{\text{radon}} - C_{\text{radium}} \lambda_{\text{radium}} q(r) = 0 \text{ for steady state} \quad (2.37)$$

$$D\nabla^2 C_{\text{radon}} - C_{\text{radon}} \lambda_{\text{radon}} + C_{\text{radium}} \lambda_{\text{radium}} [1 - q(r)] = 0 \quad (2.38)$$

$$\frac{\partial^2}{\partial r^2} C_{\text{radon}} + \frac{2}{r} \frac{\partial}{\partial r} C_{\text{radon}} - \frac{\lambda}{D} C_{\text{radon}} = g(r) \quad \text{for the spherical rock} \quad (2.39)$$

where
$$g(r) = -\left(\frac{C_{\text{radium}} \lambda_{\text{radium}}}{D}\right)[q(r) - 1] \quad \text{for } r_0 - R \leq r < r_0 \quad (2.40)$$

$$= -\left(\frac{C_{\text{radium}} \lambda_{\text{radium}}}{D}\right) \quad \text{for } 0 < r \leq r_0 - R \quad (2.41)$$

For at the boundary conditions: $C_{\text{radon}}(0) < \infty$, and $C_{\text{radon}}(r_0) = C_{\text{surface}}$

$$\epsilon_d = \frac{3}{\Re} \frac{(2 - \xi)}{2} \quad \text{for large particle, } \xi \leq 1 \quad (2.42)$$

$$\epsilon_d = \frac{3}{\Re} \quad \text{for } \Re \gg 1 \text{ and } \xi \ll 1 \quad (2.43)$$

$$\epsilon_d = \left[\frac{\text{particle surface area}}{\text{particle volume}} \right] \sqrt{\frac{D}{\lambda_{\text{radon}}}} \quad (2.44)$$

$$\epsilon_d = \rho \left[\frac{\text{particle surface area}}{\text{particle mass}} \right] \sqrt{\frac{D}{\lambda_{\text{radon}}}} \quad (2.45)$$

The overall emanation power (ϵ) consists of the sum of the recoil and the diffusion process.

$$\epsilon = \epsilon_{\text{recoil}} + \epsilon_d = \left[\left(\frac{3}{4}\right) \frac{R}{r_0} \right] + 3 \left[\frac{\sqrt{\frac{D}{x}}}{r_0} \right] \quad (2.46)$$

where
$$\xi = \frac{R}{r_0}$$

$$\Re = r_o \sqrt{\frac{x}{D}} \quad (2.47)$$

ρ = the density of the particle

Radon emanation coefficient by diffusion ($\epsilon_{\text{diffusion}}$ or ϵ_d) is a dimensionless parameter, representing a fraction or percentage of the amount of radon produced from soil particles and the amount of radon entering into the pores of the medium. It is also called the escape-to-production ratio, or release ratio. The two common radioisotopes of radon gases, released within the soil, are ^{222}Rn (with kinetic recoil energy of 86 keV, from ^{226}Ra) and ^{220}Rn (with kinetic recoil energy of 103 keV, from ^{224}Ra). The radon emanation coefficient can be derived as shown in equation (2.46).

The diffusion coefficient of radon in air (D_o) can be derived in terms of flux density of diffusing substance, which is linearly proportional to its concentration gradient as shown in Fick's law (Yu et al., 1993b).

$$J = -D_o \nabla C \quad (2.48)$$

or $D_o = \frac{|J|}{|\nabla C|}$ for radon in open air (2.49)

similarly $D_e = \frac{|J_e|}{|\nabla C|}$ for radon within the pore area in soil (2.50)

The bulk radon diffusion coefficient (D) is defined as the ratio of the diffusive flux density of radon activity across area of the medium (J_b), to the gradient of radon activity concentration in the pore space (∇C);

$$D = \frac{|J_b|}{|\nabla C|} \quad \text{for radon in soil} \quad (2.51)$$

where

D = the (bulk) diffusion coefficient of radon in soil = D_b in equation (2.15)

D_o = the (bulk) diffusion coefficient of radon in open air e.g. $1.1 \times 10^{-5} \text{ m}^2/\text{s}$

D_e = the effective (or interstitial) diffusion coefficient of radon across of pore area

J_b = the diffusive flux density of radon activity across area of medium

J_e = the effective diffusive flux density of radon activity in the pore

J = the diffusive flux density of radon activity in the open air

∇C = the gradient of radon activity concentration

$$D = p_t D_e \quad (2.52)$$

and

$$D = [\gamma(p_t)^\mu] D_o \quad (2.53)$$

$$D_e = p_t D_o \exp(-6 p_t R_s - 6 R_s^{14 p_t}) \quad (2.54)$$

where p_t = the total soil porosity

μ, γ = dimensions of pore shape of the soil materials,

generally $\gamma = 0.8$ to 1.0 , $\mu \approx 1.0$; but they are not applicable for very wet soil

or strongly aggregate soil

R_s = saturation ratio which is the water saturation in soil or the fraction of the

pore space filled with water

$$\dot{S} = \epsilon_d \rho_s S_{Ra} \lambda \left[\frac{1 - p_t}{p_t} \right] \quad (2.55)$$

$$\text{or} \quad \dot{S} = \epsilon_d \rho_s C_{Ra} \lambda \quad (2.56)$$

where \dot{S} = the bulk radon production rate or emanation into the soil (pore air)

in $(\text{pCi}/\text{m}^3\text{s})$

ϵ_d = the radon emanation coefficient (due to diffusion) ≈ 0.25 for ^{222}Rn

ρ_s = the soil particle density or the bulk dry density of medium (kg/m^3)

λ = the radon decay constant in (1/second)

S_{Ra} = the mass concentration of radium in the soil particle in (pCi/kg)

C_{Ra} = the radium activity per unit dry mass (Bq/kg)

p_t = the total soil porosity of the soil.

Radon transport in soil and building materials is considered in terms of diffusion and advection through the porous medium, which usually has irregularly shaped and positioned pores. In most cases the pore space is filled with air and/or water, leading to a multiphase system, e.g., gas in air, gas in water or gas in solid. The porosity and the fraction of water saturation are parameters to quantify the structure and phase composition of the porous medium. The porosity (p_m) is defined as the volume fraction of the medium occupied by the pores, and the fraction of water saturation (m_{water}) is the volume fraction of the pores occupied by water. The radon activity bulk fluxes ($Bq/m^2 s$) by diffusion and advection ($J_{d,a}$), by diffusion in water phase ($J_{d,water}$), and by advection in air ($J_{a,air}$) are considered in the mass balance equation (Nuclear Geophysics Division, 2007).

The total emanation coefficient can be derived from the sum of fractional emanation coefficients in the air, water, and adsorbed phase in solid surfaces (ϵ).

$$\epsilon_d = \epsilon_{air} + \epsilon_{water} + \epsilon_{solid} = \epsilon_a + \epsilon_w + \epsilon_s \quad (2.57)$$

The mass balance equations for each phase (air, water, and solid surfaces, respectively) can be derived,

$$(1-m) p_t \frac{\partial C_a}{\partial t} = \nabla \{ (1-m) p_t \tau_a D_a \nabla C_a \} + \left(\frac{k}{\mu} \right) \nabla P \cdot \nabla C_a - (1-m) p_t \lambda C_a + \epsilon_a \rho_b \lambda C_{Ra} - \sum (T_{ai} - T_{ia})$$

in air phase (2.58)

$$m p_t \frac{\partial C_w}{\partial t} = \nabla \cdot (m p_t \tau_w D_w \nabla C_w) - m p_t \lambda C_w + \epsilon_w \rho_b \lambda C_{Ra} - \sum (T_{wi} - T_{iw}) \quad \text{in water phase} \quad (2.59)$$

$$\rho_b \frac{\partial C_s}{\partial t} = - \rho_b \lambda C_s + \epsilon_s \rho_b \lambda C_{Ra} - \sum (T_{si} - T_{is}) \quad \text{in solid surface (advection) phase} \quad (2.60)$$

where m = the fraction of water saturation which is the volume fraction of the pores occupied by water

p_t = the porosity which is the volume fraction of medium occupied by pores

τ_a = the tortousity which is empirical factor accounting for the elongated path of transport due to twisting and turning of the pores

C_{Ra} = the radium activity per unit dry mass (Bq/kg)

λ = the radon decay constant in (1/second)

C_a, C_w = the radon concentration in the air and water phase (Bq/m³)

C_s = the radon concentration adsorbed per mass unit of dry material (Bq/m³)

μ = the dynamic viscosity of air (Pa sec.)

ϵ_a, ϵ_w = the emanation coefficient in the air and water phase

ρ_b = the bulk dry density of the porous medium (kg/m³) = $(1 - p_t) \rho_s$

$(1 - p_t)$ = the ratio of the solid volume (V_s) to the total volume ($V_t + V_g + V_s$)

k = the intrinsic permeability (m²)

D_a, D_w = the diffusion coefficient in air and water phase (m²/sec)

P = the pressure disturbance field (relative to absolute pressure) (Pa)

The transfer coefficients which are the Ostwald coefficient (L) and the radon surface adsorption coefficient (k_a) can be derived when $T_{ws}=T_{sw}=0$, $T_{as}=T_{sa}(=0$ in case adsorption is negligible), and $T_{aw}=T_{wa}$ are the assumptions and used.

$$\frac{C_w}{C_a} = L = \frac{\alpha_{aw}(1-m)}{\alpha_{wa}m} \quad (2.61)$$

$$\frac{C_s}{C_a} = k_a = \frac{\alpha_{as}(1-m) p_t}{\alpha_{sa}\rho_b} \quad (2.62)$$

α_{aw} = the exchange rate between air and water phase

m = the fraction of water saturation which is the volume fraction of the pores occupied by water

k_a = the radon surface adsorption coefficient

L = the Ostwald coefficient or the Radon solubility

The combination of all 3 phases can be combined in one equation for the radon in air phase as shown below, with the assumption that the air density is constant for the pressure field ($\nabla^2 P=0$),

$$\beta \frac{\partial C_a}{\partial t} = \nabla (D \nabla C_a) + \left(\frac{k}{\mu}\right) \nabla P \nabla C_a - \beta \lambda C_a + \dot{S} \quad (2.63)$$

where

β = the partition-corrected porosity = $(1-m+mL)p_t + \rho_b k_a$

D = the bulk diffusion coefficient in (Bq/m³s) = $[(1-m) \tau_a D_a + m \tau_w D_w L] p_t$

\dot{S} = the bulk radon production rate per unit bulk volume or the emanation into the soil (pore air) in (pCi/m³s) = $\epsilon_d \rho_s C_{Ra} \lambda$

CHAPTER 3

Properties of Radon affected by Temperature and Humidity

3.1 Basic equations of temperature, humidity and dew point temperature

Air is a mixture of different gas components which are approximately in volume: N₂ 78.03%, O₂ 20.99%, Ar 0.93%, CO₂ 0.03%, others (H₂, Ne, He, Kr) 0.02%, or in weight N₂ 75.47%, O₂ 23.20%, Ar 1.28%, CO₂ 0.04%, others (H₂, Ne, He, Kr) 0.01%. When water is in its gaseous phase or vapor, it is an addition to the ideal gas component of the air.

The total pressure of air (P) is the sum of partial pressure of dry air (P_{dry air}) and the partial pressure of water vapor (P_{water}) in mbar or hPa.

$$P = P_{\text{dry air}} + P_{\text{water}} \quad (3.1)$$

The balance between the condensation and the evaporation of water leads to a vapor pressure which depends on the temperature. At high temperatures air can hold more vapor than at low temperature.

The saturation vapor pressure above water (P_{water}) can be calculated by the Magnus formula (Sonntag 1990);

$$P_{\text{water}} = x e^{\frac{yT}{(z+T)}} \quad (3.2)$$

Where x is constant =6.112

y is constant =17.62

z is constant = 243.12

T is temperature in °C between -45 to 50 °C

Humidity can be described as the amount of water vapor or moisture being carried by air.

It is defined as the ratio between the actual partial vapor pressure (P_{actual}) and the saturation vapor pressure above water (P_{water}), or the ratio between partial pressure by the dew point temperature ($P_{\text{dew point}}$) and partial pressure by the ambient temperature (P_{ambient}). Since the actual partial vapor pressure can not exceed the saturation vapor pressure at equilibrium, the maximum relative humidity is 100%.

$$\text{Relative Humidity (RH)} = \left[\frac{P_{\text{actual}}}{P_{\text{water}}} \right] \times 100 \% \quad (3.3)$$

or

$$= \left[\frac{P_{\text{dew point}}}{P_{\text{ambient}}} \right] \times 100 \% \quad (3.4)$$

At the dew point temperature ($T_{\text{dew point}}$), the actual vapor pressure is equal to the saturation vapor pressure, and the relative humidity approaches its maximum value of 100%.

Humidity can be measured either as absolute humidity or relative humidity: the absolute humidity is the weight of water vapor per unit volume of air, which depends on its pressure and temperature, or gram per cubic meter; the relative humidity is the saturation condition in percentage.

The dew point temperature is the temperature at which air becomes saturated with vapor, which starts to condense. Any lowering of temperature below the dew point temperature results in condensation of some of the water vapor present.

$$\text{Relative Humidity (RH)} = (10^m / 10^n) \times 100 \% = \left[\frac{P_{\text{dew point}}}{P_{\text{ambient}}} \right] \times 100 \% \quad (3.5)$$

Partial pressure by dew point temperature ($P_{\text{dew point}}$) in mmHg = 10^m

and Partial pressure by ambient temperature (P_{ambient}) in mmHg = 10^n

where m is $\log(P_{\text{dew point}}) = A - \left[\frac{B}{T_{\text{dew point}} + C} \right]$ (3.7)

n is $\log(P_{\text{ambient}}) = A - \left[\frac{B}{T_{\text{ambient}} + C} \right]$ (3.8)

A is constant = 8.1332

B is constant = 1762.39

C is constant = 235.66

$T_{\text{dew point}}$ is dew point temperature in °C

T_{ambient} is ambient temperature in °C

Concentration by dew point temperature in ppmv = $\left(\frac{10^m}{760 \times 10^6} \right)$ (3.9)

Concentration by dew point temperature in g/m³ = $\left(\frac{10^m}{760 \times 10^6} \right) \left(\frac{0.001 \times 18}{22.4} \right)$ (3.10)

Concentration by dew point temperature in g/kg = $\left(\frac{10^m}{760 \times 10^6} \right) \left(\frac{0.001 \times 18}{22.4} \right) \left(\frac{1}{1.2} \right)$ (3.11)

Ambient temperature = $\left\{ \frac{-B}{\log\left[\left(\frac{10^m}{RH}\right) \cdot 100\right] - A} \right\} - C$ (3.12)

Dew point temperature = $\left[\frac{-B}{\log\left[\left(\frac{10^n \cdot RH}{100}\right) - A \right]} \right] - C$ (3.13)

3.2 Radon solubility in water

In a closed system the radon solubility in water is obtained by directly bubbling or slowly diffusing radon gas into the water. The relation between the air radon concentration and the radon in water concentration is at a steady state and it can be

described by radon's water solubility in terms of the Ostwald coefficient (k) in the steady state (Surbeck, 1996).

$$\frac{C_{air}}{C_{water}} = \frac{1}{\left[\frac{V_{air}}{V_{water}}\right] + k} \quad (3.14)$$

but $\left[\frac{V_{air}}{V_{water}}\right] + k = \frac{C_{water}}{C_{air}}$ is the steady state ratio (3.15)

where C_{air} = radon concentration in air

C_{water} = radon concentration in water

k = radon's water solubility or Ostwald coefficient

V_{air} = air volume

V_{water} = water volume

The radon solubility is temperature dependent between 10°C -20°C and the radon solubility decreases by about 3% per °C (Figure 3.1, page 34). The relation between the radon's water solubility (k) and the temperature T (°C) (Lawrence, 1979) can be interpolated as shown below with $r^2 = 0.99955423$ by the equilibrium concentration curve fitting (Figure 3.2, page 35);

$$k = (a-b) e^{-cT} + b \quad (3.16)$$

where a = 0.52842332

b = 0.108844754

c = 0.051255005

The solubility of radon (^{222}Rn) in the water can be determined in the equilibrated gaseous phase and liquid phase (Battino, 2006). The radon partial pressure is about 10^{-4}

mmHg (0.01 Pa). The Ostwald coefficient or radon solubility (k) in water (Figure 3.3, page 37) can be derived as;

$$k = \frac{G_L}{G_g} \quad (3.17)$$

and also
$$k = \frac{V_g}{V_s} \quad (3.18)$$

G_L = concentration of gas per unit volume of liquid phase

G_g = concentration of gas per unit volume of gas phase

V_g = volume of gas (^{222}Rn) at its partial pressure and temperature T

V_s = volume of solvent (water) used to absorb the gas (^{222}Rn) at temperature T

If there is negligible volume change on mixing, then

$$\frac{G_L}{G_g} = \frac{V_g}{V_s} \quad (3.19)$$

and
$$X_L = \frac{1}{\left[\frac{RT}{V_L \cdot P_L \cdot k}\right] + 1} \quad (3.20)$$

X_L = the mole fraction solubility at the partial pressure of gas 101.325 Pa

R = the gas constant

V_L = the molar volume of the solvent (water) at temperature T in $^{\circ}\text{K}$

P_L = the partial pressure of the solvent (water) at temperature T in $^{\circ}\text{K}$

T = temperature in $^{\circ}\text{K}$

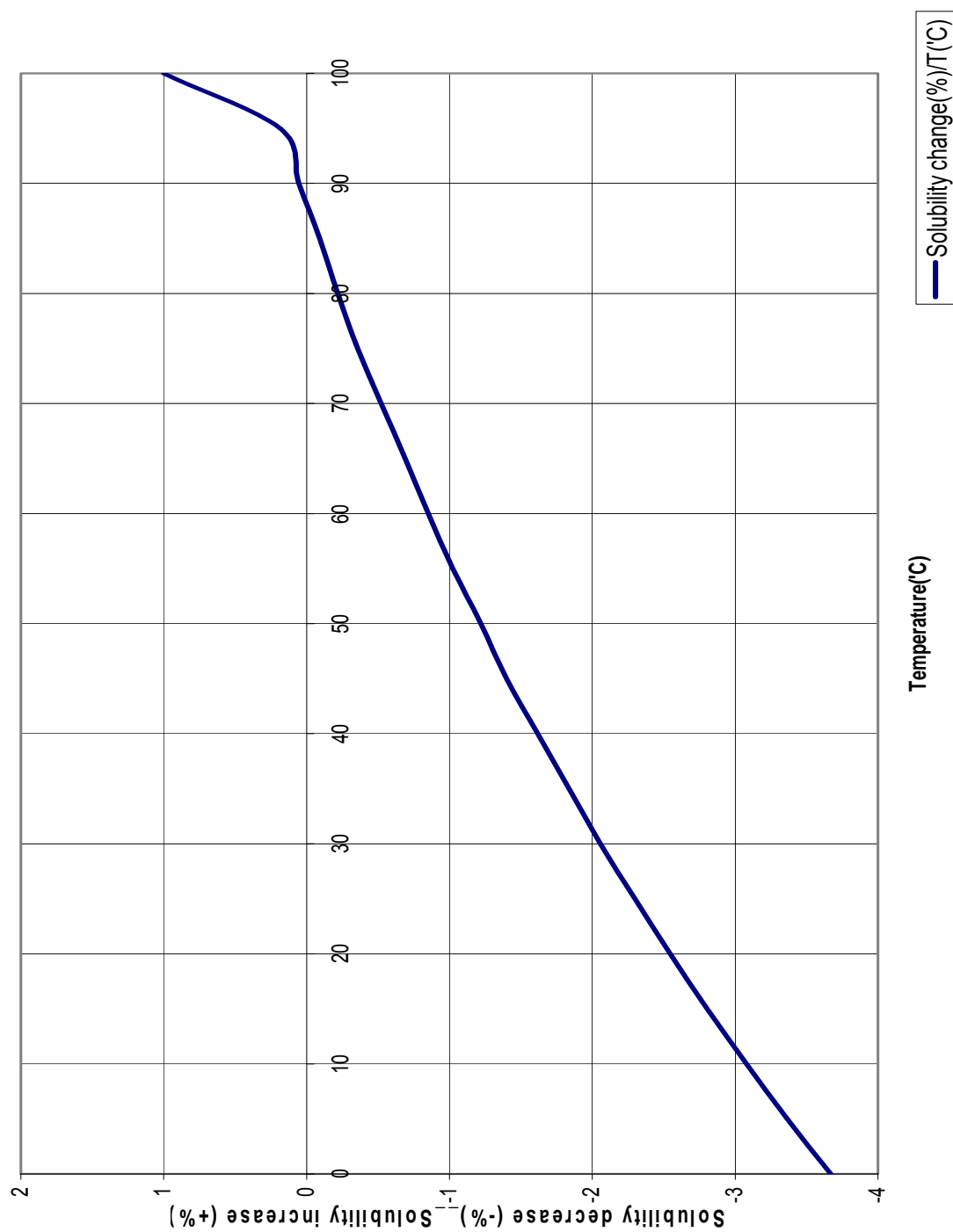


Figure 3.1: Radon solubility change per temperature change (Surbeck, 1996)

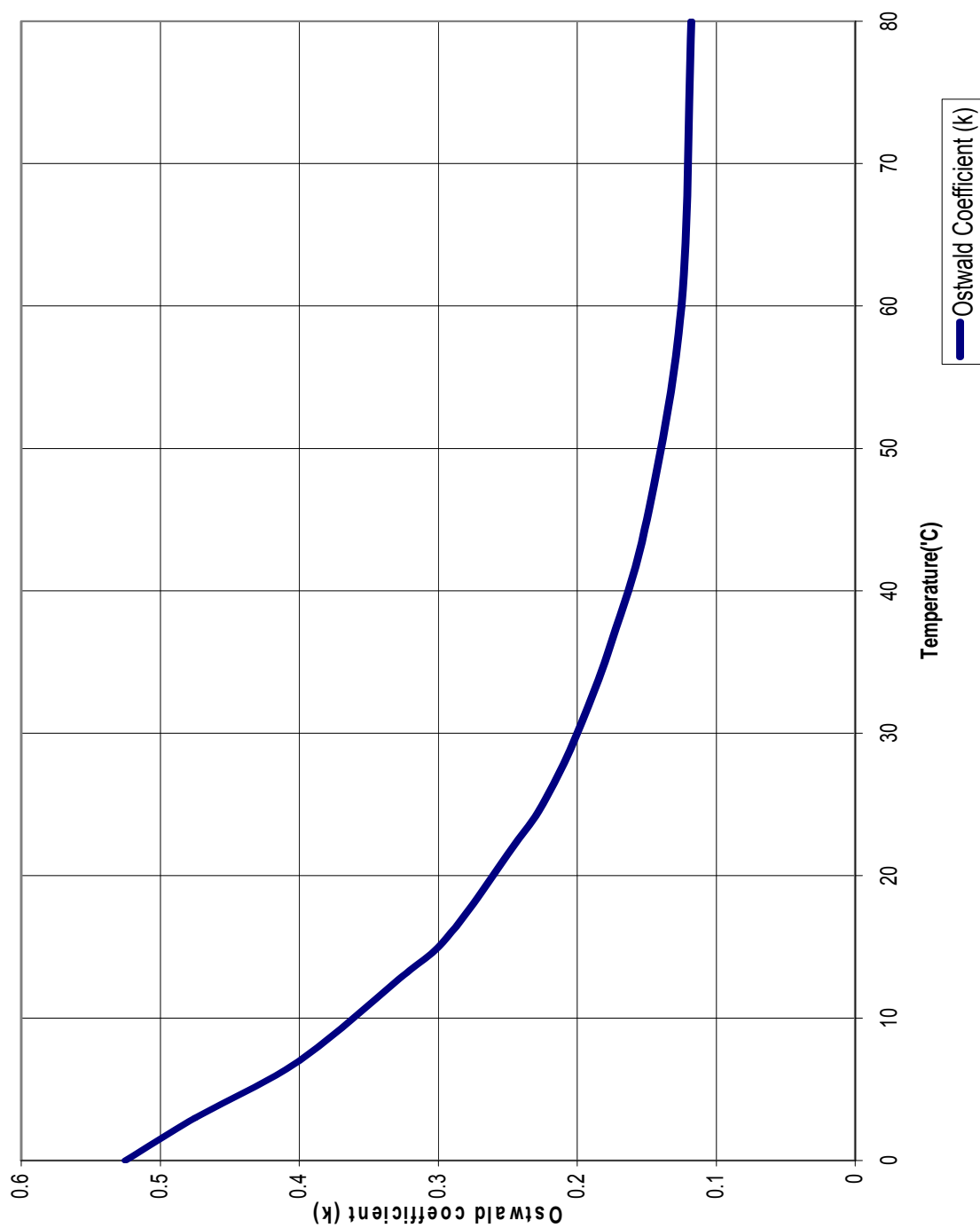


Figure 3.2: Ostwald coefficient (k) vs Temperature (Surbeck, 1996)

The Ostwald coefficient or radon solubility (k) in water at 14 °C varies from 0.299 to 0.307, which is considered to be within experimental error.

The fitting equation is obtained as:

$$\ln (X_L) = -90.5481 + \frac{130.26}{(\frac{T}{100})} + 35.0047 [\ln (\frac{T}{100})] \quad (3.21)$$

The value of the Ostwald coefficient also agreed with the calculation, performed by solubility of the hydrophobe in the one-dimensional solution model, for a hydrophobic solute (with hydrophobic effect such as water as the solvent) (Kolomeisky and Widom, 1999). The solubility decreases with increasing temperature as expected for a hydrophobic solute. The solubility of radon, which is more than twice that of Xe, in water compared to the other inert gases is shown in Appendix E (page 106).

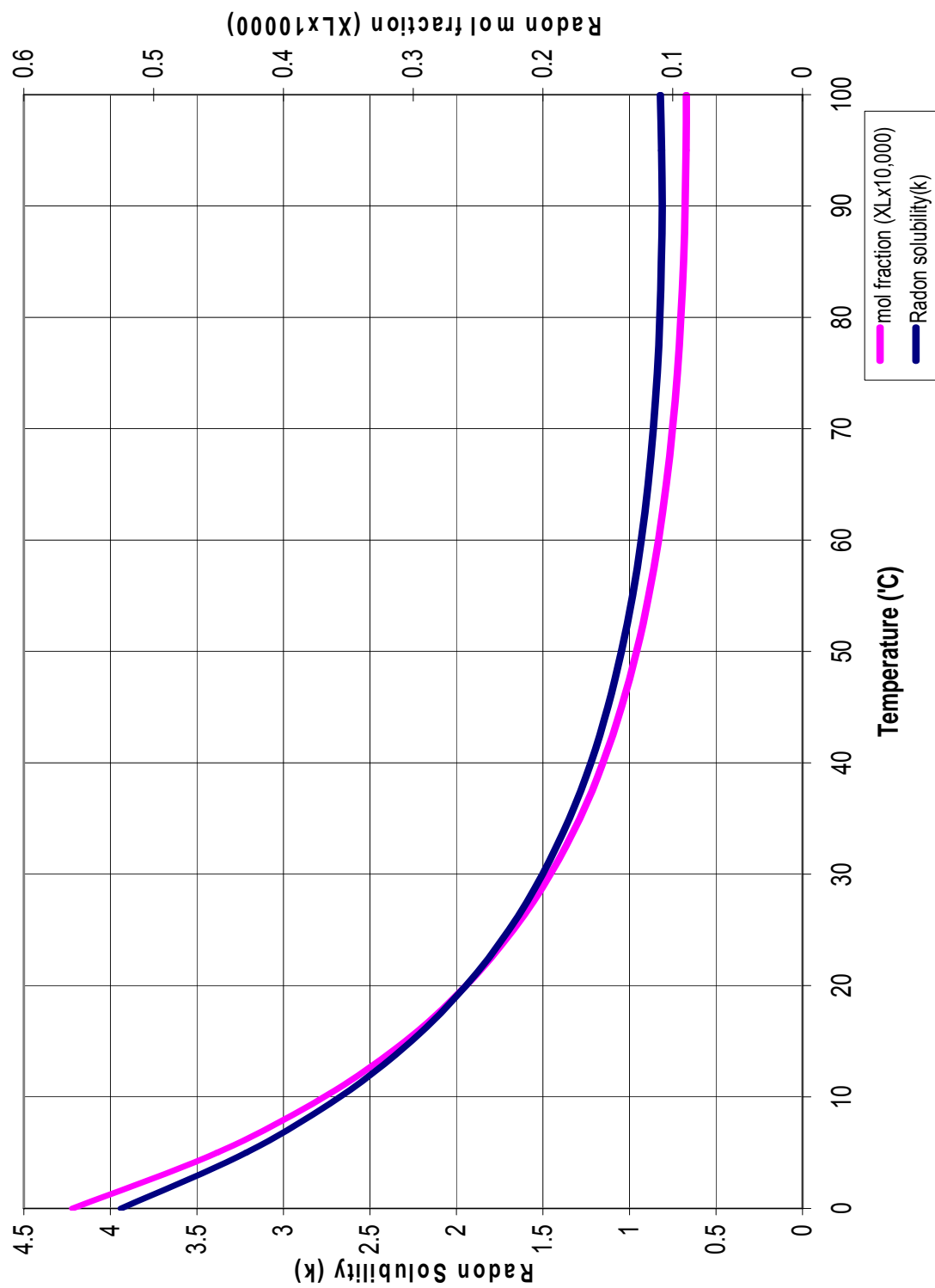


Figure 3.3: Radon solubility in water, radon partial pressure 10^{-4} mmHg (0.01 Pa)
(Battino, 2006)

CHAPTER 4

Biological effects of Radon and Radon Progeny

4.1 Mechanisms of airborne particles

Airborne radionuclide such as ^{222}Rn can be in gas or vapor form associated with liquid or solid particles known as aerosols. There are three main mechanisms that affect the behavior of airborne particles in the respiratory tract (Valentin, 2002): gravitational sedimentation, inertial impaction, and diffusion or Brownian motion.

Gravitational sedimentation and inertial impaction are aerodynamic effects which are important to large particle sizes above $0.1\mu\text{m}$. The effects of sedimentation and impaction are increased with particle density, and particles with different densities will behave differently for diameters greater than $1.0\mu\text{m}$.

$$D_{ac} \approx (\rho)^{1/2} D_p \quad (4.1)$$

where D_{ac} is the aerodynamic equivalent diameter, or diameter of a unit density sphere with the same terminal settling velocity in air as the particle of interest.

D_p is physical or geometric diameter of the particle.

ρ is density of the particle.

All small particle size with the equal diameter ($< 0.1\mu\text{m}$) will have identical diffusion behavior, regardless of their density. The effect of diffusion is directly proportional to the size of the particle.

$$D_{th} \approx D_p \quad (4.2)$$

where D_{th} is thermodynamic equivalent diameter, or diameter of the spherical particle with the same diffusion coefficient in air as the particle of interest.

D_p is physical or geometric diameter of particle.

Aerosols are usually composed of particles with different sizes which are monodisperse, but they can also be polydisperse and composed of a mixture of different particle sizes. The fractions of the aerosol, in a set of contiguous size intervals, form the size distribution. It is generally assumed that radioactive particles have a log-normally sized distribution. It is suggested that the mean diameter of the particle is the value of the particle size at the 50th percentile of distribution. The geometric standard deviation (SD_g) is the ratio between two values of the particle sizes at different percentile of distribution, as shown;

$$(SD_g) = \frac{\text{particle size at the 50}^{\text{th}} \text{ percentile}}{\text{particle size at the 16}^{\text{th}} \text{ percentile}} = \frac{\text{particle size at the 84}^{\text{th}} \text{ percentile}}{\text{particle size at the 50}^{\text{th}} \text{ percentile}}$$

Depending on the particle size range and the measurement techniques performed, aerosols can be measured by either the activity median aerodynamic diameter (AMAD), or the activity median thermodynamic diameter (AMTD). AMAD, which depends mainly on sedimentation and inertial impaction, is greater than about 0.5 μ m. AMTD which is less than about 0.5 μ m (by the diffusion mechanism) is about 50% of the activity in the aerosol.

The International Committee on Radiological Protection (ICRP) recommended the dose conversion factor of 5 mSv per WLM for workers in the radon environment (ICRP 1994), and a breathing rate of 1.2 m³/hr to be used for the AMAD of 0.2 -0.3 μ m (or 200 - 300nm) in the ICRP model of radon progeny size distribution. The dose conversion factor is dependent on the unattached fraction of the radon progeny. The radon progeny attaches, with the ambient aerosol particles, immediately after it is decayed from the radon. There are two fractions; an attached fraction, which is an important factor of dose estimation, and an unattached fraction of radon progeny in the air. The ratio of

unattached fraction to total radon progeny is an important factor for the dose estimation, even the unattached fraction is not much affected by the surrounding condition.

The ICRP human respiratory tract model (ICRP, 1995) was determined by the stochastic transport and deposition code IDEAL6 (Hofmann and Bergmann, 2000). The airways system was scaled down to a functional residual capacity of 3300ml and the alveolar deposition can be observed at around 400nm (or 0.4 μ m). It was assumed that ICRP compartments were statistically independent from each other. Therefore standard deviations of the deposition fractions for the ICRP model could be obtained by multiplying the average ICRP deposition fraction with the stochastically derived coefficients of variation. The unattached fraction of the radon decay products can be generated, as small as 1nm (or 0.001 μ m) and up to as large as 500nm (or 0.5 μ m), by the vaporization-condensation method. The aerosol sizes can be monitored by a screen type diffusion battery method or by a scanning type mobility particle sizer method (Yamada et al., 2004).

The very small particles of 1nm (or 0.001 μ m), which likely is AMAD represents the unattached (or ultrafine) and attached fraction of aerosol, or 0.6nm (or 0.0006 μ m), which is AMTD represents the unattached fraction of aerosol, are suggested by Kendall and Smith (2002). Almost 90% are very mobile and are deposited by diffusion within the airways before reaching the lung. The larger particle of 200nm (or 0.2 μ m) (AMAD) are less mobile and penetrate deeper into the lung but most are exhaled out with 70% in the deep alveolar region and 30% in the airways. The assumption is made that all the activities of mixture ^{222}Rn : ^{218}Po : ^{214}Pb : ^{214}Bi are in the ratio of 1.0:0.9:0.45:0.225, when

the mixture of nucleides usually depends on the aerosol concentration and the ventilation rate.

The annual effective dose equivalent to the population (NCRP, 1987) of natural radon is about 200 mrem or 55% of the total dose (360 mrem). Radon and radon progeny alpha particles expose the cells along their passages in the form of ionizing radiation directly and they also damage DNA indirectly. The energy deposited by the irradiation in the mucous layer results in exposure of the epithelial cells from the unilateral sources on the surfaces. The dense ionization of ion-pair clusters (free radical formation) can be found along the tracks of the alpha particles across a cell of tissues in less than 10^{-12} seconds and they also deposit energy of about 10-50 cGy (Jostes, 1996). The particles slow down and deposit high linear energy transfer (LET) per unit length of track, until it reaches the maximum amount at the end of their track, which is called Bragg peak. The number of double-strand breaks occur, as multiple locally damaged sites and also as a non-uniform distribution of DNA breaks (Double-strand DNA breaks), with an excess of small fragments that can rejoin. The dose of about 1.2-1.5 alpha particles per spherical nucleus is required to produce an average of one lethal hit to a cell (the D_{37}). The lethality can be described as the net absorption of the total energy per cell along the total path length through the nucleus. It can be either a single track through a spherical nucleus or several shorter tracks through a flat nucleus. The ion pairs that do not directly damage the DNA, can produce reactive oxygen intermediates which influence the stability of protein p53, with further effects on cell regulation. Reactive oxygen intermediates can produce oxidative damage to the DNA and/or in both deoxyribose and ribose triphosphates.

Oxidized nucleotides in DNA and RNA can show either DNA mutation or transcription and translation errors.

4.2 Radon in the respiratory system

Radon is considered to be most harmful in the respiratory system, because radon is an airborne particle which can ionize the tissue and water in the lung. Radon has been found to induce 13 times as much cytogenetic damage, as measured by the occurrence of micronuclei, than a similar dose of ^{60}Co . It was suggested that approximately half of the alpha-induced mutations arise by the complete deletion of the gene; the remaining mutations were shown as partial deletions, rearrangement, and events undetectable. DNA deletions or multi-locus lesions of various sizes appeared to be predominant after radon exposure, and also to be a risk factor for lung cancer.

Assumptions can be made as;

- 1) the cells irradiated by the particles have a greater possibility of cancer induction than the average carcinogenic potential of all lung cells.
- 2) the rate of cancer induction increases with the dose more than linearly. The cellular effects produced by the alpha particles are proportional to the absorbed dose at low and intermediate absorbed doses and then decline at higher absorbed dose due to a saturation effect. The cellular effects of alpha particles are different from the results of the low-LET beta or gamma irradiation, which cause cytotoxic effects to be linearly increased greater with absorbed dose.

The average of the probability over the sphere for each traversal at distance is directly proportional to $(\frac{3}{R^3})$, where R is the range of the alpha particle.

The alpha particle range in air (at 15°C and 1atm) (Cember, 1996), is closely approximated by:

$$R_{\text{air}} (\text{in cm}) = 0.56 E_{\alpha} \quad \text{for } E_{\alpha} < 4\text{MeV} \quad (4.3)$$

$$\text{and} \quad R_{\text{air}} (\text{in cm}) = 1.24 E_{\alpha} - 2.62 \quad \text{for } 4 \leq E_{\alpha} < 8\text{MeV} \quad (4.4)$$

If the energy of alpha is 5.489 MeV, the alpha particle range in air can be calculated,

$$R_{\text{air}} (\text{in cm}) = 1.24 (5.489) - 2.62 = 4.186 \text{ cm} \quad (4.5)$$

The alpha particle range in tissue can be obtained from the Bragg-Kleeman equation

$$\text{shown; } \frac{\text{Range in medium1}}{\text{Range in medium2}} = \left(\frac{\rho_2}{\rho_1} \right) \left(\frac{\text{atom.mass medium1}}{\text{atom.mass medium2}} \right)$$

$$\text{Therefore } R_{\text{in tissue}} = R_{\text{in air}} \left(\frac{\rho_{\text{air}}}{\rho_{\text{tissue}}} \right) \approx 1.293 \times 10^{-3} R_{\text{air}} \quad (4.6)$$

where the density of air at STP is $1.293 \times 10^{-3} \text{ g/cm}^3$ and the density of tissue is assumed to be the density of water which is 1 g/cm^3 . The lung density is 0.3 g/cm^3 .

The alpha particle range in tissue ($R_{\text{in tissue}}$) is approximately $(1.293 \times 10^{-3})(4.186)$

$$R_{\text{in tissue}} \approx 0.00541 \text{ cm} \approx 54.1 \mu\text{m} \quad (4.7)$$

and the alpha particle range in lung ($R_{\text{in lung}}$) is,

$$R_{\text{in lung}} \approx (1.293 \times 10^{-3})(4.186)/0.3 \approx 180.3 \mu\text{m} \approx 0.01803 \text{ cm} \quad (4.8)$$

Alternatively, the alpha particle range in air can be calculated by using a semi-empirical formula (Tsoulfanidis, 1983), as shown below:

$$R_{\text{air}} (\text{in mm}) = e^{1.6\sqrt{E_{\alpha}}} \quad \text{for } 4\text{MeV} < E_{\alpha}, \text{ or } E_{\alpha} \leq 4\text{MeV} \quad (4.9)$$

$$\text{and} \quad R_{\text{air}} (\text{in mm}) = (0.05 E_{\alpha} + 2.85)[(E_{\alpha})^{3/2}] \quad \text{for } 4 \leq E_{\alpha} < 15 \text{ MeV} \quad (4.10)$$

Therefore the alpha particle range in air is $[(0.05)(5.489) + 2.85][(5.489)^{3/2}]$

$$\approx 3.1244(12.8635) \approx 40.19 \text{ mm} \approx 4.019 \text{ cm}.$$

The alpha particle range in tissue ($R_{\text{in tissue}}$) is approximately $(1.293 \times 10^{-3})(4.019)$

$$R_{\text{in tissue}} \approx 0.005196 \text{ cm} \approx 51.96 \text{ } \mu\text{m} \quad (4.11)$$

The alpha particle in lung can also obtained as $\approx 0.01732 \text{ cm} \approx 173.2 \text{ } \mu\text{m}$.

It can be concluded that the alpha particle range in the lung is 173-180 μm traveling within the lung as a spherical domain of radius 200 μm .

Let N be the number of cells traversed during t days,

A is the activity in Ci

t is time in days using $t=3.823$ days

v is the number of disintegrations produced by activity A for each alpha particle traversed one cell in t days

ξ is the expected number of traversals

If alpha particles arising from a fixed point (particulate radon at a fixed location)

$$v = 3.7 \times 10^{10} (3600 \times 24) t A = 3.2 \times 10^{15} t A \quad \text{per alpha particle per one cell}$$

$$\text{or} \quad 5v = 5 \times 3.2 \times 10^{15} t A \quad \text{per particle per path or traversals}$$

$$5v = 1.6 \times 10^{16} t A \quad \text{per particle per path or traversals}$$

$$N = 1.6 \times 10^{16} t A \quad (4.12)$$

If the spherical domain of radius 200 μm , in which the fluence of alpha particles is inversely proportional to the square of distance r from the center,

$$\xi = \frac{k}{r^2} \quad (4.13)$$

The cells at the border of the domain may be partly traversed by the alpha particles and the reduction of energy deposition can only create non-lethal damages, which possibly develop abnormality of the cell in terms of a tumor. The population of 6600 cells is

considered to occupy the spherical domain of radius 200 μm . Therefore the fraction of “cells at risks”, which are actually traversed by alpha particles, increases as the activity of the alpha particles increases.

If the cell is at the distance (r) from the alpha particle, the mean number of traversals per cell in the sphere can be obtained by integrating the numbers of traversals, over the sphere of radius R from 0 to R , where R is the alpha particle range.

$$\text{averaged } \xi = \frac{\int_0^R \left(\frac{k \cdot r^2}{r^2} \right) dr}{\int_0^R r^2 dr} = \frac{3k}{R^2} \quad (4.14)$$

From the poisson equation:

the probability for zero traversals at distance r is $p_0 = e^{\frac{-k}{r^2}}$

the probability for one traversals at distance r is $p_1 = \left(\frac{k}{r^2} \right) e^{\frac{-k}{r^2}}$

Similarly the average of the probability over the sphere is averaged p_0 for zero traversals at distance r ,

$$\text{averaged } p_0 = \frac{\int_0^R r^2 e^{\frac{-k}{r^2}} dr}{\int_0^R r^2 dr} = \left(\frac{3}{R^3} \right) \int_0^R R^2 e^{\frac{-k}{r^2}} dr \quad (4.15)$$

the average of the probability over the sphere is averaged p_0 for one traversals at distance r

$$\text{averaged } p_1 = \frac{\int_0^R \left(\frac{r^2 k}{r^2} \right) e^{\frac{-k}{r^2}} dr}{\int_0^R r^2 dr} = \left(\frac{3k}{R^3} \right) \int_0^R e^{\frac{-k}{r^2}} dr \quad (4.16)$$

Therefore the probability for multiple traversals averaged over the sphere is ;

$$\text{averaged } p_{\xi > 1} = 1 - (\text{averaged } p_0) - (\text{averaged } p_1) \quad (4.17)$$

The equation (4.17) suggests that the absolute of the cell traversed decreased rapidly with increasing activity.

The diameter of the lung cell, which has an average density of $0.2-0.3 \text{ g/cm}^3$, is assumed to be approximately $12 \text{ }\mu\text{m}$, and the mean traversal length of an alpha particle is $8 \text{ }\mu\text{m}$. The total tissue range of $52-54 \text{ }\mu\text{m}$ approximately equals to an alpha particle travelling path of seven cells. The total lung range of $173-180 \text{ }\mu\text{m}$ is considered to be the alpha particle travelling path of twenty-two lung cells. Multiple traversals are assumed to be neglected when the uniform activity is distributed throughout the lung. The mean range for an alpha particle of 5.489 MeV , which produced about $50,000$ ion pairs per cm, is approximately 4 cm ($4 \times 10^6 \text{ }\mu\text{m}$) in air at STP, or about 0.018 cm in the lung.

A material, such as Aluminum which has an atomic mass of 26.98 and a density of 2.7 g/cm^3 , is used as a shield to stop the alpha particle of 5.489 MeV . The alpha particle range in Aluminum (R_{Al}) can be determined, where the alpha particle range in air is 4.186 cm . The density and the atomic mass of air are $1.225 \times 10^{-3} \text{ g/cm}^3$ and 28.964 g/mol at 15°C and 1 atm , respectively.

$$R_{Al} = 2.3 \times 10^{-4} \left[\frac{\sqrt{26.98}}{2.7} \right] (4.186 \text{ cm}) = 18.5 \times 10^{-4} = 0.00185 \text{ cm} = 18.5 \text{ }\mu\text{m} \quad (4.18)$$

Therefore the shielding of Al material must be $\geq 18.5 \text{ }\mu\text{m}$ thick to stop the alpha particle of 5.489 MeV .

When radon enters through the nasal passages, the cells in the bronchial epithelium are targeted mainly by the short-lived decay products which are deposited along the

bronchial airway surface (National Research Council, 1999b). The dose to targeted cells, from the radon gas, is less than that from its daughters' products because of the location of the radon as it decays along the airway passages. There is a low probability that the alpha particles will interact with the cell, but the decays products are on the surfaces within about 20-30 μ m of these target cells, so there is higher probability of hitting a target-cell nucleus.

The doses to the Alveolar capillaries in the lungs and the T-lymphocytes in the bronchial epithelium, by continuous exposure to 1Bq/m³, are shown by ICRP (1977, 1990) and the bronchial epithelium dose is higher than Alveolar capillaries dose in lungs by about 50 times.

4.3 ICRP model of radon particle size distribution in the respiratory system

Some radon progeny attach to airborne particles and form radon progeny aerosols. The size and distribution of these aerosol particles are important considerations in assessing the likely radiological effect on the respiratory system. The activity-weighted particle size distribution was shown by Porstendorfer J et al., (1979). The attachment coefficients for ²²²Rn decay products to any size of particle can be calculated. The activity-weighted particle size distribution is considered as the product of number size distribution and the probability of attachment for unattached radon decay products (BEIR VI, 1999). The size of aerosol radon particles increases in aerated-water, for example in a shower, or in high humidity, such as in the lung. The diameter of the particles, before and after showering in the bath, is different. The activity weighted size of particle diameter of 50 nm prior to showering, is increased to 80nm after showering. The larger particles are shown to be less efficient at delivering a dose to bronchial tissues due to the dampness.

Therefore water molecules can affect the efficiency of dose distribution in terms of humidity, temperature and dew point temperature of the system. The solubility of ^{222}Rn in water at the body temperature is about 0.000122 mole fraction of gas mixture (Lide, 1996).

Deposition efficiencies must also be considered from animals and human measurements in relationship with particle size, specific dissolution rate of inhaled material, attached/ or unattached aerosol, retention in airways, airways dimension, the sensitive tissue and cells to radiation-induced cancer as targets, and airflows as inspiration and expiration rates (breathing rate).

Tissues	Lung w_T (ICRP60)	Apportionment factors (ICRP66)
Extra-thoracic region (ET) (target basal cell nuclei 40-50 μm)	0.025	
Anterior nose (ET_1)		0.001
Posterior nasal passages, pharynx, larynx mouth (ET_2)		0.998
Lymphatics (LN_{ET})		0.001
Thoracic region	0.12	
Bronchial (BB) (target secretory 10-40 μm and target basal cell nuclei 35-50 μm)		0.333
Bronchiolar (bb) (target secretory cell nuclei 4-12 μm)		0.333
Alveolar, interstitial (AI)		0.333
Lymphatics (LN_{TH})		0.001

Table 4.1: Lung w_T in from ICRP60 and Apportionment factors from ICRP66

The measurements are assessed as mechanical transport clearance in terms of aerodynamic processes such as gravitational settling and inertial impaction, and the thermodynamic process of diffusion (Roy, 1996). The weighting and detriment apportionment factors in the airways were recommended by ICRP publication 60 (ICRP, 1990) and ICRP publication 66 (ICRP, 1995), respectively for calculations as shown in Table 4.1 (page 48).

The assumption was made that log/normal particle size distribution was used for each population and the curves were given as functions of the AMTD and also of the AMAD. In the absence of information on the particles sizes, deposited fractions are calculated for the default values: AMAD of 5 μ m for workers, and 1 μ m for the public.

Information on Solubility and Reactivity properties (**SR**) of gases and vapors were used to consider the inhaled gas molecules reaching the airways to return to the expired air only then the gases dissolved in or reacted with the surface lining. The model of gases were used as default approaches into 3 classes, **SR₀**, **SR₁**, and **SR₂**, as shown in Table 4.2.

SR ₀	Insoluble and non-reactive: negligible deposition in the respiratory tract but interact with airways
SR ₁	Soluble or reactive: 100% deposition is assumed with distributions of 10% ET ₁ , 20%ET ₂ , 10%bb, 20%BB, and 40%AI
SR ₂	Highly soluble or reactive: total deposition and instantaneous translocation to blood

Table 4.2: SR₀ (Insoluble and non-reactive), SR₁ (Soluble or reactive), and SR₂ (Highly soluble or reactive) parameters.

The additional information of solubility is also reported by Fogg and Sangster (2003). The default absorption rates were classified into 3 classes for half-times of 10 minutes

within F-type, M-type and S-type as rapidly, rapid, and slow absorption types, in order to determine default absorption parameters, as shown in Table 4.3.

	Rapidly	Rapid	Slow
F: 100% dissolved within 10 minutes	1	100	-
M: 10% dissolved within 10 minutes, then 90% remaining 140 days	0.1	100	0.005
S: 0.1% dissolved within 10 minutes, then 99.9% remaining 7000 days	0.001	100	0.0001

Table 4.3: F, M and S Parameters

Radon in the form of waterborne radon can also contribute to overall radon exposure. Waterborne radon is primarily from groundwater sources (NRC, 1999a) such as wells rather than from rivers. The waterborne radon to air is 10,000:1. EPA establishes an action level if radon is at or over 4.0pCi/L. The Committee on the Biological Effects of Ionizing Radiation (BEIR) established the value of a dimensionless parameter, k-factor, that characterized the comparative dose to lung cells in the home and in mines for the same exposure (NRC, 1999b). It was found that the doses per unit exposure in mines and homes were essentially the same. K-factor used in risk projections is calculated to be about 1 for men, women and children (age 10 years), and slightly above 1 for infants (age 1 year). Laboratory studies using different species of radon-exposed animals clearly show a linear dose-response relationship between radon and lung cancer.

The difficulty in estimating the annual dose from natural sources is an estimate of a dose conversion factor for ^{222}Rn . Dose conversion factor for ^{222}Rn in the equilibrium with its progeny varies between 6-15 nSv per Bq hr m^{-3} (Grasty and LaMarre, 2004). The

United Nations Scientific Committee on the Effects of Atomic Radiation (UNSCEAR) recommended using the dose conversion factor of 9 nSv per Bq hr m⁻³. Therefore the indoor annual effective dose from ²²²Rn in equilibrium with its decay products can be obtained as, by assuming a person spends 7000 hr in door in a year,

$$^{222}\text{Rn} (\mu\text{Sv}) = (11.4\text{Bq m}^{-3})(7000\text{hr})(9 \text{ nSv per Bq hr m}^{-3}) = 718 \mu\text{Sv}$$

where the EEC (Equilibrium Equivalent Concentration) of ²²²Rn for 19 cities in Canada, using

$$\text{population-weighted average of } ^{222}\text{Rn in door} = 11.4\text{Bq m}^{-3}.$$

The radon inhalations measurements were suggested and measured in percentage of micro-nucleated and bi-nucleated alveolar macrophages of rats, exposed to the radon at high and low equilibrium of aerosol (Morlier et al., 1996). It was found that the reading of radon, as a micronuclei index in micro-nucleated alveolar macrophages was always lower than in multinucleated alveolar macrophages. The radon measurement at low equilibrium in micro-nucleated alveolar macrophages (1.47±0.42 %) was higher than at high equilibrium (1.22 ±0.26 %), but at low equilibrium in multi-nucleated alveolar macrophages (2.30 ±0.78 %) it was lower than at high equilibrium (2.91 ±0.74%).

The radon concentration in the bronchial and the bronchiolar regions of lungs was reported by Leonard (2007) in terms of the enhanced deposition effect (EDE) of lung dose reduction. The EDE of radon, as a function of relative humidity or airborne water density, decreased while the airborne water density increased as a result of the influence of the relative humidity.

CHAPTER 5

The Measurement of Radon by the Fiber Optic Scintillating Detector

In general most radon (Rn^{222}) measurements provide adequate information on the upper limit for radiation exposure in an essential health risk assessment, due to the radon progeny as a function of time and space. Airborne radon and its newly created daughters have high electrical charges, especially Po^{210} , which causes a substantial fraction to become attached to dust, water and other aerosol particles in air. They are also deposited on the wall surface in the vicinity of their passages. The properties of radon due to solubility can play an important role in detection. The solubility of radon also depends on the temperature within the detector. Therefore the humidity and temperature can affect the concentration of radon detected according to its solubility and also its surface deposition (adsorption) along its passage.

The basic principle of the experiment in the present study (for Schematic of the equipment see Figure 5.1, page 58) was based on a large sample representing the whole population, within the minimum time while maintaining the reasonable statistics, for the minimum detectable radon concentration < 4 pCi/liter. The instrument was originally designed and built by Kim (1995) as presented by Kim et al. (1995).

5.1 The fiber optic scintillating detector

The rare-earth doped silicated glass compositions of Si, Mg, Al, Ce, and Li oxides (Schott R-4) were used in the construction of the porous glass fiber bundle, acting as a scintillator. The melt of compositions was performed in a controlled environment to control the cerium ions to be the trivalent state as Ce^{+3} . The maximum optical excitation occurred at 351 nm with the refractive index of 1.51. The glass density was 2.34 g/cm^3 .

The Schott R-4 had a light output efficiency of 1.2%. The glass was drawn into fibers of $50.22 \pm 0.77 \mu\text{m}$ diameter to obtain the efficient capture of the radiation from ^{222}Rn . The close-packing of the 7387 fibers in length of 6.9 cm was constructed into a rectangular fiber bundle of $6.9 \times 12.2 \times 2.4 \text{ mm}$. It provided the pore volume of 0.865 cm^3 and surface area of 0.08 m^2 . The center line of the fiber bundle was positioned parallel to the axis of a Hamamatsu (R268) cylindrical photomultiplier tube (PM-tube) in order to produce the optical wave-guided effect, which directed 66% of the escaped photons from the glass fibers back into the PM-tube. It is concluded (Kim et al., 1995) that 66% of the scintillation light is guided within the glass fibers and only 17% is reflected at the air-fiber boundary.

A reflecting surface of polished aluminium foil ($1 \mu\text{m}$ thickness) was used as a reflector on the compartment around the fiber glass bundle, in order to reflect all of the escaping photons and the overlapping spectrum between the emission and excitation spectrum. The PM-tube and its preamplifier were mounted in a gas-tight and light-tight aluminium chamber, through which the radon-laden air could be circulated by the use of peristaltic pump (B in Figure 5.1, page 58). The fiber optic scintillating detector (D in Figure 5.1) was placed in a large metallic chamber (16" diameter x 60" length) in order to keep the humidity of the air constant and also to isolate it from the humidity of the room air. Three electrical connections for high voltage, for power supply of the PM preamplifier, and for signal lines, were passed through the wall of the chamber and were also sealed by epoxy glue. The chamber was housed in the refrigerator, which had a heater circuit along its inner wall. The temperature within the freezer was regulated by the temperature differences detected from the thermocouples, using a Therm-O-Watch

model TC2-1000 as a temperature control device. If the temperature was lower than the desired temperature setting, the heater was switched on to keep the constant desired temperature.

5.2 The radon source (Pylon), the Humidity flask, and the Dryer (Dehumidifier)

The radon source providing 1.024×10^{10} atoms of ^{222}Rn at the secular equilibrium, was a Pylon module (RN1025) unit with 21.5 kBq of ^{226}Ra source. In order to trap and eliminate the effects of the radon progeny, 25 mm diameter Whatman glass fiber filters, of 0.8 μm pore size, were placed before the valve inlet (R in Figure 5.1) and also after the valve outlet (W in Figure 5.1) of the radon source, along the air passage of the system.

The Humidity flask (V in Figure 5.1) was a pyrex glass bottle (Pyrex part number 31760-25080) with a coarse fritted disc (Pyrex part number 31760-250CSO). The flask (250cc) was filled with water. Air was pushed through the inlet, and went through the coarse fritted disc causing the air to form into fine bubbles. The fine bubbles approached the water surface, and the aerosols carrying water molecules, then exited the flask to T (in Figure 5.1).

The Dryer (Dehumidifier), an air-tight plastic canister about 12 inches long with inlet and exit (M and L in Figure 5.1, respectively), was filled with DRIERITE (anhydrous calcium sulfate) which was 10-20 mesh size. When aerosols entered into the dryer, the water molecules were absorbed onto the calcium sulfate. Only the dried air exited.

5.3 The Multichannel Analyzer (MCA)

The scintillations produced by the radiation interactions were detected by a PM tube operating at the optimal voltage of +650V. In general the ASA-100 (Canberra Industries Inc., Meriden, USA), which was a PCI bus Multichannel Analyzer (MCA), can supply a

preamplifier voltage of $\pm 12\text{V}$ (50 mA) and high voltages (HV) up to 1,000 volts to any NaI detector. It managed the data acquisition up to 2048 channels by 80 MHz Wilkinson chip. The parameters required for data acquisition could be set up as shown in Table 5.1. Due to the degradation of the NaI crystal over a number of years, there was an increasing drift of the dark current, therefore the data collection was confined to the channels outside the dark current.

ADC	Stabilizer	Amplifier	PowerSupply
LLD=12.3%	"ON"900 channels	"ON"Amplifier	HV=650volts
ULD=100%	GainCentroid=900	CoarseGainx256	
	GainSpacing=246	FineGainx2.5	

Table 5.1: The setup parameter of ASA-100 in the PAMS software.

The signal was collected and amplified by the MCA with the gain of 2.5×256 . The ASA100 was controlled by PAMS (PARAMETER MONITOR Software) data acquisition which operated within Genie 2000 software platform (Canberra Industries Inc., Meriden, USA), under the Microsoft-XP operating system. The acquisitions were recorded and displayed as multiple graphic modes in count rate and counts. The dwell time of the MCS (Multi Channel Scaling) mode was fixed to 25 sec to correspond to the recording time of the humidity (%), temperature ($^{\circ}\text{C}$), temperature ($^{\circ}\text{F}$), dew point ($^{\circ}\text{C}$), and dew point ($^{\circ}\text{F}$). The data were collected over at least a week for each individual experiment, during which the radon Pylon valve was on for 5-6 days and off for 2-3 days. The minimum required for the radon "ON" to reach the steady state was 2 days. The data were analyzed using PC computers.

Concurrently the humidity, temperature and dew point were observed (E in Figure 5.1) and recorded in the long-term through the ADC by IBM PC-based. All data were recorded using the Procomm-Plus software (Symantec Corporation, Cupertino, USA).

5.4 Preamplifier for the PM of the Detector

The power supply of the PM tube preamplifier was constructed as internal ISA and PCI power supplier cards, as shown in Figure 5.2 (page 59), in order to supply -24V to the preamplifier circuit of the PM tube in the detector. A Corsel (Corsel USA Inc., San Jose, USA) DC-DC converter, ZW3-2412, was used for the conversion of voltage from 12V to 24V, and vice versa. The ZW3-2412 was considered as a Fly-back converter circuit method with a switching frequency of 250-1400 kHz. The 12V was obtained through the PC bus of ISA or PCI. The single output of pin connection was arranged without a capacitor near the input terminal, because the ZW3-2412 has an input filter already built-in. The noise, created by the converter input, could be reduced by the formation of the π type filter if the capacitor was connected near the input ($\pm 12V$) terminal. The capacitor of 100 μF (50V) was connected at the output ($\pm 24V$) terminal to lower the ripple voltage.

The average current of output, $I_{avg} = (I_{peak} - I_{steadystate}) (t/T_{period})$, where t = time.

The other capacitor of 0.1 μF (50V) was also connected externally at the load when the distance between the load and the DC output was long.

The external capacitor, $C_{ext} = (I_{peak} - I_{avg}) (t/\text{Fluctuation of output voltage})$

Pin 6 of the DB9F (Figure 5.2) was externally connected to the output of -24V so that the -24V could be used to supply the voltage to a Bicorn (Bicorn, Newbury, USA) Photomultiplier tube (PM), and pin1 of the DB9F is grounded. The DC-DC converter, NDTD2412, was used for the PCI card instead of the ZW3-2412 because the latter was unobtainable. There was very little difference in the circuits of the NDTD2412 (on PCI card) and the ZW3-2412 converters (on ISA card). When using the ZW3-2412, a

capacitor of 47 μf (25V) was needed between the output terminal and the common point to lower the output voltage from -26.87V to the desired -24V, and also the capacitor of 10 μf (25V) was placed between the input terminal and the ground, to stabilize V_{in} and to make sure that it stabilized at -24V.

5.5 The connection of the system

The circulation passage (Figure 5.1), with a diameter of about 0.25 inches, was copper or stainless steel tubing or clear tygon rubber tubing that could hold pressure upto 3 psi. The tygon rubber tubing was encased in butyl black rubber tubing, to prevent the escape and leakage by the diffusion of the air through the rubber material, except at the electrical peristaltic pump. The radon Pylon (W in Figure 5.1) was connected directly to the air ion counter 1 (C in Figure 5.1) with the peristaltic pump (B in Figure 5.1), to control the flow speed of the radon-laden air before entering the fiber optic scintillating detector (D in Figure 5.1). The relative humidity detector was connected at the exit of the fiber optic scintillating detector to the air ion counter 2 (EFGH in Figure 5.1). The air ion counter 2 was then connected to the Anemometer (I in Figure 5.1) of the Control Company which measured the speed of air circulation in ft/min. All lengths between point-to-point connections are shown in Figure 5.1. Five 3-way valves were located at S,A,T,J,K,O and N in Figure 5.1. These valves were used to change the direction of the radon-laden air without reconnection, in five different ways (Figure 5.1);

- 1) When the measurement was in progress at controlled temperature,
the route was I-J-K-T-X-U-S-R.
- 2) When the decreasing level of relative humidity was required at controlled temperature, the route was I-J-O-N-M-L-K-T-X-U-S-R, (routing through dryer).

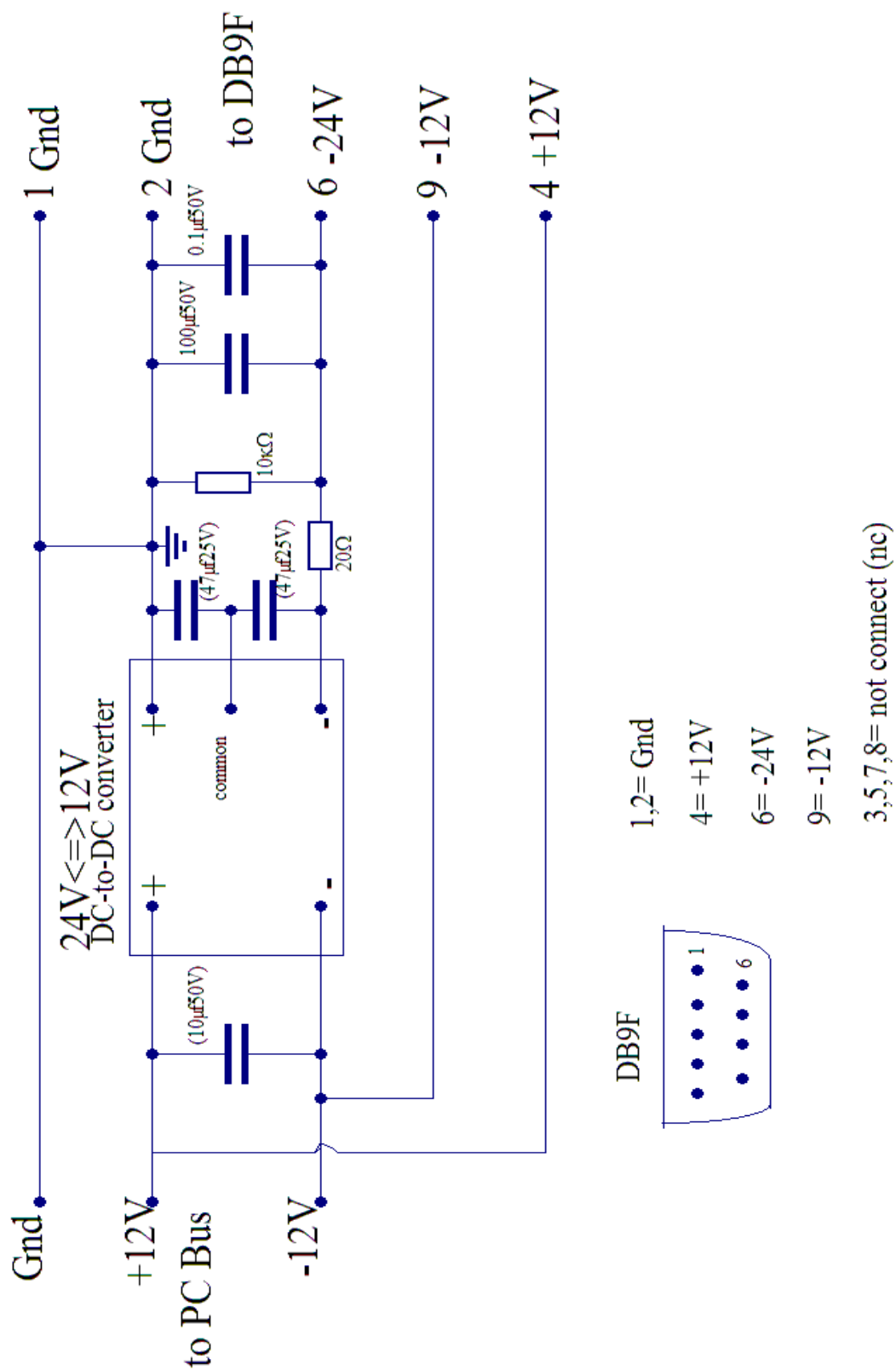


Figure 5.2: Circuit of the power supply for the preamplifier of the PM

- 3) When the increasing level of relative humidity was required at room temperature, the route was I-J-O-P, and (with humidity flask)-V-T-X-U-S-R.
- 4) When the clearance of the radon from the radon-laden air was required at room temperature, the route was I-J-O-P, and (without humidity flask)-V-T-X-U-S-R.
- 5) When the relative humidity (0%) was required, the route was I-J-O-P, and (nitrogen gas)-Q-N-M-L-K-T-X-U-S-R.

When the radon pylon valve was turned on, the route was U-S-R-W-A-B. If the radon pylon valve was turned off, the route was U-S-A-B.

5.6 Operation and Data Collection

At the beginning of the experiment, air was circulated from S to R (Figure 5.1, page 58) and entered the radon pylon. The air was mixed with the radon particles and exited at W to A. The radon-laden air passed through the peristaltic pump and then entered the air ion counter 1, at C, before entering the fiber optic scintillating detector at D. The measurement of the radon in counts per minutes (cpm) was obtained by the Multi-Channel Analyzer. The relative humidity, RH (%), temperature and dew-point temperature were measured when the radon-laden air exited from the fiber optic scintillating detector. The flow was then directed through the route E-F-G-H, and entered the air ion counter 2. The speed of flow was measured at I after the radon-laden air exited the air ion counter 2. The radon-laden air flowed along I-J-K-T-X-U and entered the air ion counter 3 before entering into the radon pylon along U-S-R-W to complete one cycle of flow.

The measurement of radon in cpm was recorded every 25 seconds for each data, until the steady state was reached, then the radiation source or the radon pylon valve was turned off by manipulating the valves at S and A. The cpm was obtained and plotted against time. The long term data are shown in Figure 5.4 (page 66). At the beginning of the measurement, there is a rise of the counts to a maximum peak (Figure 5.5, page 67), which was followed by multiple peaks of decreasing amplitude until reaching a saturation region. After the saturation region was reached, the graph gradually showed steady decline until it approached the steady state, due to the dispersion of the radon-laden air. As the steady state or the equilibrium approaches, the graph showed a nearly flat plateau at time over 2,000 minutes (Figure 5.4, page 66) or over 2 days. The radon-laden air was uniformly distributed within the system.

Multiple experiments were conducted at each controlled temperature. Data from each experiment was recorded but only the data from the steady state plateau was selected for further analysis, to obtain radon (cpm) as a function of relative humidity, at each controlled temperature. This was then plotted in a 2D graph using TableCurve-2D (Systat software Inc., Chicago, USA) to obtain the curve of best fit between the relative humidity (RH%) and the predicted values of radon (cpm) from all data of all experiments obtained by the fiber optic detector. The temperature ranges of 4-17, 16-23, 25-37, and 30-50 °C for curves between RH% and cpm are shown in Figure 5.3 (page 65). The graph showed the highest cpm of radon at low humidity and then the cpm decreased as the humidity increases. The cpm increased at about 30% humidity and then decreased again after about 50% humidity.

Data from the experiments, graphed in Figure 5.4, with radon in cpm and in ions/sec as a function of time (min), showed the highest maximum peak at the initial release of the radon and then a decrease. During the time of the maximum saturation peak the radon filled into the compartment in the system. Then the graph goes down because some of the radon attached to the wall of the compartment and the fiber optic tubing in the detector and also as a result of radon decay. After about 2000 minutes, when the radon reached equilibrium, the graph showed a steady state plateau (Figure 5.4)

The further general model could be considered using SYSTAT package (Systat software Inc., Chicago, USA) to model a nonlinear curve function relating between the counts, temperature and the relative humidity which were based on the best fit 3D-equation by TableCurve-3D (Systat software Inc., Chicago, USA) as an initial guideline.

5.7 Modeling and Data Analysis

A flow chart of the step by step model procedure is shown in Figure 5.6, page 68. The data of water vapor weight per weight of dry air was obtained and shown in Appendix F. This data was used in the model to represent the maximum influences of water to radon in the system. The parameter used in this model was the weight of water in the steady state, per the weight of air which was saturated entirely in the system. To estimate the model of the water behavior in statistics, the Gauss-Newton method of least square estimation which is nonlinear regression was used.

The best fit of model could be obtained from this data in form of, $Z=a+b[\text{Ln}(X)]+cY$, or

$$Z= \text{Ln}[\text{water vapor weight in the dry air}]= a+b[\text{Ln}(\text{RH}\%)]+ c[\text{Temperature}] \quad (5.1)$$

where $a= -1.2438$, $b= 0.9687$, $c= 0.0653$, and $r^2= 0.995$.

So it could be stated that this equation represented a model of water influence to water, or adsorption of water to water, at maximum or almost 100% with r^2 at 0.995.

The same non-linear model was applied to the radon data obtained from the experiment. The parameter measured expressed in term of logarithm, could also represent the water influences to the model. The radon measurement could be expressed as, $\text{Ln}[\text{the percentage of (cpm of the radon at the equilibrium/the cpm at the maximum saturation peak)}]$. The assumption was made that if there was maximum adsorption of radon to the water in the closed loop system, then r^2 will be close to 1.00. If there was minimum adsorption of radon to the water in the closed loop system, then r^2 would be close to 0.00. If the behavior of radon was dictated by the water behavior, such as the expansion by high temperature, highest density of water at 4-7 °C etc., it meant that the model should give the same perfect fit to the radon measurement at any T and RH(%), when the data of the radon measurement was used in the same model as for water.

Model	r^2	a	b	c	d	e	f
Water	0.995	-1.244	0.969	0.065	n/a	n/a	n/a
Rn (RH 0-60%)	0.138	-1.244	0.969	0.065	5.419	-1.092	-0.006
Rn (RH 0-15%)	0.084	-1.244	0.969	0.065	5.410	-1.206	-0.022
Rn (RH15-25%)	0.333	-1.244	0.969	0.065	3.521	-0.501	-0.051
Rn (RH 25-45%)	0.508	-1.244	0.969	0.065	8.883	-1.925	-0.072
Rn (RH 45-60%)	0.358	-1.244	0.969	0.065	9.134	-2.019	-0.064

Table 5.2 Values of best fit (r^2) of water and radon.

If the radon was influenced 100% by the water, the data measured must have behaved the same as water molecules in the model and also be able to fit the same equation of $Z=a+b[\text{Ln}(X)]+cY$, with the same best fit in 3D model, $r^2=0.995$. The deviation from the best fit of the model, represented the deviation of the influence or adsorption from the

water molecules to the radon particles. The data of radon measurement was analyzed with an identical equation, which was obtained from the water model, with the extra deviated term of $d+e[\text{Ln}(\text{RH}\%)]+ f[\text{Temperature}]$.

$$Z= a+b[\text{Ln}(\text{RH}\%)]+ c[\text{Temperature}]+ d+e[\text{Ln}(\text{RH}\%)]+ f[\text{Temperature}] \quad (5.2)$$

$$Z= \{-1.244+0.969*[\text{Ln}(\text{RH}\%)] +0.065*[\text{Temperature}]\} \\ +\{d+e[\text{Ln}(\text{RH}\%)]+ f[\text{Temperature}]\} \quad (5.3)$$

where Z is $\text{Ln}[\text{cpm at steady state/cpm at the maximum saturation}]$ in the radon data.

The value of r^2 obtained from the modeling of water and radon are listed in Table 5.2 (page 63). Whenever the degree of best fit (r^2) showed a less perfect fit for radon, this implies that less adsorption of water to radon (or radon to water), or less water influence to dictate the pattern of radon behavior within the closed loop system.

The following is an unconventional way to use the model to estimate, semi-quantitatively, the influence of humidity on radon detection. The highest degree of fitness ($r^2=0.995$) represented the maximum influence of water. For the low RH (0-15%) or low amount of water, the value of r^2 was 0.084. When the RH increased (to 15-25%) the r^2 was increased to 0.333, and at the higher RH (25-45%) the r^2 was 0.508.

The lower the degree of fitness, the less adsorption of water to radon could be suggested at lower relative humidity of 0-15% (Table 5.2). The degree of radon/water interaction increased as RH(%) increased from 0%, peaks at 25-45%, and decreased with higher humidity. As the amount of water increased the degree of radon/water interaction increased from 0-45% and then decreased from 45-60%. This correlated with the radon (cpm) measurement that also decreased with the higher humidity because of the adsorption of the water to radon (Figure 5.3, page 65).

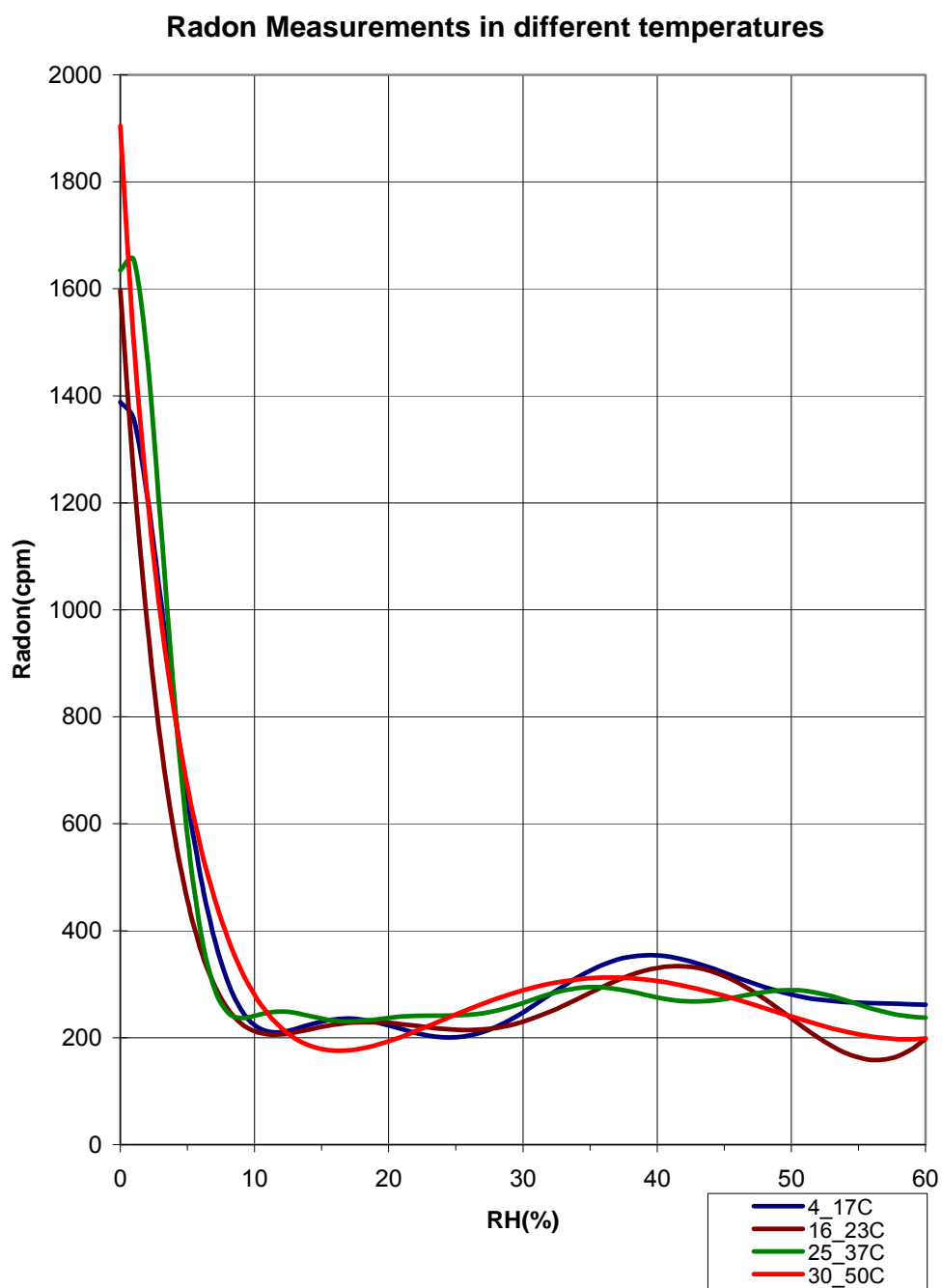


Figure 5.3: Radon Measurement in different temperatures.

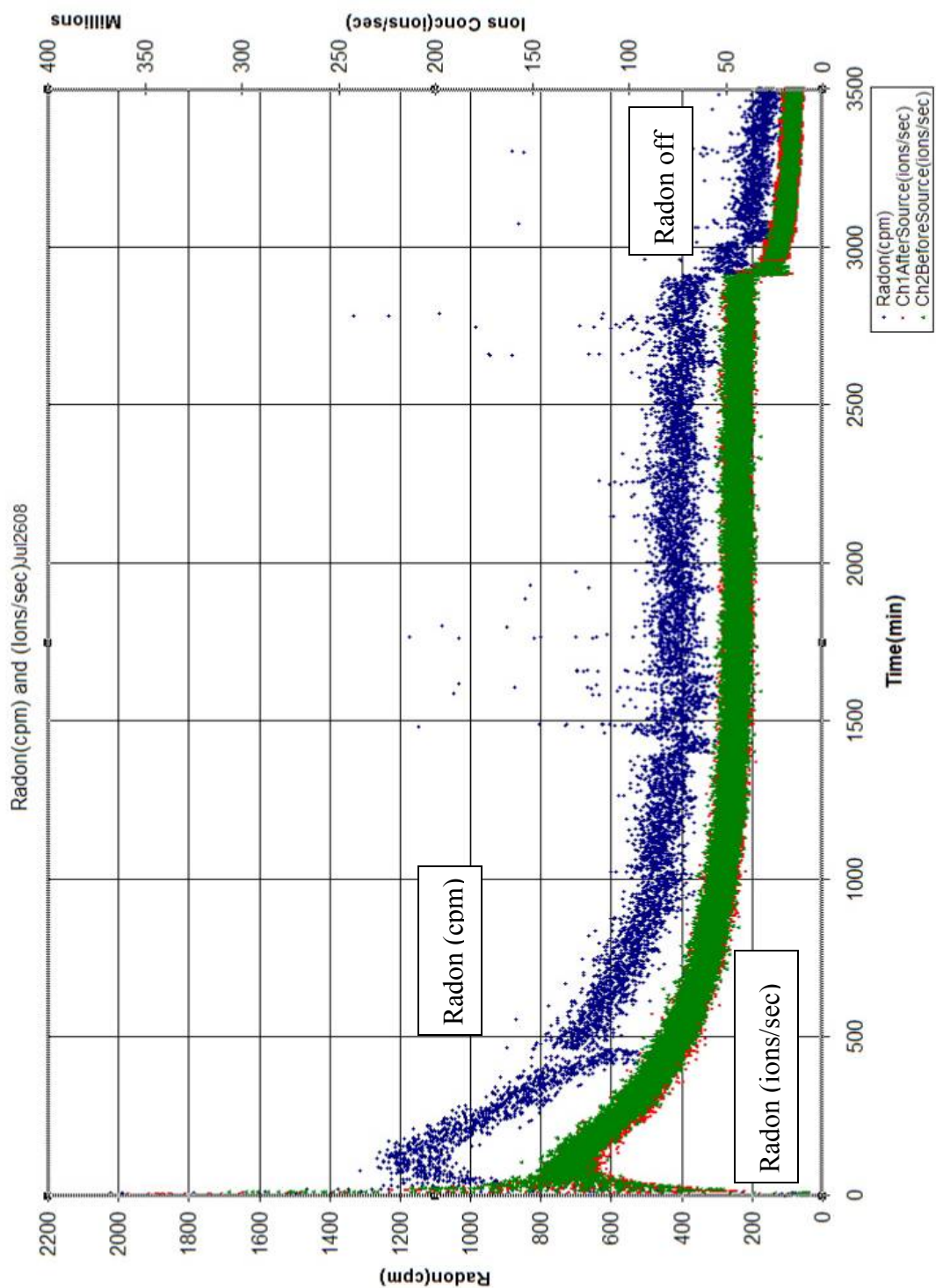


Figure 5.4: Radon (cpm) by the fiber optic detector and ions (sec^{-1}) by the air ion counters over time (min)

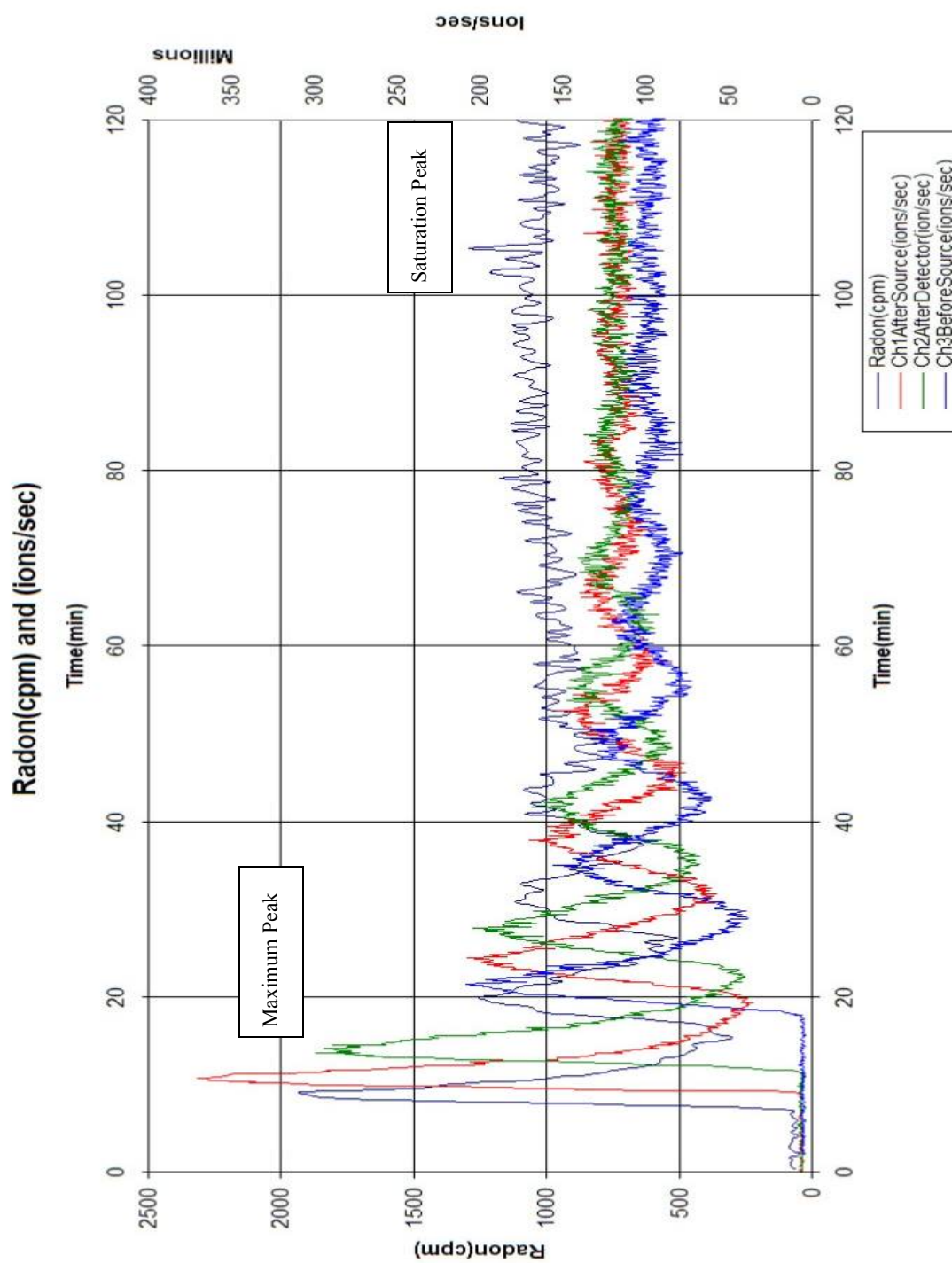


Figure 5.5: Maximum Peak and Saturation Peak of Radon (cpm) at the beginning

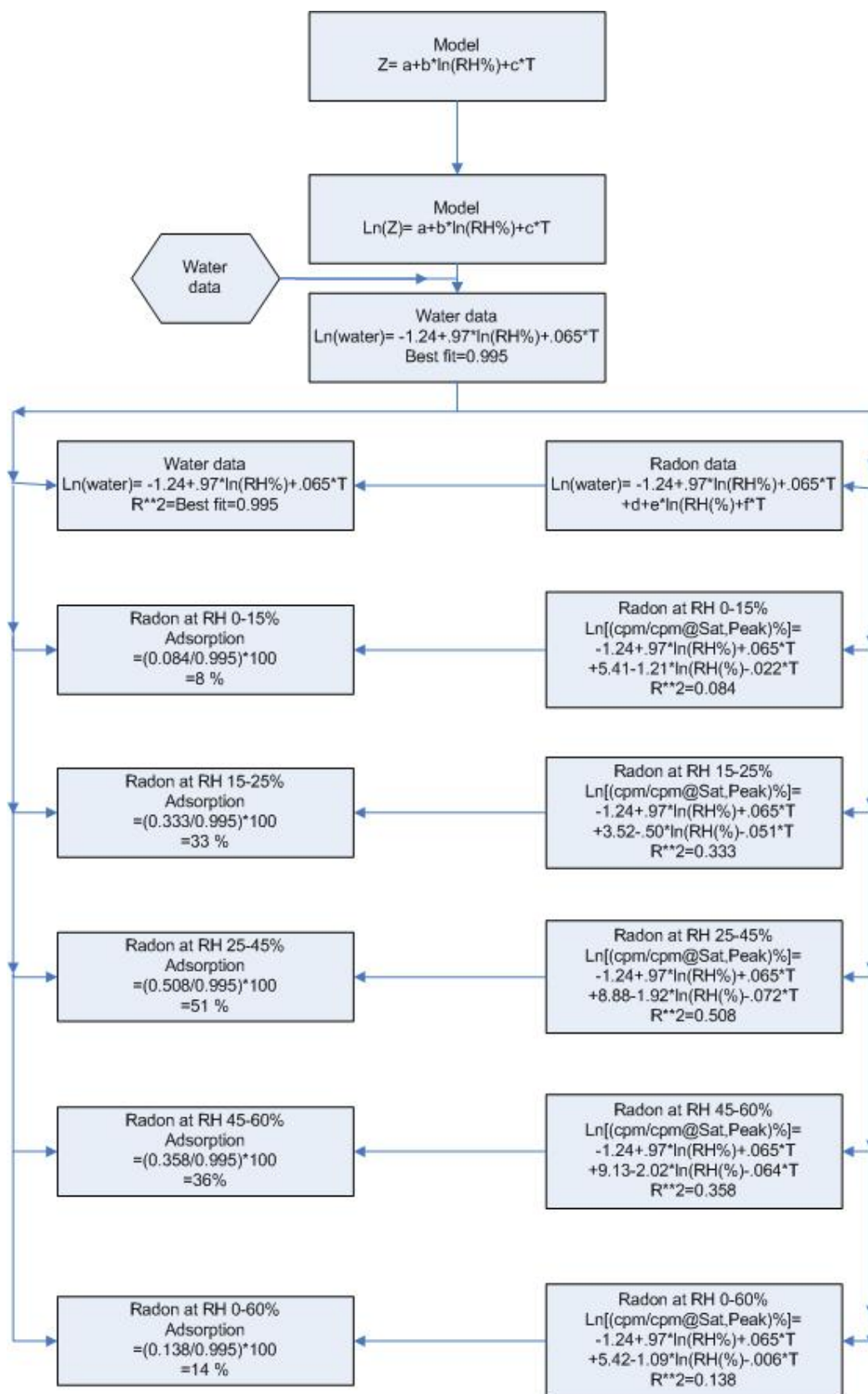


Figure 5.6; Flow Diagram of Model

CHAPTER 6

The air ions measurement

The measurement of air ions distribution can be achieved by several methods, such as the dispersion method, the ion spectrometer method, the Faraday cage method, and the Gerdien tube method (Vojtek et al., 2006).

6.1: The Basic design of the Gerdien tube detector

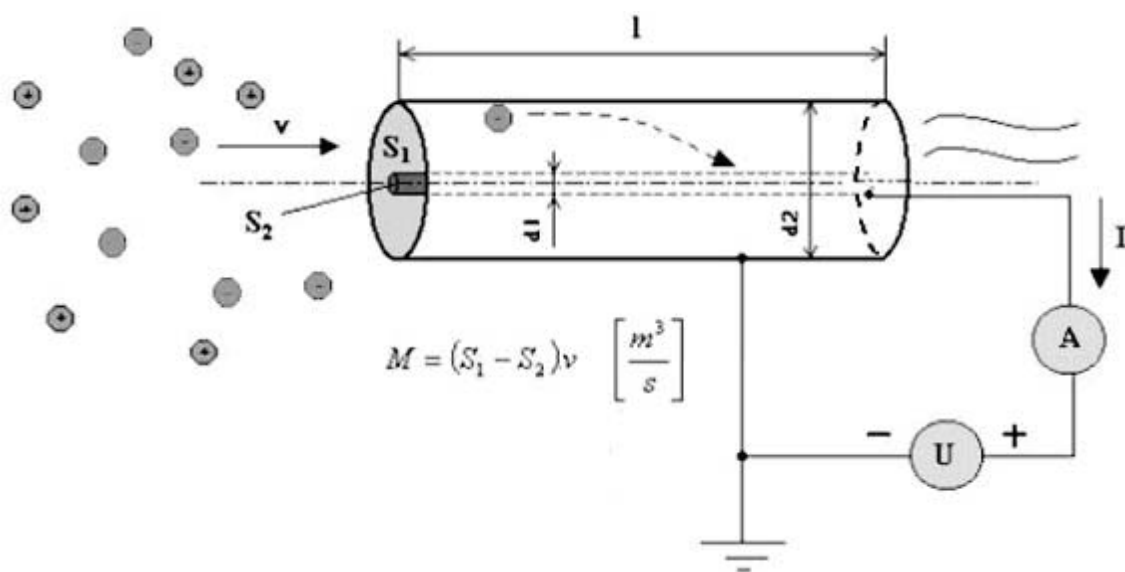


Figure 6.1: The basic design of the Gerdien Tube method
(Vojtek et al., 2006)

The basic design of the Gerdien Tube method is shown in Figure 6.1. This method was used to measure the amount of positive or negative ions in the air, after the air was ionized by the radiation. The method was based on the separation of positive and negative ions in the electric field between two electrodes of positive and negative polarity. The inner electrode (the collector) was located at the center of the collection compartment and the outer electrode. The tubing adapter was the rectangular shaped inner compartment (5x7x1.4cm), which was specially designed by the Alpha Laboratory

(Lee, 2008) for this research. Both electrodes were situated within this compartment. When the air ions flowed into the compartment of the tubing adapter, the ions in the electric field impact the collector, then the current produced was measured by the picoampere-meter. The tubing adaptor for the air ions counter were air-sealed to prevent leakages of radon gas. This air ions counter detector required a flow of at least 400 cubic cm per second, due to the limitation of the circuitry. The minimum resolution of 10 ions/cubic cm was achieved and requires an input of about 8000 ions/sec.

The electric field was produced by the voltage source of U . The charged ions in the electric field impact the collector and the current produced was measured by the picoampere meter. The number of ions per cubic cm, n , could be obtained by,

$$n = \frac{I_{out}}{eM} \quad (6.1)$$

where I_{out} = the output current measured by the picoAmpere-meter

l = the length of the Gerdien tube (in Figure 6.1)

M = the air flow volume rate = $(S_1 - S_2)v$ in $\frac{m^3}{s}$

e = the elementary charge of electron: + positive or –negative air particle (ion)

S_1 = the surface area of the outer electrode with diameter of d_1

S_2 = the surface area of the inner electrode or the collector with diameter of d_2

v = the air flow velocity through the Gerdien tube in $\frac{m}{s}$

R_u and C_u = input resistance and capacitance of the voltage source

R_V = the insulating resistance of the collector voltage source

R_{AK} = the leakage resistance of the Gerdien tube

$R_{EH}, C_{EH}, R_{EL}, C_{EL}$ = the leakage resistance and capacitance of picoAmpere-meter

(Figure 6.2)

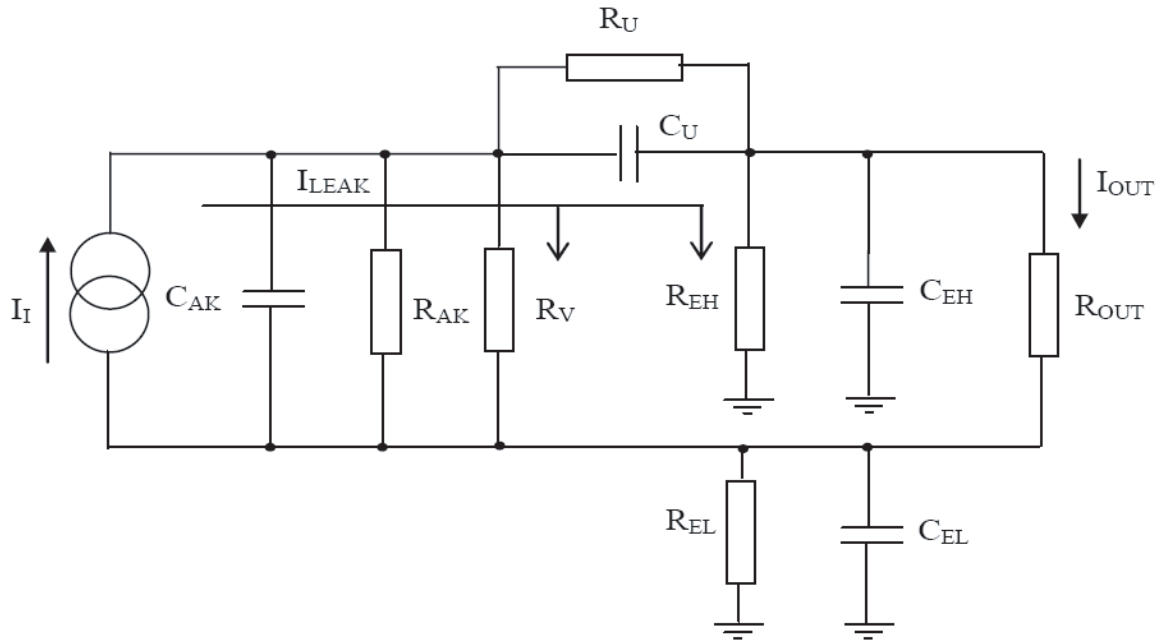


Figure 6.2: The basic circuit of the Gerdien Tube method
(Vojtek et al., 2006)

The estimate of 50,000 ions per an alpha particle was obtained by Lee B (2008) from measuring ^{241}Am . It was also assumed that one ^{222}Rn decay releases about 50,000 + and - ion pairs. But not all will be detected. Many of the alpha particles collided with walls or dust in the collecting compartment before releasing the full energy into air, or ion pairs spontaneously recombined, a number as small as 35 eV/ion pair was reasonable if the air is clean, no surfaces were nearby, and there is no recombination. Otherwise, much of the energy would be absorbed by other things, so that effectively, more than 35 eV would be absorbed per stable ion pair produced. When a 5 MeV alpha was produced in air,

approximately 100 eV of energy was removed per (quasi stable) pair (one + and one -) of air ions produced. The mean free path of the alpha was about 2 cm at standard condition for temperature and pressure (STP). Single ionized ions were much more common and stable than multiple ionized ones, so the assumption was made that only singles were present. Therefore an alpha produces about 50,000 single charged pairs if the path was fairly unobstructed. This number was ions per alpha that survive over the distance of at least (about) 2 cm in the air. Once the alpha dislodged electrons, various atoms stick to the extra electron or extra positive atom.

In this Air Ions Counter, there was a brass sheet about 5x6 cm in the center as the collector. This was the "plate". It collected the ions (only positive (+) or negative (-) at one time during a measurement, depending on the POLARITY switch). This plate was held near "zero" potential (voltage) because it was connected to zero through a 10 giga-ohm (10×10^9 ohm) resistor. The inside surface of the chamber was at a different voltage: either +10 V (if POLARITY is negative (-)), or -10 V (if POLARITY is positive (+)). If the chamber was -10V, then the plate was positive (+) with respect to the chamber. It was so positive that almost all negative (-) ions within the chamber immediately hit the plate and transfer their charge to the collector. However, all positive (+) ions stayed away from the plate. The voltage of the plate would be raised above zero if + ions were introduced, because the E-field caused all + ions in the air (between the plate and the enclosure) to hit the plate. The DC current equaled $[(1.6 \times 10^{-19} \text{ coulombs/ion}) \times (\text{the number of ions per second})]$ that hit the plate. This current, when it was multiplied by ten billion (ohms), gave the voltage at the plate. The voltage was amplified, depending on RANGE selected.

Each ion carried a charge of 1.6×10^{-19} coulomb, so there was a negative (-) current flowing into the plate, equaled to that charge multiplied by the number of negative (-) ions per sec hitting the plate. A high- impedance voltmeter measured the plate voltage, which differed from zero by an amount equal to the current x resistance [R =10 giga-ohms]. This voltage difference from zero was amplified and sent to the display and the output to the analog-to-digital converter.

Radon would continuously produce + and - ions at a current level proportional to the radon concentration. Positive (+) and negative (-) groups of atoms (air ions) could exist simultaneously in the air for a long time without neutralizing each other. They were relatively far from each other and rarely see each other's electric field. If one of these ions collided with a piece of metal, the metal would become slightly charged. These collisions happened frequently, but there was usually an equal number of positive (+) and negative (-) ions, so any metal that was near air ions usually remains approximately neutral. However, things were different if a static electric field was near the metal. Suppose the metal was very positive (+) with respect to the surroundings, then an electric field pointed outward from the metal. This would attract negative (-) ions to and repel positive (+) ions from the metal. Then the metal would become less and less positive (+). This change could be measured, and the rate of change was proportional to the number of negative (-) ions per second that hit the metal. (A high- impedance voltmeter connected between the metal & ground would show how positive (+) the metal is. If this positive (+) voltage decreased rapidly, it was because a lot of negative (-) ions were in the air.)

The external zero switch on this ion counter, showed only zeros on the display. The

output jack would be at zero \pm about 10mV which was equal to the internal offsets of the operational amplifier. Measurement range was 10 to 1,999,000 ions/cm³. The analog output ranges were ± 2.5 , ± 0.25 , and ± 0.025 volts full scale for all three knob settings of the RANGE, but the display could display only 2.0, 0.2 and 0.02 volts full scale. The sensitivity of the ion counter at the output jack was dependent on the RANGE setting. On “19.99” scale, 1 pico-ampere (pA) produced an output of 2.5 volts $\pm 10\%$. (Note that: 1 pA produced 2.5 volts, and the output was linear $\pm 0.5\%$.) On “199.9” scale, the sensitivity was 1 pA per 0.25 volt or 250 mV, and also on “1999” scale, 1 pA per 0.025 volt or 25 mV. The measurement of $960 \times 10^6 \frac{\text{ions}}{\text{sec}}$ was obtained by Lee (2008) on the full scale of “1999” range, or $384 \times 10^6 \frac{\text{ions}}{\text{sec.volts}}$. The analog-to-digital converter produced by Madgetech (Madgetech, Inc., Coontoocook, USA), was used to collect the data for over at least 4 days with the interval of 5 seconds between the data points.

6.2: Operation and Data Collection

Three air ion counters were placed at C, H and U respectively, in Figure 5.1 (page 58). When the experiment started, the software was initiated as shown in Figure 6.3 (page 78). The background reading was started and data collected at the beginning for 5 minutes before the radon was released. The red line (Figure 6.3) is for the air ion counter1 (AIC1), blue line for the air ion counter2 (AIC2), and green line for the air ion counter3 (AIC3).

Radon, which had accumulated in the radon source (Pylon), left the radon source at W (Figure 5.1) and entered the air ion counter1 (AIC1) at C (Figure 5.1). The graph for

AIC1 shown in red (Figure 6.3), increased from a1 to the highest point a2. Radon left AIC1 (a4) and entered the fiber optic detector at D (Figure 5.1). The graph of AIC1 decreased to a4. The second graph, recorded by air ion counter 2 (AIC2) shown in blue, increased from b1 after radon had left the fiber optic detector. Radon-laden air entered AIC2 at H (Figure 5.1). The second peak (b2) was shown to be lower than the first peak (a2), which meant that some of the radon ions were adsorbed to the surface of the fiber optic in the detector, or to the wall of the tubing, or decayed. The third graph recorded by air ion counter 3 (AIC3) shown in green, started to rise to c2 near the end of the first peak (a2) at the first completion of the cycle of radon-laden air in the system. The graph tended to increase in width over time as the flow of radon filled the detector compartment.

The flow was circulated and the amplitude of the peaks decreased until the system reached the equilibrium state (Figure 5.5, page 67). The system eventually reached the steady state or equilibrium (Figure 5.4, page 66) after around 2,000 minutes. At this point, the radon levels being emitted from the source and those being lost through sorption and decay were about equal.

6.3: Data analysis

The data measured in voltage, obtained by all three air ion counters, was converted to ions per second as shown in Figure 6.3 (page 78). The conversion factor was 960 million ions per second per 2.5 volts or 384 million ions per second per volt. The area under the curve of the first six peaks equal to 1,000 data points of each air ion counter was derived by SYSTAT statistics software, as shown in Table 6.1 (page 76). The area represented

the amount of radon ions in the positive polarity detection. The curve of the air ion count behaved similarly to the curve obtained with the fiber optic detector shown in Figure 5.4.

Detector	Total ions	P1(ions)	P2(ions)	P3(ions)	P4(ions)	P5(ions)	P6(ions)
AIC1	6.7162E+11	8.7568E+10	9.4189E+10	9.2223E+10	9.6863E+10	1.0759E+11	9.5456E+10
AIC2	6.6186E+11	8.5514E+10	8.8795E+10	9.0985E+10	9.2145E+10	1.0543E+11	9.4761E+10
AIC3	5.1787E+11	7.0495E+10	7.9995E+10	7.4136E+10	8.6683E+10	7.8310E+10	9.4210E+10
AIC1	N/A	N/A	N/A	N/A	N/A	N/A	N/A
AIC2	4.7873E+11	1.1168E+11	6.4150E+10	6.1995E+10	1.1861E+11	6.5300E+10	5.7711E+10
AIC3	3.8692E+11	8.9369E+10	5.0017E+10	4.7611E+10	5.3327E+10	4.7183E+10	4.1910E+10
AIC1	6.1947E+11	7.3020E+10	7.2578E+10	7.5370E+10	7.6358E+10	7.5657E+10	7.9788E+10
AIC2	5.7628E+11	6.8832E+10	7.1356E+10	7.4305E+10	7.4709E+10	7.2923E+10	7.2819E+10
AIC3	4.8429E+11	5.7946E+10	6.6036E+10	6.2693E+10	6.7402E+10	6.1723E+10	5.8106E+10
AIC1	2.2996E+09	3.7405E+08	3.8754E+08	4.0295E+08	3.9718E+08	4.3493E+08	N/A
AIC2	2.1732E+09	3.6887E+08	3.7866E+08	3.8784E+08	3.9373E+08	4.1886E+08	N/A
AIC3	1.7012E+09	2.9626E+08	3.2670E+08	3.3761E+08	3.4550E+08	3.8338E+08	N/A
AIC1	N/A	N/A	N/A	N/A	N/A	N/A	N/A
AIC2	4.7873E+11	3.1878E+10	8.0583E+10	5.7961E+10	5.8793E+10	6.4653E+10	6.7919E+10
AIC3	3.8692E+11	1.0860E+10	5.6748E+10	5.2962E+10	5.3398E+10	5.1164E+10	6.0613E+10
AIC1	1.2836E+09	1.1002E+08	1.0361E+08	1.1455E+08	1.2714E+08	1.2092E+08	1.0780E+08
AIC2	1.2633E+09	1.0765E+08	9.9647E+07	1.0492E+08	1.1413E+08	1.0812E+08	1.0758E+08
AIC3	1.0553E+09	9.1384E+07	8.7074E+07	1.0318E+08	9.2897E+07	1.3170E+07	1.0563E+08
AIC1	4.9411E+11	1.3324E+11	1.3501E+11	1.4023E+11	N/A	N/A	N/A
AIC2	4.5562E+11	1.3016E+11	1.3225E+11	1.3811E+11	N/A	N/A	N/A
AIC3	3.4018E+11	1.0729E+11	1.0566E+11	1.2016E+11	N/A	N/A	N/A

Table 6.1: Area under the curve peak of radon ion.

The percentage difference between ions detected by AIC1 and AIC2 (AIC1-AIC2), and between AIC2 and AIC3 (AIC2-AIC3), and AIC1 and AIC3 (AIC1-AIC3) were calculated for 7 runs of the experiment as shown in Table 6.2 (page 77). These values showed the percent of ions adsorbed on the detector wall and on the system passage, such as the three way valve, the copper tubing and tygon tubing. From the first pass of the radon-laden air through the fiber optic detector, the amount of radon ion adsorbed from the initial flow ranged from 1.4 – 5.7%. In the second and third passes the amount of radon adsorbed to the passage

Detector		total ions	P1(ions)	P2(ions)	P3(ions)	P4(ions)	P5(ions)	P6(ions)
AIC1-AIC2 %diff.		9.7531E+09	2.0541E+09 2.35%	5.3944E+09 5.73%	1.2380E+09 1.34%	4.7185E+09 4.87%	2.1609E+09 2.01%	6.9549E+08 0.73%
AIC2-AIC3 %diff.		1.4399E+11	1.5018E+10 17.56%	8.7996E+09 9.91%	1.6849E+10 18.52%	5.4614E+09 5.93%	2.7122E+10 25.72%	5.5025E+08 0.58%
AIC1-AIC3 %diff.				2.3694E+10 25.16%	1.2228E+10 13.26%	2.2728E+10 23.46%	2.0909E+10 19.43%	1.7146E+10 17.96%
AIC2-AIC3 %diff.		9.1815E+10	2.2309E+10 19.98%	1.4133E+10 22.03%	1.4384E+10 23.20%	6.5280E+10 55.04%	1.8117E+10 27.74%	1.5801E+10 27.38%
AIC1-AIC2 %diff.		4.3185E+10	4.1881E+09 5.74%	1.2216E+09 1.68%	1.0645E+09 1.41%	1.6485E+09 2.16%	2.7346E+09 3.61%	6.9689E+09 8.73%
AIC2-AIC3 %diff.		9.1997E+10	1.0886E+10 15.82%	5.3201E+09 7.46%	1.1613E+10 15.63%	7.3076E+09 9.78%	1.1199E+10 15.36%	1.4713E+10 20.20%
AIC1-AIC3 %diff.				1.4632E+10 20.16%	9.3338E+09 12.38%	1.3665E+10 17.90%	8.2555E+09 10.91%	1.8064E+10 22.64%
AIC1-AIC2 %diff.		1.2639E+08	5.1741E+06 1.38%	8.8772E+06 2.29%	1.5106E+07 3.75%	3.4425E+06 0.87%	1.6066E+07 3.69%	N/A N/A
AIC2-AIC3 %diff.		4.7200E+08	7.2616E+07 19.69%	5.1970E+07 13.72%	5.0229E+07 12.95%	4.8237E+07 12.25%	3.5485E+07 8.47%	N/A N/A
AIC1-AIC3 %diff.				9.1283E+07 23.55%	7.6251E+07 18.92%	5.9564E+07 15.00%	8.9433E+07 20.56%	N/A N/A
AIC2-AIC3 %diff.		9.1815E+10	2.1018E+10 29.58%	2.3835E+10 8.62%	4.9983E+09 9.18%	5.3953E+09 20.86%	1.3489E+10 10.76%	7.3058E+09
AIC1-AIC2 %diff.		2.0283E+07	2.3667E+06 2.15%	3.9603E+06 3.82%	9.6373E+06 8.41%	1.3001E+07 10.23%	1.2801E+07 10.59%	2.1957E+05 0.20%
AIC2-AIC3 %diff.		2.0795E+08	1.6264E+07 15.11%	1.2573E+07 12.62%	1.7416E+06 1.66%	2.1238E+07 18.61%	9.4953E+07 87.82%	1.9504E+06 1.81%
AIC1-AIC3 %diff.				1.2223E+07 11.80%	2.7481E+07 23.99%	2.3959E+07 18.85%	2.8027E+07 23.18%	9.4629E+07 87.78%
AIC1-AIC2 %diff.		3.8492E+10	3.0881E+09 2.32%	2.7587E+09 2.04%	2.1166E+09 1.51%	N/A N/A	N/A N/A	N/A N/A
AIC2-AIC3 %diff.		1.1544E+11	2.2863E+10 17.57%	2.6592E+10 20.11%	1.7951E+10 13.00%	N/A N/A	N/A N/A	N/A N/A
AIC1-AIC3 %diff.				1.2583E+00 0.00%	1.3272E+00 0.00%	N/A N/A	N/A N/A	N/A N/A

Table 6.2: Adsorption of radon ion on the wall of the detector and passage.



Figure 6.3: Distribution of radon measured by air ion counters.

During the second and third passes, the residue of radon in the pylon was released into the fiber optic detector (AIC1-AIC3), the amount ranges from 11.8 – 29.6%. From the red peak (a2 in Figure 6.3, page 78) to the next red peak (a5) was one cycle of radon-laden air entering the air ion counter 1, and the time of 553 seconds was the time between a2 and a5.

CHAPTER 7

Discussion and Conclusions

7.1 Discussion

The basic hypothesis for the experiment is that the molecules of water attach to radon atoms and both molecules tend to stay on the surface of copper and insulators at low temperature or low airflow-rate. For the same amounts of water in the air, more radon atoms can be detected at the lower temperature and less at the higher. The maximum count of the radon atoms can be obtained at low relative humidity and this then decreases rapidly to around 16-25% of the maximum of the radon at 35% relative humidity (Figure 5.3, page 65). The adsorption of the radon in the vapor over the surface can be measured by using the air ion measuring devices (Figure 5.1, page 58).

The adsorption of water to radon is 8.4% (8.4% of total water atoms attached to the radon atoms) at relative humidity of 0-15% (Table 5.2, page 63). The adsorption of water to radon is 13.8% for the overall radon data at relative humidity of 0-60%. As the amount of water measured in terms of RH(%) increases, the degree of radon adsorption increases from 0-45% and then decreases from 45-60%. This correlates with the radon (cpm) measurement that also decreased with the higher humidity because of the adsorption of the water to radon (Figure 5.3).

An understanding of the behavior of water is required to facilitate the interpretation of the data shown in Figure 5.3. Studies of water monolayers on the surface of materials provide the base line of monolayer formation at different relative humidity.

The maximum adsorption of water onto a surface in terms of number of water monolayers was reported by Bartnikas and McMahon (1987). They stated that up to 7

water layers can be adsorbed on the surface of quartz glass and only 3 water layers on Teflon (PTFE, polytetra fluoroethylene) at a relative humidity of 100% at 23 °C. On the surface of glass the first monolayer of water formed at around RH 18%, the second layer at RH 53%, the third layer at RH 70%, the fourth layer at RH 80%, the fifth layer at RH 85%, the sixth layer at RH 92%, and the seventh layer at RH 100%. It was also confirmed (Mazer et al., 1991) that the first monolayer of water on the glass surface was at RH 18-20% or 50 µg of adsorbed water per area of the glass surface. They established an equation to calculate the number of monolayers of water adsorbed onto the glass surface at 23 °C. The amount of adsorbed water increases rapidly when the relative humidity is above 80%. The water content in air is greater at higher temperature than at lower temperature (Figure F.1, page 109), at the same relative humidity.

At the radon source (Pylon):

Humidity from the humidity flask is added before the Pylon (radon source). At RH 0% the radon disperses freely from the source into the air and exits through the filter paper, which captures the radon progeny. When the humidity increases, molecules of water start to attach randomly on the surface of the radon source in the Pylon. The beginning of the overlay is monolayer, and then bi-layer, tri-layer, and multilayer of water, which causes the radon to have more difficulty in being released from the surface of the radon source. It is analogous to the cryo-trapping phenomena (Welch, 2001). Therefore radon is trapped under the overlay of the multi layer of water molecules on the surface of the radon source at very high humidity. The graph (Figure 5.3, page 65) shows a general decrease when the relative humidity is increased.

When the RH increases to 20-50%, the water molecules are loosely bound within the water layer on the surface of the radon source. Some radon is released at RH 20% at the high temperature, but released at RH 25% at the low temperature, due to the higher mobility of radon gas at higher temperature and also more loosely binding of the water molecules.

At $RH > 50\%$ more multi-layers of water molecules overlay the surface of radon sources and also trap the radon molecules to be released, so less radon atoms exited from the Pylon as the humidity increases.

At the detector:

The water sorption hysteresis shown in Figure 1.1 (page 11) indicates the formation of a water monolayer at around RH 30%. Water can influence the surrounding molecules, e.g. the colligative effect of dissolved molecules through dipole-dipole forces, ionic bonds, hydrogen bonds; the capillary effect of water in changing of hydrogen bonds in the water; the surface interaction effect of undissolved molecules through dipole-dipole forces, ionic bonds (H_3O^+ or OH^-), van der Waal forces, and hydrogen bonds. Water activity (a_w) is shown (Figure 1.1) in fraction of water per water saturated in air. So the equilibrium relative humidity in (%) is $100(a_w)$.

Figure 5.3 (page 65) shows the influence of water molecules on radon atoms, over the glass surface of the detector as a function of relative humidity (RH) and temperature. Interactions between water molecules and radon atoms are a combination of the displacement of radon by water, which removes radon atoms, and the overlay of water molecules on the radon, which traps radon atoms.

Three ranges of RH will be considered in turn:

1) RH 0-20%: At low humidity, the attached fraction of radon has a very high tendency to attach on the surface due to its smaller dimension in comparison to the unattached fraction of radon. The attached fraction is considered as the 'naked' radon atom (when no water is present). So at the lowest relative humidity, or 0%, the graph of radon (cpm) shows the highest peak due to no influence of water over radon. When the humidity is increased, the water activity (a_w) is increased as shown in Figure 1.1 (page 11). Also the water molecules start to form a strongly bound monolayer on the surface and wall of the detector. At RH 0% naked Rn, as attached fraction, was on the metal surface of the detector because of radon's sticking property. Also there was only dry air in the detector. The dry air, which was more dense than water vapor, has density of 1.292 g/cm^3 (0°C) and 1.165 g/cm^3 (30°C) (Wikipedia, 2007). So it was more difficult for the Rn molecules to escape from the surface of the detector. At the same humidity there are more radon atoms releasing from the radon sources at higher temperature than at lower temperature. The water molecules tend to form a layer on the surface and the radon atoms are gradually replaced by water. The further influence of water's hydrogen bond strength can be shown in changes of its physical properties (e.g., viscosity, density, compressibility, surface tension), and in forms of osmotic and atoms arrangement, which affects the radon (e.g., mono-layer, bi-layer and multi-layers, solvent phase). Some of the attached fractions of radon are displaced by molecules of water so the activity is decreased.

2) RH 20-50%: On the glass surface the accumulation of the water layer increases more rapidly as some areas bi-layers of water are formed (Bartnikas and McMahon, 1987). The higher the relative humidity at this interval, the less strongly bound are water

layers and capillary adsorbed water. The radon atoms increasingly reattach to the surface between the loosely bound water layers, so the measured activity increases between RH 20-50%. More water molecules are easily displaced by radon atoms sooner, especially at higher temperature. The water is more loosely bound at the higher temperature than at the lower temperature. Radon shows more displacement and less overlay by the water molecules at high temperature, and conversely at low temperature. So the peak is more pronounced in the low temperature than in the high temperature.

3) RH > 50%: The radon with their attached water molecules get larger at very high humidity (Porstendorfer and Mercer, 1978). When the relative humidity is increased above 50%, the radon is again displaced by the water in the form of solvent. Therefore the radon activity is decreased. The closer the relative humidity comes to 100%, the greater is the size of the average radon on the detector surface, while the molecules of water turn into solvent (liquid). The activity is increased but less than the reading at the relative humidity of 20-50% because the radon atom attached to water, with its larger size, occupies a larger surface area with fewer radon atoms, or fewer radon atoms would fit on a given area of the surface.

At high temperature the radon tends to have more mobility and much larger size to occupy the area of surface with much fewer radon atoms. So the reading of cpm is much less on the surface when compared with low temperature. The graph (Figure 5.3) of activity shows decreases and therefore less radon. At low temperature the radon tends to have less mobility, and large size relative to the size at lower humidity. The graph shows decreases because of less radon atoms attached on the surface.

The use of the three air ion measuring units (located at the entrance of the radon, the exit of the radon source (or the entrance of the ionizing detector), and the last one at the exit of the ionizing detector) actually confirmed that radon ions adsorb and attach to the surface of the detector compartment and the bundle of fiber optics, as shown in Table 6.2 (page 77). The ions/sec measured by air ions detector and the radon in cpm measured by the fiber optic detector, shown in Figure 5.4 (page 66), have similar changes in distribution over time due to the radon/water interaction within the closed loop system. The mechanism of the radon/water interaction, in terms of displacement and overlay by the water molecules on the surface (as described above), is the same in both type of detectors. It is also supported by the mathematical model (Table 5.2, page 63) for RH 0-60%.

There is a significant correlation between the experimental data (Figure 5.3, page 65) and the mathematical model $[Z = a + b \cdot \ln(\text{RH}\%) + c \cdot \text{Temp}]$ both showing the influence of temperature and humidity (water in the air) with a pronounced rising peak at RH 25-45%.

The amount of radon atoms adsorbed onto the surface of the fiber optic are about 1.4 - 5.7% at 1st pass, about 1.7 - 5.7% at the 2nd pass, about 1.3 - 8.4% at the 3rd pass, about 1.0 - 10.2% at the 4th pass, and about 2.0 - 10.6% at the 5th pass of the radon-laden air within the closed loop (see Table 6.2, page 77). These data were obtained by the air ions counter at the entry and the exit of the fiber optic detector. Also the amount of radon atoms adsorbed onto the tubing wall between air ion counter 2 (at H in Figure 5.1) and air ion counter 3 (at U in Figure 5.1) are about 15.1 - 20% at the 1st pass, about 7.5 - 29.6% at the 2nd pass, about 13 - 23.2% at the 3rd pass, about 5.9 - 18.6% at the 4th pass, and about 8.5 - 25.7% at the 5th pass. Therefore the radon-laden air measured at the

beginning of the experiment showed a high or maximum peak (Figure 5.5, page 67) and then the amplitude of the peaks decreased due to the adsorption of radon atoms to the surface of tubing and detector. At about 2000 minutes the graph reached the saturation region at which the adsorption is saturated and the equilibrium of the system is reached.

Maintaining a constant temperature over the duration of an individual experiment, about one week, was highly challenging. A system of heating and cooling controls was set up, but with the constantly changing external room temperature, which was beyond control, it was not possible to achieve perfect isothermal conditions. Another challenge was maintaining a constant flow rate due to the unpredictable nature of the tygon tubing, which stretched when being used in the peristaltic pump.

7.2 Conclusions

- It is proved beyond doubt that relative humidity (RH) has an influence over radon detection in both types of radon detector studied here. The mathematical model and the experimental data show that highest activity of radon occurs at RH 0%. When the RH increases, radon is inhibited from access to the detector surfaces.
- Water molecules start to overlay and loosely bind at RH 30-80%, so more radon can attach to the surface of the detector to replace the water molecules.
- Radon attaches to the walls of the tubing and the surface of the detector. Radon also attaches to the water molecules, therefore the detection is much less than it would be otherwise.
- Using air ion counters the amounts of radon attached on the walls of the tubing can be measured. Air ion counters can also measure additional build up. After the radon-laden

air completes each circulation, it passes by the radon source and exits with an additional amount of build up, accumulated since the previous exit.

- For future research, one recommendation would be for improved room temperature regulation. The room temperature should be controllable to eliminate large temperature fluctuation, which would facilitate better temperature control of the experimental system.
- For future research, other recommendations for the materials would be; to shorten the length of the tubing, so that the steady state can be reached sooner than 2000 minutes, this would enable each experiment to be conducted in less time. To use plastic three-way valves instead of copper to eliminate the large amount of adsorption on the copper metal. Also to use a smaller size three-way valve to minimize the surface area. A new material or new type of peristaltic pump should be used to prevent or avoid the stretching of the tubing.

Appendix A

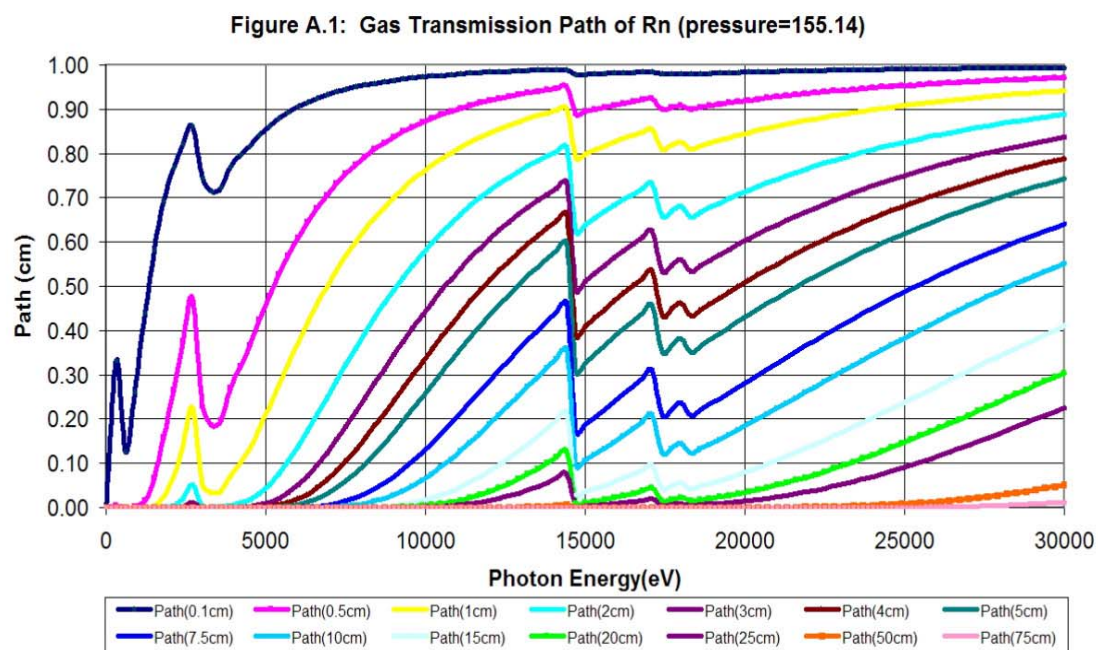
Basic Information of Radon

Name	Radon
Symbol	${}_{86}\text{Rn}^{222}$
CAS registry number	10043-92-2, 14859-67-7 for Rn in water as solvent
Physical state (at 20°C, 1atm)	Gas (the densest known gas)
General Information	Colourless gas at ordinary temperature, but when cooled below freezing point it exhibits a brilliant phosphorescence which becomes yellow as the temperature is lowered and orange at the temperature of liquid air.
Atomic number	86
Atomic mass	222.018
Atomic weight	222.0 amu (222 g/mol)
Atomic number-to-mass(Z/A)	0.38736
Atomic radius	1.34 Å
Atomic volume	50.5 cm ³ /mol
Molar volume	50.5 cm ³ /mol
Mean excitation energy	794.0 eV
Melting Point	-71.15 °C (202.15 °K, -95.8 °C)
Boiling Point	-61.85 °C (211.35 °K, -79.24 °F)
Critical Point	377°K at 6.28MPa
Covalent radius	145 pm
Heat of vaporization	16.4-18.1 kJ/mol.
Heat of fusion	2.89- 3.247 kJ/mol.
Specific heat capacity	94 J/(kg.°K)
Enthalpy of Fusion	2.7 kJ/mol
Enthalpy of Vaporisation	18.1 kJ/mol
Heat capacity	20.786 J/(mol.°K) at 25°C
Thermal entropy, S°	176.1 J/(mol.°K) at 298.15°K (omitted nuclear spin and isotope mixing effects)
Thermal conductivity	0.00364 W/(m.°K), 3.61mW/(m.°K) at 300°K,
Estimated Crustal Abundance	4x10 ⁻¹³ mg/kg
Estimated Oceanic Abundance	6x10 ⁻¹⁶ mg/liter
Physical half-life	3.824 days
Mean lifetime	5.5 days
Vapor Pressure	1Pa at 110°K, 10Pa at 121°K, 100Pa at 134°K, 1kPa at 152°K, 10kPa at 176°K, 100kPa at 211°K
1st ionization energy/potential	1 st (M-M ⁺): 1037 kJ/mol.

Electronegativity	no data (Pauling scale)
Electron Affinity (M-M)	+41 kJ/mol
Electrical conductivity	0.1 mOhm-cm
Polarizability	5.3 \AA^3 ($5.3 \times 10^{-24} \text{ cm}^3$)
Number of protons/electrons	86
Number of neutrons	136
Ionization energy	10.745 eV
Production rate	0.001 cm^3/day per g of Ra^{226} 0.64 cm^3/month per g of Ra^{226}
Classification	Gas in Noble Gas [max.electrons of outer shell 2(Helium) or 8] Gas (nonmagnetic)
Crystal structure	Cubic face centered
Cross section σ_a	0.72 barns (Thermal Neutron Capture)
Oxidation states	Rn^0 , Rn^{+2}
Density	0.00973 g/cm^3 at 293°K(9.73 g/L at 0°C,101.325kPa)
Color	Colorless
Atomic radius (calc.)	120pm
Covalent radius	145pm
Atomic structure	Number of energy levels= 6 1 st Energy level= 2 2 nd Energy level= 8 3 rd Energy level= 18 4 th Energy level= 32 5 th Energy level= 18 6 th Energy level= 8
Electron configuration	$1s^2, 2s^2 2p^6, 3s^2 3p^6 3d^{10}, 4s^2 4p^6 4d^{10} 4f^{14}, 5s^2 5p^6 5d^{10}, 6s^2 6p^6$
Electron per shell	2, 8, 18, 32, 18, 8
Group, period, block	18(VIIIA), 6, p
Dissolve with water	about 230 cm^3/kg at 20°C
Reaction with	only fluorine in halogens to form the difluoride radon(II) fluoride, RnF_2
X-ray mass attenuation coefficients	(see graph)
Electron Level Widths	L3 6.41 eV L2 7.20 eV L1 13.10 eV K 73.30 eV
Electron binding energies	98404 eV, (1s of shell K) orbital 18049 eV, (2s of shell L _I) orbital 17337.1 eV, (2p _{1/2} of shell L _{II}) orbital 14619 eV, (2p _{3/2} of shell L _{III}) orbital 4482 eV, (3s of shell M _I) orbital

4159 eV, ($3p_{1/2}$ of shell M_{II}) orbital
 3538 eV, ($3p_{3/2}$ of shell M_{III}) orbital
 3021.5 eV, ($3d_{3/2}$ of shell M_{IV}) orbital
 2892.4 eV, ($3d_{5/2}$ of shell M_V) orbital
 1097 eV, (4s of shell N_I) orbital
 929 eV, ($4p_{1/2}$ of shell N_{II}) orbital
 768 eV, ($4p_{3/2}$ of shell N_{III}) orbital
 567 eV, ($4d_{3/2}$ of shell N_{IV}) orbital
 541 eV, ($4d_{5/2}$ of shell N_V) orbital
 238 eV, ($4f_{5/2}$ of shell N_{VI}) orbital
 238 eV, ($4f_{7/2}$ of shell N_{VII}) orbital
 214 eV, (5s of shell O_I) orbital
 164 eV, ($5p_{1/2}$ of shell O_{II}) orbital
 127 eV, ($5p_{3/2}$ of shell O_{III}) orbital
 48 eV, ($5d_{3/2}$ of shell O_{IV}) orbital
 48 eV, ($5d_{5/2}$ of shell O_V) orbital
 26 eV, (6s of shell P_I) orbital

Isotopes	Isotope	half life
	Rn^{211}	14.6 hours
	Rn^{212}	24.0 minutes
	Rn^{217}	0.6 milliseconds
	Rn^{218}	35.0 milliseconds
	Rn^{219} actinon (derived from Actinium)	3.96 seconds
	Rn^{220} thoron (decay of Thorium)	55.61 seconds
	Rn^{222}	3.824 days
Date of discovery	1898	
Discoverer	Fredrich Ernst Dorn	
Name origin	1900 called radium emanation (from Radium) 1908 called niton by William Ramsay and Robert Whytlaw-Gray (Latin “nitens” meaning “shining”, symbol Nt) 1923 called Radon	
Result from	decay of Radium Ra^{226}	
Particle emitted	alpha	
Daughter product	Polonium Po^{218}	



(National Institute of Standards and Technology (NIST), Physics Laboratory, 2007)

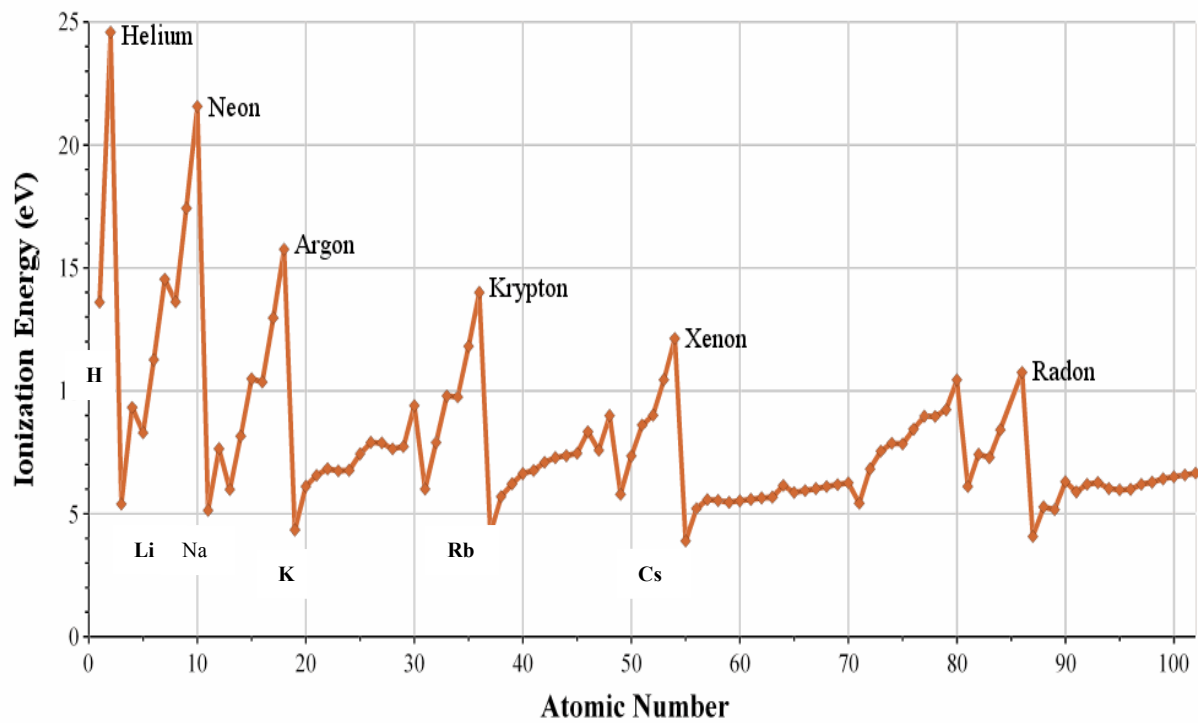


Figure A.2: Ionization energy (eV) of the outer electron in various elements (Wikipedia, 2007)

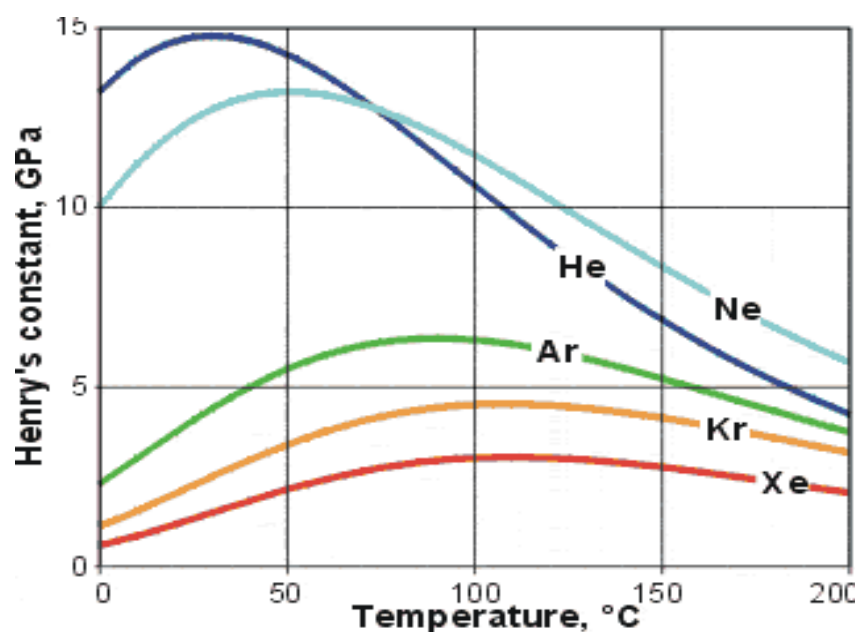


Figure A.3 : Henry's constant of Inert gases vs Temperature °C

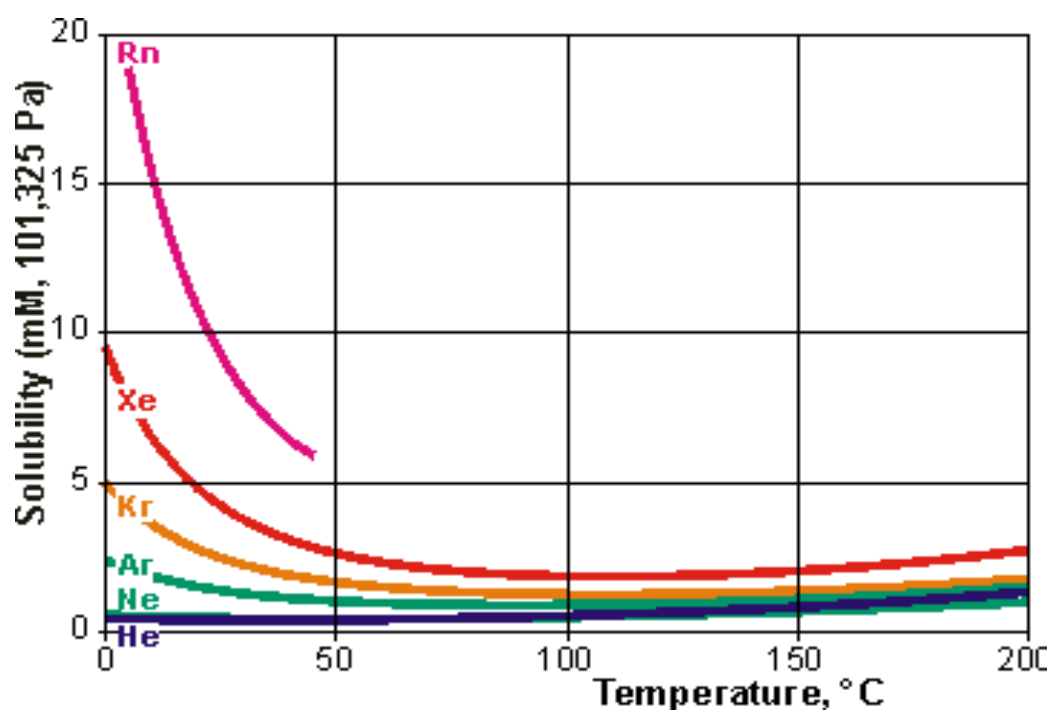


Figure A.4: Solubility of Inert gases vs Temperature °C

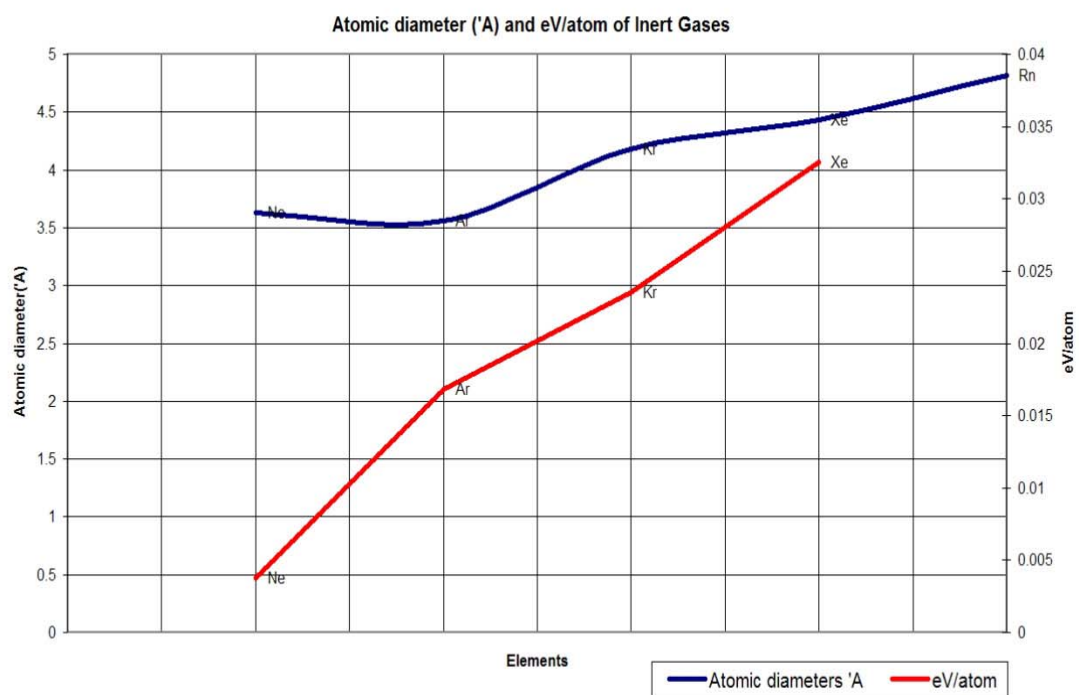


Figure A5: Atomic diameter and eV of Inert gases

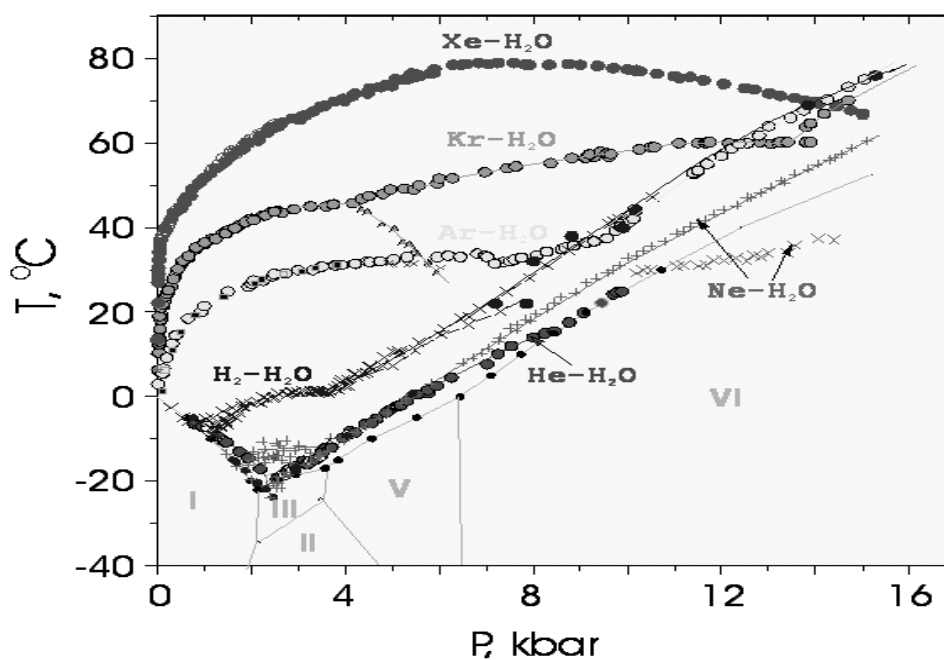


Figure A.6: Decomposition of hydrate forming in Inert gas-water system (Manakov, A Yu, 2000)

Appendix B

The Diffusive Transport

The diffusive transport is an important phenomenon for all states and substances. Fick's law is used to describe the random motion of molecules; such as in the form of: molecular diffusion or turbulence in fluids; turbulent diffusion (eddies current) in fluids; random disperse in gases; and diffusivity in air/gases.

Gaseous pollutants in soils gradually move through air passages between soil grains (in the small scaled randomly as Brownian motions of molecules). The down-gradient motions and large scaled motions are calculated by Fick's law. The diffusive flux (J_x) is directly proportional to the concentration gradient ($\frac{\Delta C}{\Delta x}$). The Fick's 1st law can be derived as,

$$N_x = A D \frac{\Delta C}{\Delta x}$$

$$J_x = D \frac{\partial C}{\partial x}$$

$$N_x = \text{mass flux } [(\text{mass})(\text{time})^{-1}]$$

$$A = \text{area of plane of diffusion } [(\text{m})^2]$$

$$D = \text{diffusion coefficient (molecular or turbulent)} [(\text{m})^2 (\text{min})^{-1}]$$

$$\Delta C = \text{concentration difference } [(\text{mg})(\text{m})^{-3}]$$

$$\Delta x = \text{distance or length over which concentration difference migrates}$$

$$\frac{\Delta C}{\Delta x} = \text{concentration gradient}$$

$$J_x = \text{diffusive flux or mass flux per area } [(\text{mass})(\text{m})^{-2}(\text{time})^{-1}]$$

The diffusivity is highly temperature-dependent and it can be shown its relation in term of the atomic jump frequency.

$$\frac{D}{D_0} = e^{-\frac{Q}{KT}}$$

D_0 = the frequency factor

Q = activation energy which is equivalent to enthalpy (ΔH) of atom migration

K = the Boltzmann constant

T = the absolute temperature

$$\frac{\partial C}{\partial t} = \frac{\partial}{\partial x} \left[D \frac{\partial C}{\partial x} \right] = D \frac{\partial^2 C}{\partial x^2}$$

The change in concentration between two points is the differences of $|J_a| > |J_b|$ which will show a net flow of the mass through the point. At the point there is a change in the concentration as a result of intrinsic diffusion, due to the Kirkendall flow of the mass passing the points. The net effect, which is a weighted average of the two intrinsic diffusion coefficients, is the inter-diffusion coefficient (\bar{D}). The inter-diffusion coefficient is the value measured in most experiments (Bhadeshia H K D H, 2007).

$$\bar{D} = X_b D_a + X_a D_b$$

where

X_a, X_b = mole fraction of the matter a and b

D_a, D_b = intrinsic diffusion coefficient of the matter a and b

The solution to Fick's 2nd law can be shown in 4 groups of processes (Green A, Humphreys J and Mackenzie R et al, 2000):

1. Carburization process:

solution is $C = C_s - (C_s - C_0) \operatorname{erf}\left(\frac{x}{2\sqrt{Dt}}\right)$

C_s = surface concentration

C_0 = initial bulk concentration

2. De-carburization process:

solution is $C = C_0 \operatorname{erf}\left(\frac{x}{2\sqrt{Dt}}\right)$

C_0 = initial bulk concentration

3. Diffusion couple process:

solution is $C = \left[\frac{C_1 + C_2}{2}\right] - \left[\frac{C_1 - C_2}{2}\right] \operatorname{erf}\left(\frac{x}{2\sqrt{Dt}}\right)$

C_1 = concentration of material 1

C_2 = concentration of material 2

4. Homogenization process:

solution is $C = C_{\text{mean}} + \beta_0 \sin\left(\frac{\pi x}{\lambda}\right) e^{-\frac{t}{\tau}}$

C_{mean} = mean concentration

β_0 = initial concentration amplitude

τ = half-wavelength of cells

t = relaxation time

λ = distance per each jump

z	erf(z)	z	erf(z)	z	erfc(z)	z	erfc(z)
0	0	0.85	0.7707	0	1	0.85	0.2293
0.025	0.0282	0.9	0.797	0.025	0.968	0.9	0.2031
0.05	0.0564	0.95	0.8209	0.05	0.9436	0.95	0.1791
0.1	0.1125	1	0.8427	0.1	0.8875	1	0.1573
0.15	0.168	1.1	0.8802	0.15	0.8320	1.1	0.1198
0.2	0.2227	1.2	0.9103	0.2	0.7773	1.2	0.0897
0.25	0.2763	1.3	0.934	0.25	0.7237	1.3	0.06599
0.3	0.3286	1.4	0.9523	0.3	0.6714	1.4	0.04771
0.35	0.3794	1.5	0.9661	0.35	0.6206	1.5	0.03389
0.4	0.4284	1.6	0.9763	0.4	0.5716	1.6	0.02365
0.45	0.4755	1.7	0.9838	0.45	0.5245	1.7	0.01621
0.5	0.5205	1.8	0.9891	0.5	0.4795	1.8	0.01091
0.55	0.5633	1.9	0.9928	0.55	0.4367	1.9	0.00721
0.6	0.6039	2	0.9953	0.6	0.3961	2	0.00468
0.65	0.642	2.2	0.9981	0.65	0.3580	2.2	0.00186
0.7	0.6678	2.4	0.9993	0.7	0.3222	2.4	0.00069
0.75	0.7111	2.6	0.9998	0.75	0.2888	2.6	0.00024
0.8	0.7421	2.8	0.9999	0.8	0.2579	2.8	0.000075

Table B.1: Gaussian Error function erf(z) and Complimentary error function erfc(z)

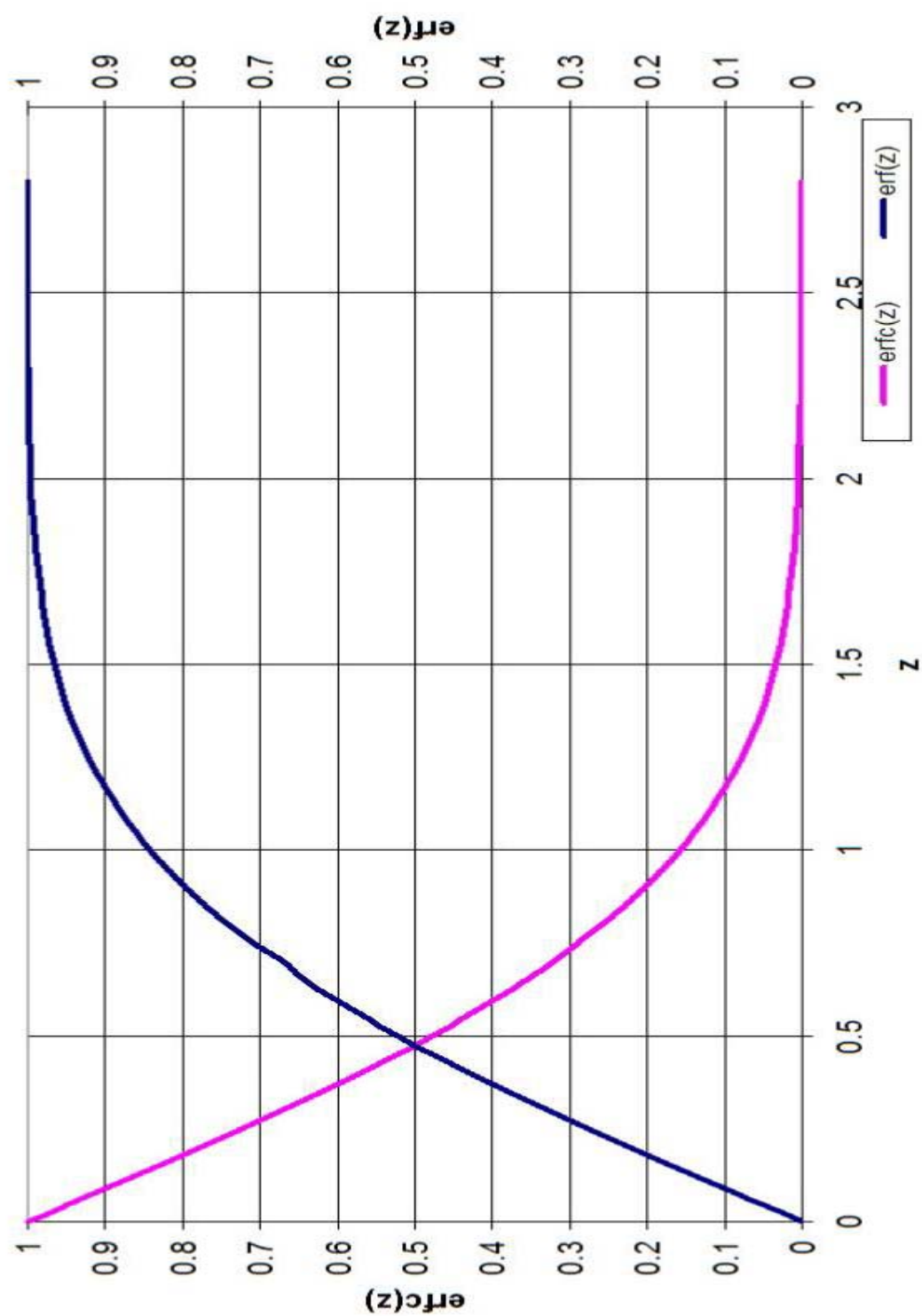


Figure B.1: Gaussian error function $\text{erf}(z)$ and Complimentary error function $\text{erfc}(z)$

Appendix C

Scattering angle and impact parameter (b) of alpha particle (5.489MeV)

Scattering angle(θ)	impact parameter(b) in meters	b(fermi)	Scattered fraction
5	5.17E-13	516.7429	3.22E-10
10	2.58E-13	257.8789	8.01E-11
15	1.71E-13	171.3715	3.54E-11
20	1.28E-13	127.9525	1.97E-11
25	1.02E-13	101.7682	1.25E-11
30	8.42E-14	84.20061	8.54E-12
35	7.16E-14	71.55589	6.17E-12
40	6.20E-14	61.98717	4.63E-12
45	5.45E-14	54.46824	3.57E-12
50	4.84E-14	48.38326	2.82E-12
55	4.33E-14	43.34021	2.26E-12
60	3.91E-14	39.07764	1.84E-12
65	3.54E-14	35.41444	1.51E-12
70	3.22E-14	32.22114	1.25E-12
75	2.94E-14	29.4027	1.04E-12
80	2.69E-14	26.88773	8.71E-13
85	2.46E-14	24.62154	7.30E-13
90	2.26E-14	22.56148	6.13E-13
95	2.07E-14	20.67379	5.15E-13
97	2.00E-14	19.96071	4.80E-13
98	1.91E-14	19.6124	4.64E-13
99	1.93E-14	19.26932	4.47E-13
100	1.89E-14	18.93133	4.32E-13
105	1.73E-14	17.31203	3.61E-13
110	1.58E-14	15.79772	3.01E-13
115	1.44E-14	14.37325	2.49E-13
120	1.30E-14	13.02588	2.04E-13
125	1.17E-14	11.74476	1.66E-13
130	1.05E-14	10.52059	1.33E-13
135	9.35E-15	9.345273	1.05E-13
140	8.21E-15	8.211709	8.13E-14
145	7.11E-15	7.113609	6.10E-14
150	6.05E-15	6.045332	4.40E-14
155	5.00E-15	5.001761	3.01E-14
160	3.98E-15	3.978198	1.91E-14
165	2.97E-15	2.970276	1.06E-14
170	1.97E-15	1.973874	4.69E-15
175	9.85E-16	0.985055	1.17E-15
180	0	0	n/a

The alpha 5.489MeV scattering off a nucleus of atomic number $z=86$

Table C.1: Scattering angle of alpha particle (5.489MeV), (Hyperphysics. 2007)

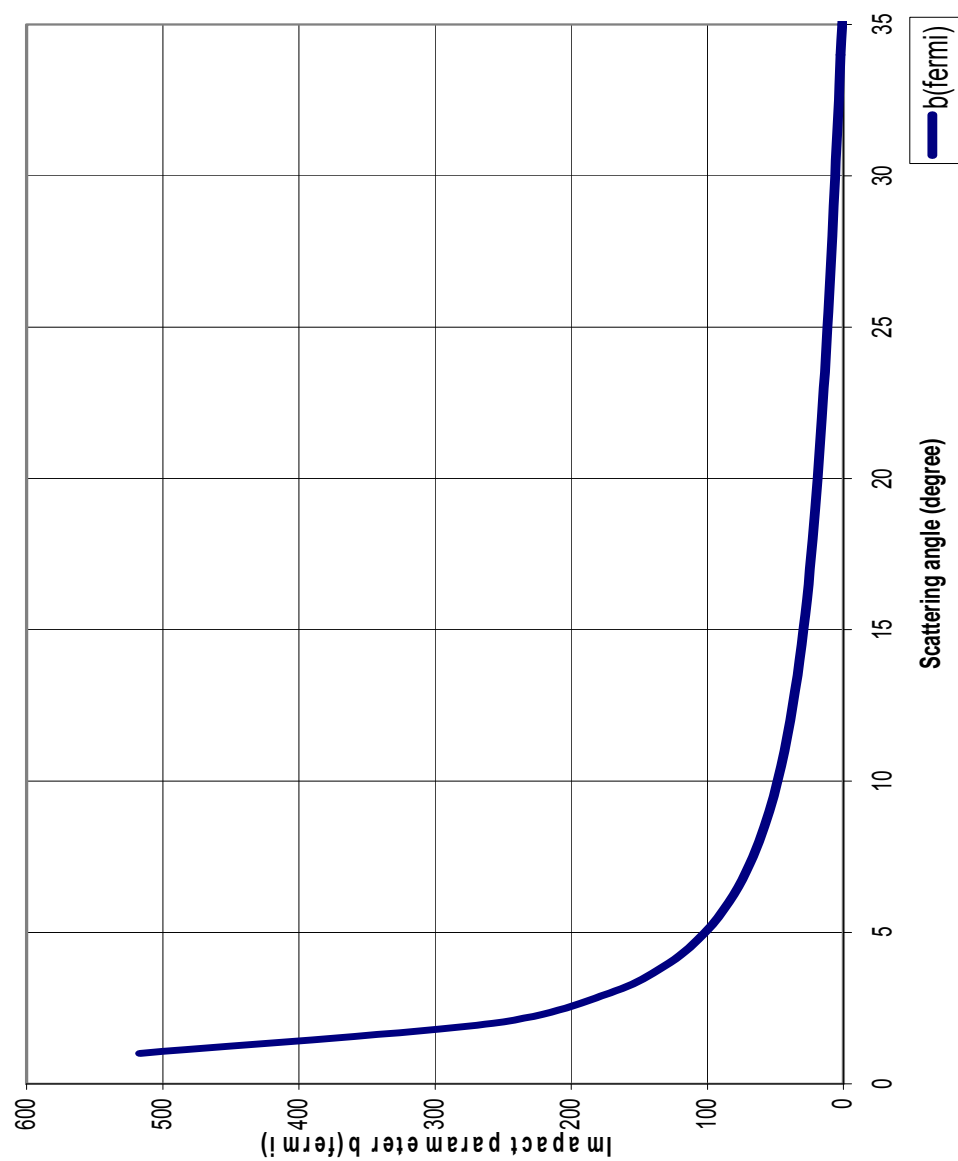


Figure C.1: Alpha Scattering Impact Parameter as a function of Scattering Angle.

Appendix D

Van der Waal force by Lennard-Jones 6-12 potential for small non-polar molecules

The total potential energy of interactions in any system can be derived in the general form for the intermolecular interactions by using the pair-wise additivity approximation (PWAA) (Combs L L, 2008). The potential energy well of all possible interactions and perturbations of interactions by others, is the combination of all pair interactions in forms of attraction and repulsive forces. The total potential energy (V) is the sum of potentials from all pair interactions, which are charge-charge interaction $[\frac{-q_1 q_2}{r}]$, charge-dipole interaction $[\frac{-q^2 \mu^2}{3kTr^4}]$, dipole-dipole interaction $[\frac{2\mu_1^2 \mu_2^2}{3kTr^6}]$, induced dipole-charge interaction $[\frac{-q^2 \alpha}{r^6}]$, induced dipole-dipole interaction $[\frac{\alpha \mu^2}{r^6}]$ or London dispersion, induced dipole-induced dipole interaction $[\frac{3h\nu_0(\alpha_1 \alpha_2)}{4r^6}]$, and van der Waals repulsion.

$$V_{\text{total}} = \sum V_{ij}(r)$$

$$\begin{aligned} V_{\text{total}} &= [\frac{-q_1 q_2}{r}] + [\frac{-q^2 \mu^2}{3kTr^4}] + [\frac{2\mu_1^2 \mu_2^2}{3kTr^6}] + [\frac{-q^2 \alpha}{r^6}] + [\frac{\alpha \mu^2}{r^6}] + [\frac{3h\nu_0(\alpha_1 \alpha_2)}{4r^6}] \\ &= [\frac{-q_1 q_2}{r}] + [\frac{-q^2 \mu^2}{3kTr^4}] + [\frac{2\mu_1^2 \mu_2^2}{3kTr^6}] + [\frac{-q^2 \alpha}{r^6}] + [\frac{\alpha \mu^2}{r^6}] + [\frac{3I(\alpha_1 \alpha_2)}{4r^6}] \end{aligned}$$

If $q=0$ as the van der Waals force occurs over the non polar molecule (or no charge):

$$V_{\text{total}}(q=0) = [\frac{A}{r^{12}}] - [\frac{B}{r^6}]$$

$$\text{and } B = [-\frac{2\mu_1^2 \mu_2^2}{3kTr^6}] + [\frac{\alpha \mu^2}{r^6}] + [\frac{3h\nu_0(\alpha_1 \alpha_2)}{4r^6}] = 4\epsilon\sigma^6$$

$$A = 4\epsilon\sigma^{12}$$

$$\text{Then } V_{\text{total}} = 4\epsilon \left[\left(\frac{\sigma}{r} \right)^{12} - \left(\frac{\sigma}{r} \right)^6 \right]$$

The computerized V_{total} is truncated at the cut-off distance of 2.5σ , where $V_{\text{total}} = -0.0163\epsilon$.

The minimum potential energy can be obtained at the distance $r = 2^{\frac{1}{6}} \sigma$.

which is known as the Lennard-Jones 6-12 potential for small non-polar molecules.

Therefore the force gradient function can be derived from the negative of the gradient of the total potential:

$$F(r) = -\nabla [V(r)] = \frac{d}{dr} (V(r)) \tilde{r} = 4\epsilon \left[12 \left(\frac{\sigma^{12}}{r^{13}} \right) - 6 \left(\frac{\sigma^6}{r^7} \right) \right] \tilde{r}$$

$$\text{or } F(r) = -\left(\frac{4\epsilon}{r} \right) \left[6 \left(\frac{\sigma}{r} \right)^6 - 12 \left(\frac{\sigma}{r} \right)^{12} \right]$$

and the maximum force $(F_{\text{max}}) = -2.3964 \left(\frac{\epsilon}{\sigma} \right)$, at $r = 1.2445 \sigma$, where

q, q_1, q_2 = charges in coulombs

μ, μ_1, μ_2 = dipole moment in Debye

$\alpha, \alpha_1, \alpha_2$ = molar polarizability in angstroms/molecule

k = the Boltzman constant

r = the distance between interacting particles

or the distance between the particle and the center of the dipole in Angstroms

T = the temperature

I = the ionizing potential

ν_0 = the fundamental vibrational frequency of the molecules

(no vibrational mode for an atom)

h = the planck's constant

h_0 = the energy of the first vibrational energy mode of the molecule.

σ = finite distance at which interparticle potential is zero $= \left(\frac{A}{B}\right)^{\frac{1}{6}}$

ε = the depth of potential well $= \frac{B^2}{4A}$

Generally there is less variation of vibrational energy among molecules, but this does not cause the variation in the polarizability. Thus most of the variation in the dispersion interaction arises from the polarizability differences.

The intermolecular potential energy (V) as dipole-dipole interaction for water- water

molecules is inversely proportional to $\left[\frac{3}{2kTr^6}\right]$, or $V = \frac{-2(1.85)^2}{(3kTr^6)}$, where k is the

Boltzman constant, T is temperature, and r is the distance between interacting particles or the distance between the particle and the center of the dipole (Combs L L, 2008).

The generalized Potential Energy functions can be derived as V_{total} and it is the combination of repulsive potential ($V_{\text{repulsive}}$) and attractive potential ($V_{\text{attractive}}$).

$$V_{\text{total}} = V_{\text{repulsive}} + V_{\text{attractive}} = \frac{A}{r^n} + \frac{B}{r^m}$$

where $n > m$ (attraction potential at large distance until close to zero)

if $V_{\text{total}} = 0$, then $\sigma = r$, where $\frac{A}{r^n} = \frac{B}{r^m}$ and $B = A \sigma^{(m-n)}$

if $V_{\text{total}} = V_{\text{minimum}}$, where $r(v=v_{\text{min}})$ is $r_{v_{\text{min}}}$ or r^* ,

and also ε = depth of the potential well in negative value ($-V$) or $V_{r=r^*} = -\varepsilon$

$$V_{\text{total}} = \frac{A}{r^n} + \frac{B}{r^m} = \frac{A}{r^n} - \frac{A\sigma^{(m-n)}}{r^m}$$

$$\sigma^n V_{\text{total}} = A \left[\left(\frac{\sigma}{r} \right)^n - \left(\frac{\sigma}{r} \right)^m \right]$$

To find V_{minimum} , taking derivative of first order;

$$\sigma^n \frac{dV}{dr} = A \left[n \left(\frac{\sigma}{r} \right)^{n-1} \left(-\frac{\sigma}{r^2} \right) - m \left(\frac{\sigma}{r} \right)^{m-1} \left(-\frac{\sigma}{r^2} \right) \right] = 0$$

so
$$n \left(\frac{\sigma}{r^*} \right)^n = m \left(\frac{\sigma}{r^*} \right)^m$$

$$\left(\frac{\sigma}{r^*} \right)^{n-m} = \frac{m}{n}$$

$$\left(\frac{\sigma}{r^*} \right) = \left(\frac{m}{n} \right)^{\frac{1}{(n-m)}}$$

$$\sigma = \left\{ \left(\frac{m}{n} \right)^{\frac{1}{(n-m)}} \right\} r^*$$

from
$$\sigma^n V_{\text{total}} = A \left[\left(\frac{\sigma}{r} \right)^n - \left(\frac{\sigma}{r} \right)^m \right]$$

$$\sigma^n (-\varepsilon) = A \left[\left(\frac{m}{n} \right)^{\frac{n}{(n-m)}} - \left(\frac{m}{n} \right)^{\frac{m}{(n-m)}} \right]$$

then A and B can be derived as;

$$A = \frac{\varepsilon \sigma^n}{(n-m)} \left(\frac{n}{m} \right)^{\frac{1}{(n-m)}}$$

and
$$B = \frac{\varepsilon \sigma^m}{(n-m)} \left(\frac{n}{m} \right)^{\frac{1}{(n-m)}}$$

$$V = \varepsilon \left[\frac{\left(\frac{n}{m} \right)^{\frac{1}{(n-m)}}}{n-m} \right] \left[\left(\frac{\sigma}{r} \right)^n - \left(\frac{\sigma}{r} \right)^m \right]$$

For Lennard-Jones 6-12 potential equation, $V_{\text{total}} = 4\epsilon \left[\left(\frac{\sigma}{r} \right)^{12} - \left(\frac{\sigma}{r} \right)^6 \right]$

and $F(r) = -\left(\frac{4\epsilon}{r} \right) \left[6 \left(\frac{\sigma}{r} \right)^6 - 12 \left(\frac{\sigma}{r} \right)^{12} \right]$

Therefore the maximum attraction of van der Waal force, $F_{\text{max}} = -2.3964 \frac{\epsilon}{\sigma}$, at $r = 1.2445$

Appendix E

Properties of inert gases and water.

Elements	H ₂ O	He	Ne	Ar	Kr	Xe	Rn
Ionization potential (kJ/mole) 10 ³	[0.0889 3]	2.371	2.079,2.0 85	1.519,1.5 24	1.350	1.170,1. 173	1.034
Electronegativity κ		4.53	3.08	2.91	2.58	2.24	1.98
Dissociation pressure 10 ⁻⁴ Pa	—	—	—	9.66 x10 ⁻²	1.42 x10 ⁻²	1.13 x10 ⁻²	3.92 x10 ⁻⁴
Dissociation energy of (M)F ₄ Halides (kJ/mole)	—	—	-452.0	46.1	78.7	208.0	—
Heat of Formation of (M)F ₄ Halides (kJ/mole)	—	—	2123	225	-2	-515	-360
Bond Ionicity of (M)F ₄ Halides (%)	—	—	33	53	47	58	—
Electronic polarizability, α , cm x10 ²⁵ (or nm ³ x10 ⁻³)	—	—	3.9 (0.39)	16.3 (1.63)	24.6 (2.46)	40.0 (4.0)	54.2 (5.42)
Polarizability, 10 ⁸ cm or °A ³ /molecule	1.44- 1.48	—	1.6	1.82	1.98	2.13	2.2
Permanent Dipole moment (Debye, D, or 10 ⁻¹⁸ esu.cm)	1.85-2.6	0	0	0	0	0	0
Van der Waal constant, a (bar L ² /mol ²)	5.537	0.034	0.208	1.355	2.325	4.192	6.601
Van der Waal constant, b(L/mol)	0.0304	0.023	0.0167	0.03201	0.0396	0.0515	0.0623
Van der Waals Surface Area, A _{ws} 10 ⁻²⁰ m ²	N/A	24.6	29.8	44.4	51.3	58.6	74.8
Solvent Accessible Surface Area A _{sas} 10 ⁻²⁰ m ²	N/A	98.5	108.6	135.2	147.0	159.3	185.3
Solvent-Excluding Surface Area A _{ses} 10 ⁻²⁰ m ²	N/A	24.6	29.8	44.4	51.3	58.6	74.8
Number of water molecules in the first Solvation shell, N molecules of water	N/A	12.6	13.9	17.2	18.7	20.3	23.6
Volumes of space enclosed by Van der Waals Surface, V _{ws} 10 ⁻³⁰ m ²	N/A	11.5	15.3	27.8	34.5	42.2	60.9
Volumes of space enclosed by Solvent Accessible Surface, V _{sas} 10 ⁻³⁰ m ²	N/A	92.0	106.4	147.8	167.6	180.0	237.2
Volumes of space enclosed by Solvent-Excluding Surface, V _{ses} 10 ⁻³⁰ m ²	N/A	11.5	15.3	27.8	34.5	42.2	60.9

Elements	H2O	He	Ne	Ar	Kr	Xe	Rn
Atomic radius, angstrom		1.08	1.21	1.64	1.78	1.96	2.11
Individual gas constant, R, J/Kg °K (Universal gas constant(R_u)=R.MW p (286.9 DryAir)	461.5Va	2,077	412.015	208.174	99.218	63.329	37.453
Molecular weight, MW(kg/kmole) Vap (28.97 DryAir)	18.02	4.003	20.18	39.94	83.80	131.29	222.0
Solubility in water (H ₂ O), mM (5°C,101.325Pa)		0.41	0.53	2.11	4.20	8.21	18.83
Solubility minima in water (H ₂ O), °C		30	50	90	108	110	
ΔS° of solution in H ₂ O at 25°C, J/mol °K (entropy)		- 100.6	-110.1	-128.2	-134.5	-142.2	
ΔG° of solution in H ₂ O at 25°C, kJ/mol (Gibbs free energy)		29.41	29.03	26.25	24.80	23.42	
ΔH° of solution in H ₂ O at 25°C, kJ/mol (enthalpy)		-0.59	-3.80	-11.98	-15.29	-18.99	

(Scharlin et al. (1998), Wikipedia (2007), Stein (1983), Chaplin (2008), and Battino (2006))

Appendix F

Properties of water

RH(%)	T('C)	DP('C)	Water Vapor in air (lb water/ lb dry air)	Water Vapor in air (grain Water vapor/ lb dry air)	RH(%)	T('C)	DP('C)	Water Vapor in air (lb water/ lb dry air)	Water Vapor in air (grain Water vapor/ lb dry air)
10	-1	-26.17	0.00042857	3	50	18	7.43	0.00557143	39
10	4	-22.46	0.00057143	4	50	22	11.11	0.00785714	55
10	10	-18.18	0.00085714	6	50	27	15.7	0.01114286	78
10	18	-12.57	0.00114286	8	50	32	20.28	0.01542857	108
10	22	-9.8	0.00157143	11	50	38	25.76	0.021	147
10	27	-6.38	0.00228571	16	60	-1	-7.02	0.002	14
10	32	-3	0.003	21	60	4	-2.7	0.00257143	18
10	38	1.13	0.00414286	29	60	10	2.6	0.00457143	32
20	-1	-19.1	0.00071429	5	60	18	10.13	0.00685714	48
20	4	-15.17	0.001	7	60	22	13.89	0.00942857	66
20	10	-10.63	0.00142857	10	60	27	18.58	0.01314286	92
20	18	-4.68	0.00228571	16	60	32	23.26	0.01828571	128
20	22	-1.74	0.003	21	60	38	28.87	0.02514286	176
20	27	2.15	0.00428571	30	70	-1	-5.23	0.00242857	17
20	32	6.25	0.006	42	70	4	-0.85	0.00285714	20
20	38	11.15	0.00828571	58	70	10	4.79	0.00542857	38
30	-1	-14.77	0.001	7	70	18	12.45	0.00771429	54
30	4	-10.7	0.00142857	10	70	22	16.28	0.01114286	78
30	10	-6.01	0.002	14	70	27	21.06	0.01542857	108
30	18	0.18	0.00314286	22	70	32	25.84	0.02257143	158
30	22	3.65	0.00485714	34	70	38	31.56	0.02971429	208
30	27	7.96	0.00657143	46	80	-1	-3.66	0.00271429	19
30	32	12.27	0.00928571	65	80	4	0.87	0.00314286	22
30	38	17.41	0.01242857	87	80	10	6.71	0.006	42
40	-1	-11.61	0.00128571	9	80	18	14.5	0.00885714	62
40	4	-7.44	0.002	14	80	22	18.39	0.01257143	88
40	10	-2.63	0.00285714	20	80	27	23.25	0.01785714	125
40	18	4.21	0.00428571	30	80	32	28.11	0.02471429	173
40	22	7.79	0.00628571	44	90	-1	-2.26	0.003	21
40	27	12.26	0.00885714	62	90	4	2.51	0.00342857	24
40	32	16.72	0.01214286	85	90	10	8.44	0.00685714	48
40	38	22.05	0.01657143	116	90	18	16.34	0.01	70
50	-1	-9.1	0.00171429	12	90	22	20.28	0.01428571	100
50	4	-4.85	0.00228571	16	90	27	25.22	0.02	140
50	10	0.06	0.00371429	26	90	32	30.15	0.02785714	195

Table F.1: Water vapor weight in air per dry air weight (Engineering Toolbox 2005)

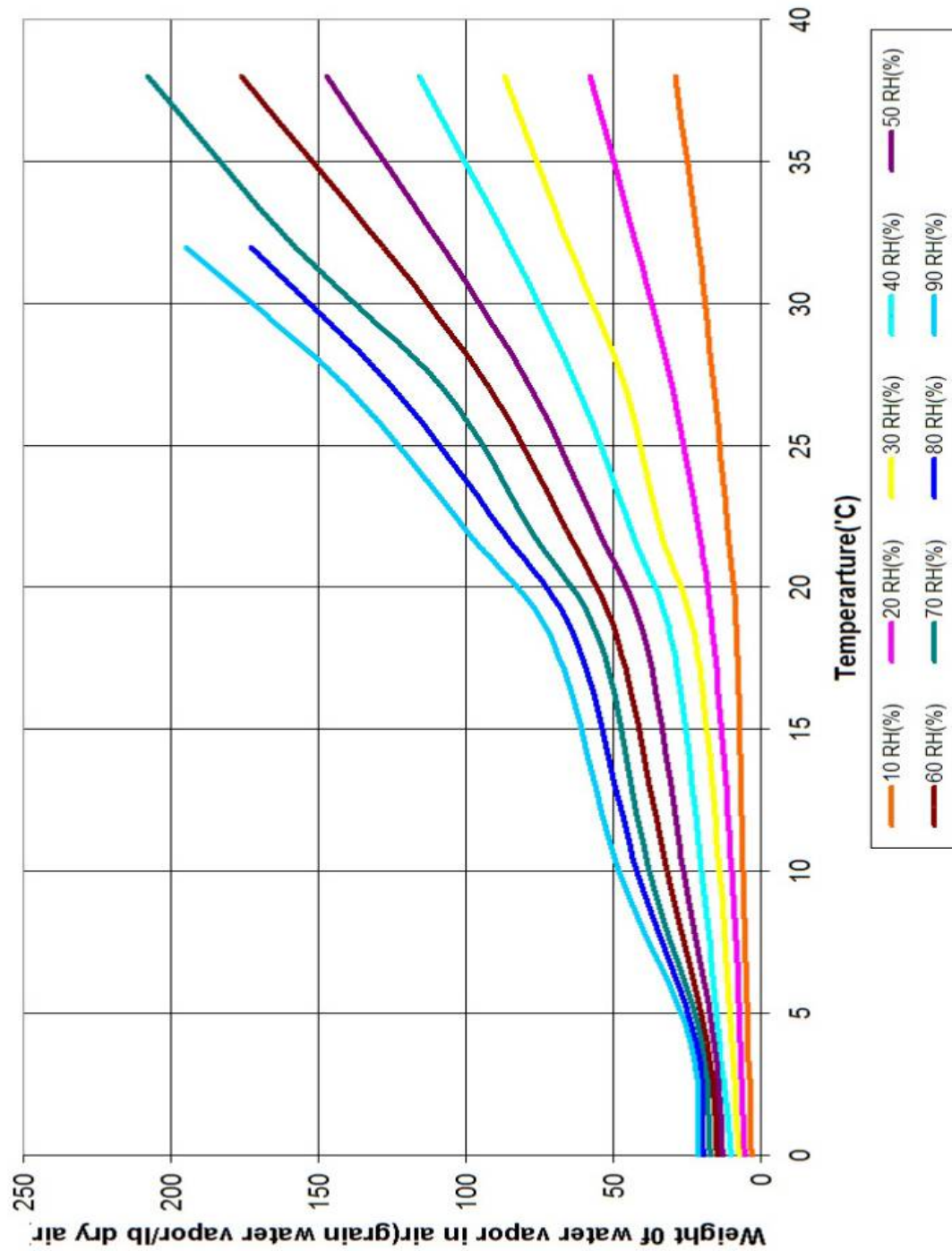


Figure F.1: Weight of water in the air as a function of temperature at different humidities.
(Engineering Toolbox 2005)

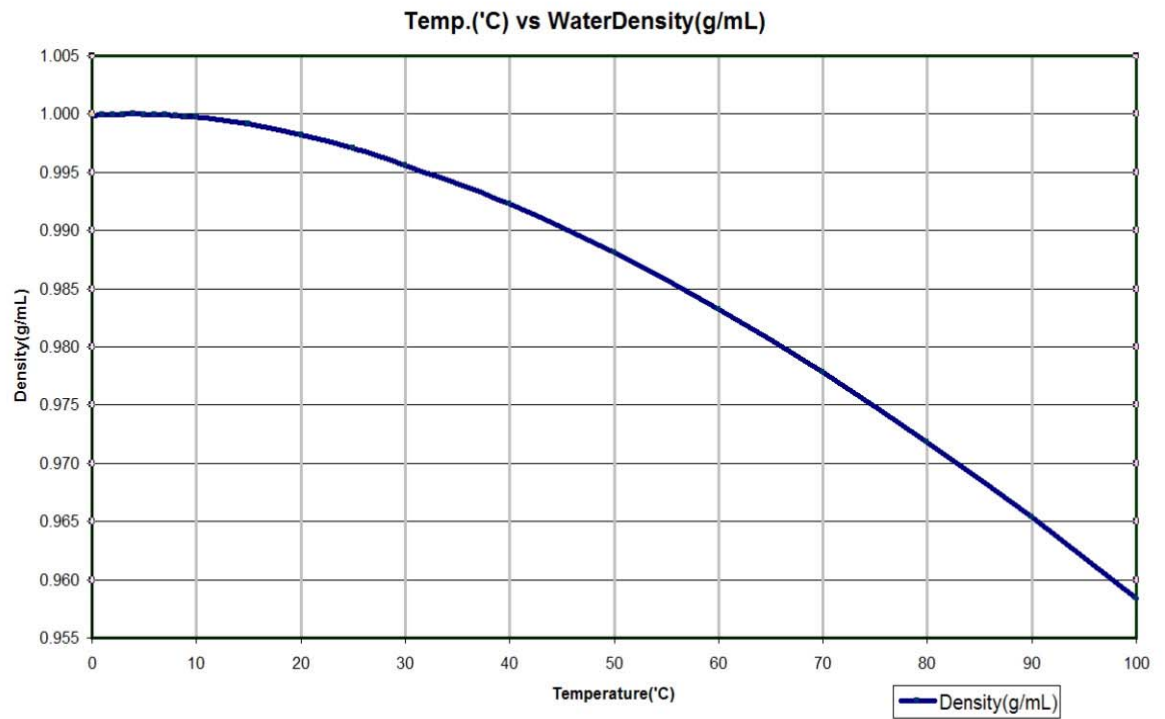


Figure F.2: Water density as a function of Temperature (°C), 0 to 100 °C
(Engineering Toolbox 2005)

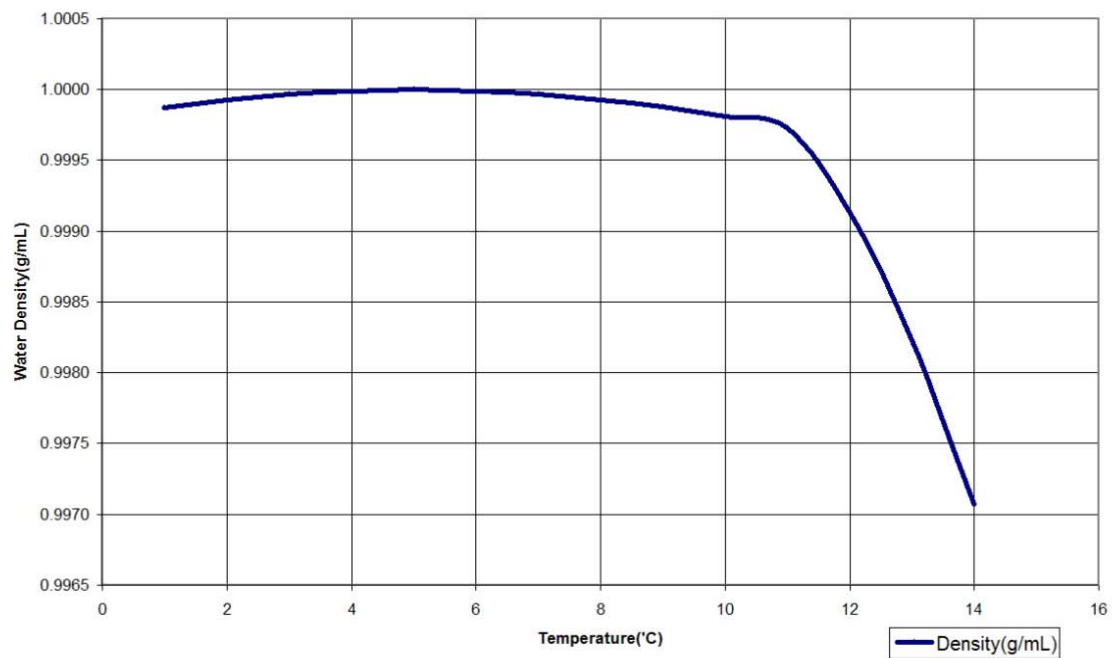


Figure F.3: Water density as a function of Temperature (°C)
(Engineering Toolbox 2005)

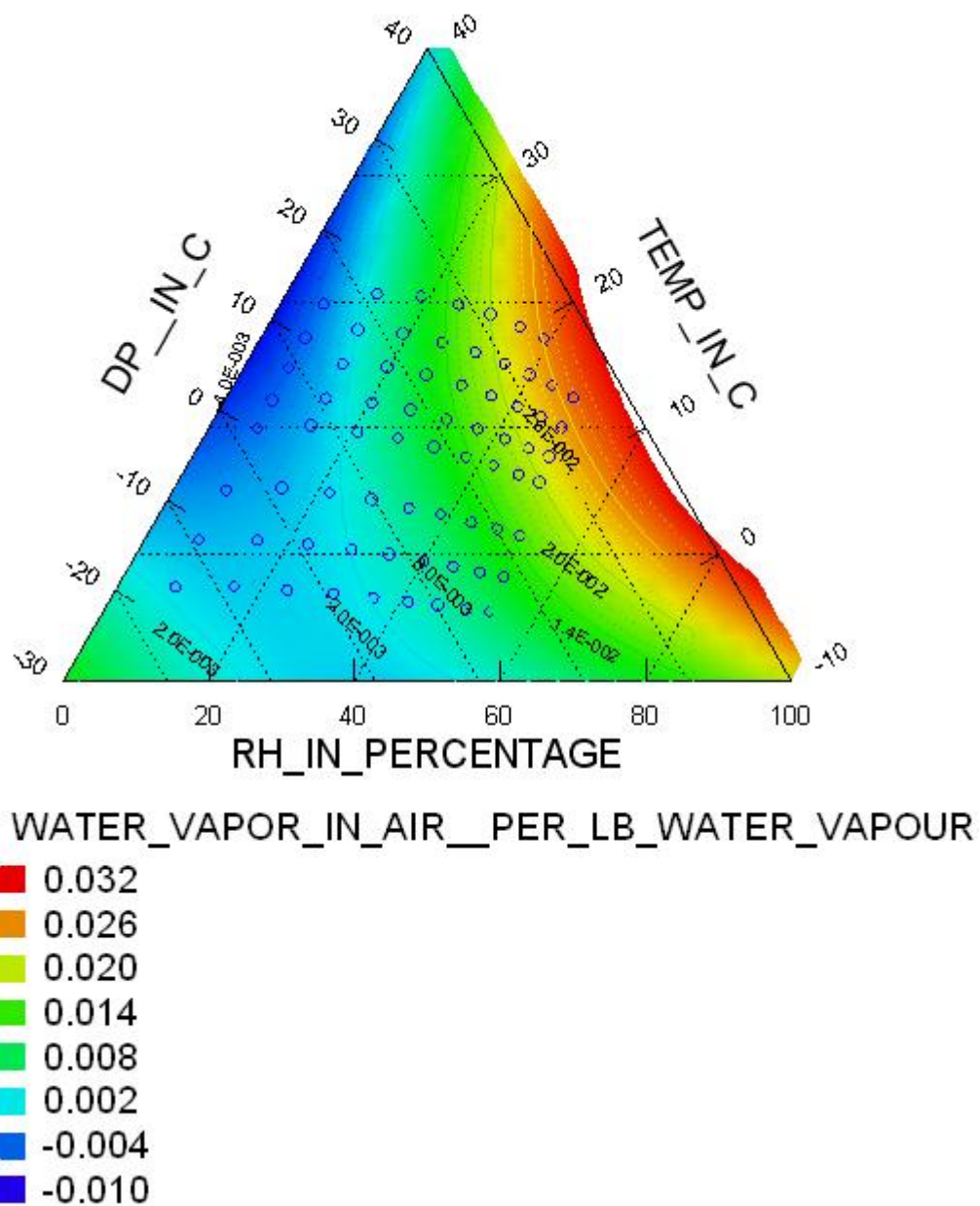


Figure F.4: 4D Pyramid of water vapor weight in grain per lb of air as function of relative humidity (%), temperature (°C) and dew point temperature (°C)

Appendix G

Command File and Output for Calculation of area under the peak of radon ion

```

USE "C:\Documents and
Settings\Administrator\Desktop\SystatGraph\Area_Curves\CH1_out_SYS_PP_Sep2008O
utputFinal2.syz"
USE "C:\Documents and
Settings\Administrator\Desktop\SystatGraph\Area_Curves\SYS_PP_Sep2008TotalFinal
.syz"
IDVAR TIME_MIN
IF case < 1000 THEN
LET NUMBERDATA = case
ENDIF
SELECT (Case <= 999)
LINE CH1AFTERSOURCE_IONS_SEC*NUMBERDATA /xgrid ygrid
LINE CH1AFTERSOURCE_IONS_SEC*TIME_MIN /xgrid ygrid
LINE CH2AFTERDETECTOR_IONS_SEC*NUMBERDATA /xgrid ygrid
LINE CH2AFTERDETECTOR_IONS_SEC*TIME_MIN /xgrid ygrid
LINE CH3BEFORESOURCE_IONS_SEC*NUMBERDATA /xgrid ygrid
LINE CH3BEFORESOURCE_IONS_SEC*TIME_MIN /xgrid ygrid
EXTRACT "C:\Documents and
Settings\Administrator\Desktop\SystatGraph\Area_Curves\CH1_intermed_SYS_PP_Sep2
008TotalFinal.syz"
TRANSPose CH1AFTERSOURCE_IONS_SEC ch2afterdetector_ions_sec
ch3beforesource_ions_sec
LET area_1 = are(col(1)..col(999))
LET p11 = Sum(col(110)..col(190))
LET p12 = Sum(col(191)..col(260))
LET p13 = Sum(col(261)..col(350))
LET p14 = Sum(col(351)..col(430))
LET p15 = Sum(col(431)..col(420))
LET p16 = Sum(col(421)..col(600))
LET filename$ = "SYS_PP_Sep2008TotalFinal.syz"
LET time$= now$('hh:mm:ss mm/dd/yyyy')
DSAVE file1
APPEND file1 "C:\Documents and
Settings\Administrator\Desktop\SystatGraph\Area_Curves\CH1_out_SYS_PP_Sep2008O
utputFinal2.syz"
ESAVE "C:\Documents and
Settings\Administrator\Desktop\SystatGraph\Area_Curves\CH1_out_SYS_PP_Sep2008O
utputFinal2.syz"
PRINT "area_1="
PRINT area_1
LET NEWVAR1=area_1* 6.22
PRINT NEWVAR1
PRINT "NEWVAR1="
PRINT "P11="
PRINT p11
PRINT "P12="
PRINT p12
PRINT "P13="
PRINT p13
PRINT "P14="
PRINT p14
PRINT "P15="
PRINT p15
PRINT "P16="

```

Figure G1: Command File for calculation of area under the curve of radon ion

Figure G2: Output for Calculation of area under the peak of radon ion

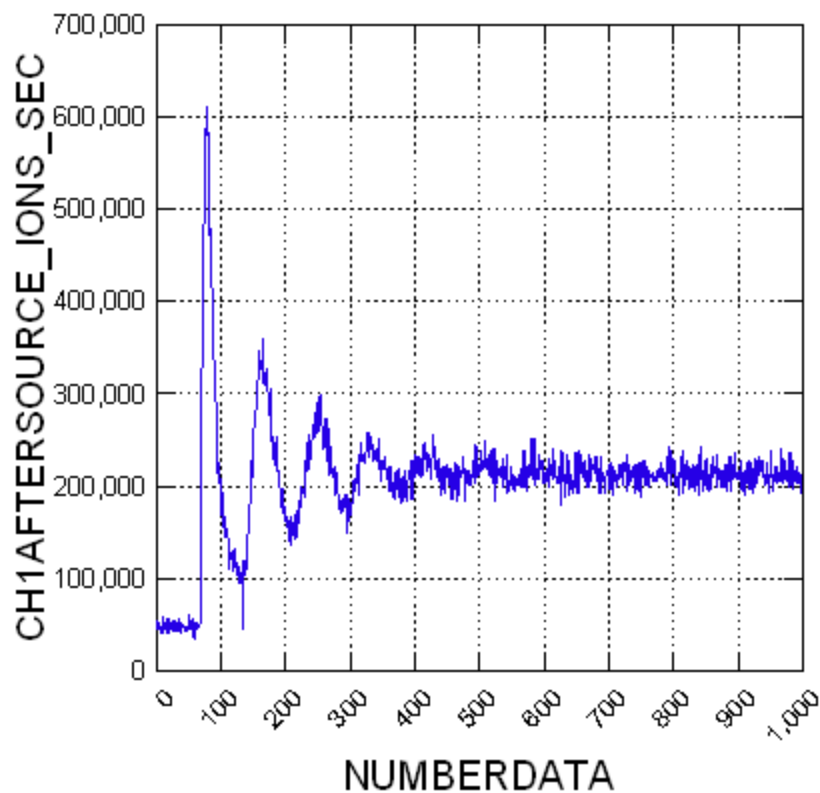
USE "C:\Documents and Settings\Administrator\Desktop\SystatGraph\Area_Curves\CH1_out_SYS_PP_Sep2008OutputFinal2.syz"

▼File: C:\Documents and Settings\Administrator\Desktop\SystatGraph\Area_Curves\CH1_out_SYS_PP_Sep2008OutputFinal2.syz

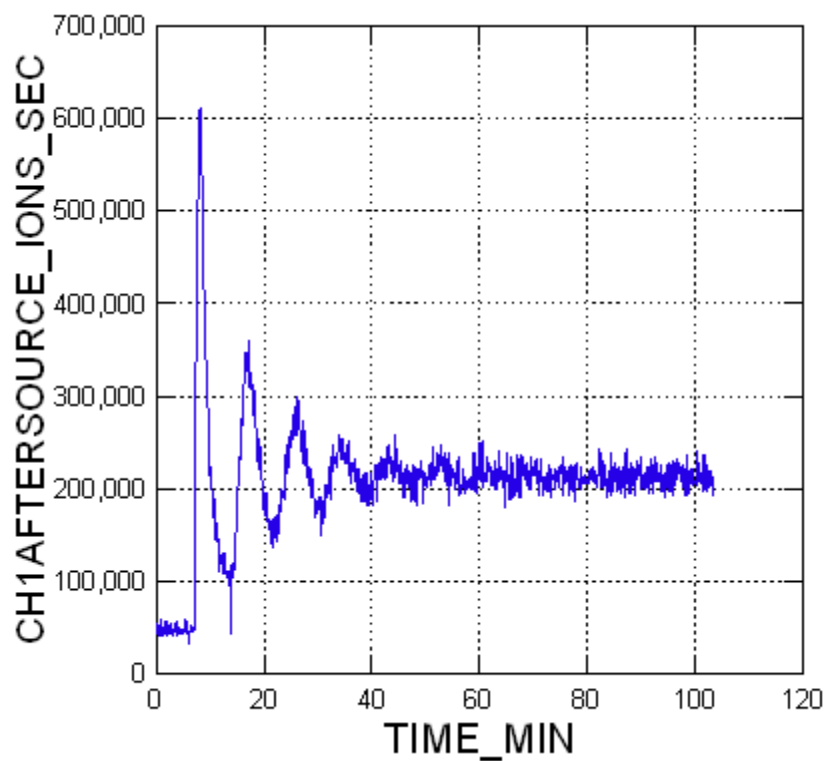
Number of Variables : 1009
Number of Cases : 30

SYSTAT Rectangular file C:\Documents and Settings\Administrator\Desktop\SystatGraph\Area_Curves\CH1_out_SYS_PP_Sep2008OutputFinal2.syz,
created Thu Oct 23 18:50:40 2008, contains variables:

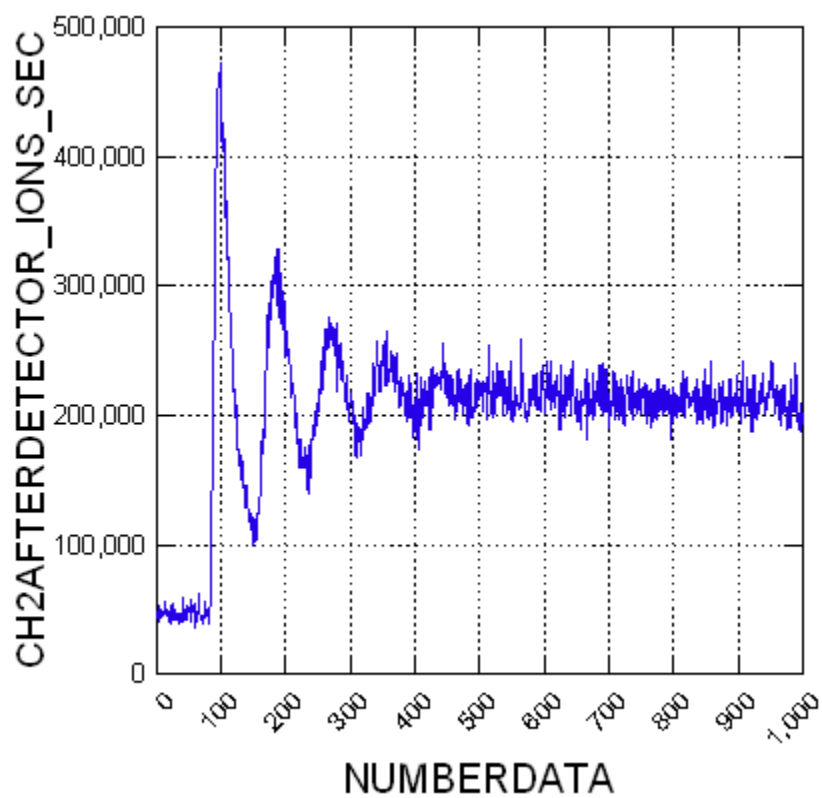
COL(1)	COL(2)	COL(3)	COL(4)	COL(5)	COL(6)
COL(7)	COL(8)	COL(9)	COL(10)	COL(11)	COL(12)
.....					
COL(955)	COL(956)	COL(957)	COL(958)	COL(959)	COL(960)
COL(961)	COL(962)	COL(963)	COL(964)	COL(965)	COL(966)
COL(967)	COL(968)	COL(969)	COL(970)	COL(971)	COL(972)
COL(973)	COL(974)	COL(975)	COL(976)	COL(977)	COL(978)
COL(979)	COL(980)	COL(981)	COL(982)	COL(983)	COL(984)
COL(985)	COL(986)	COL(987)	COL(988)	COL(989)	COL(990)
COL(991)	COL(992)	COL(993)	COL(994)	COL(995)	COL(996)
COL(997)	COL(998)	COL(999)	LABEL\$	AREA_1	P11
P12	P13	P14	P15	P16	FILENAME\$
TIME\$					



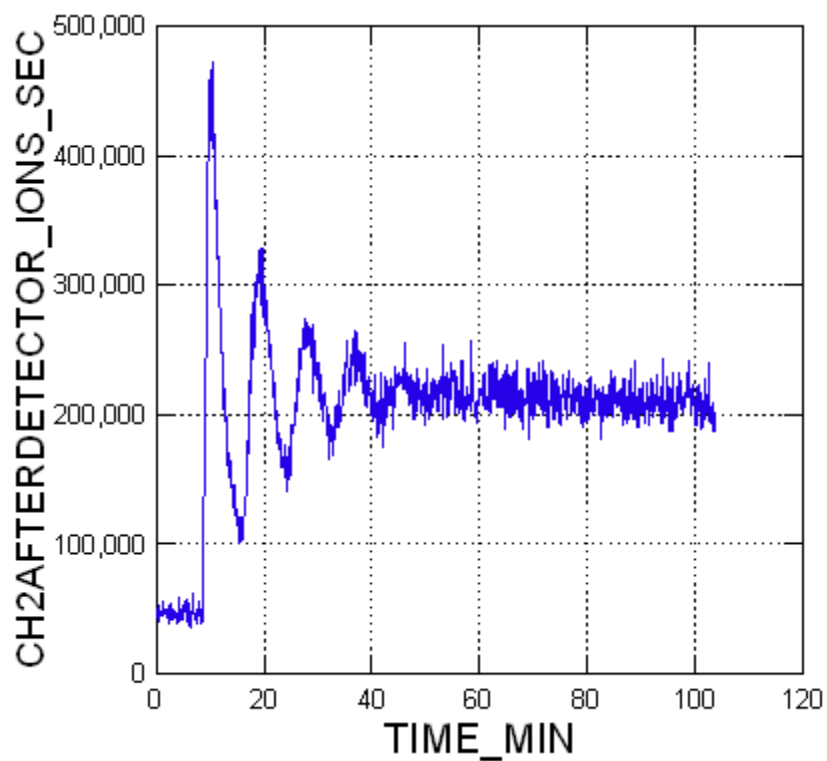
> LINE CH1AFTERSOURCE_IONS_SEC*TIME_MIN /xgrid ygr



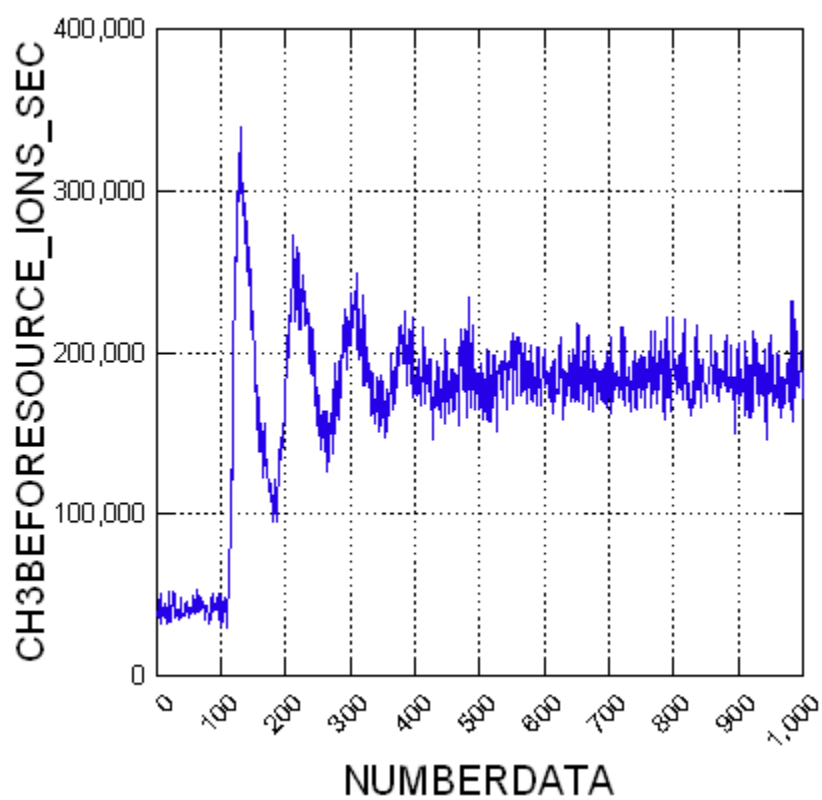
```
> LINE CH2AFTERDETECTOR_IONS_SEC*NUMBERDATA /xgrid ygrid
```



```
> LINE CH2AFTERDETECTOR_IONS_SEC*TIME_MIN /xgrid ygrid
```

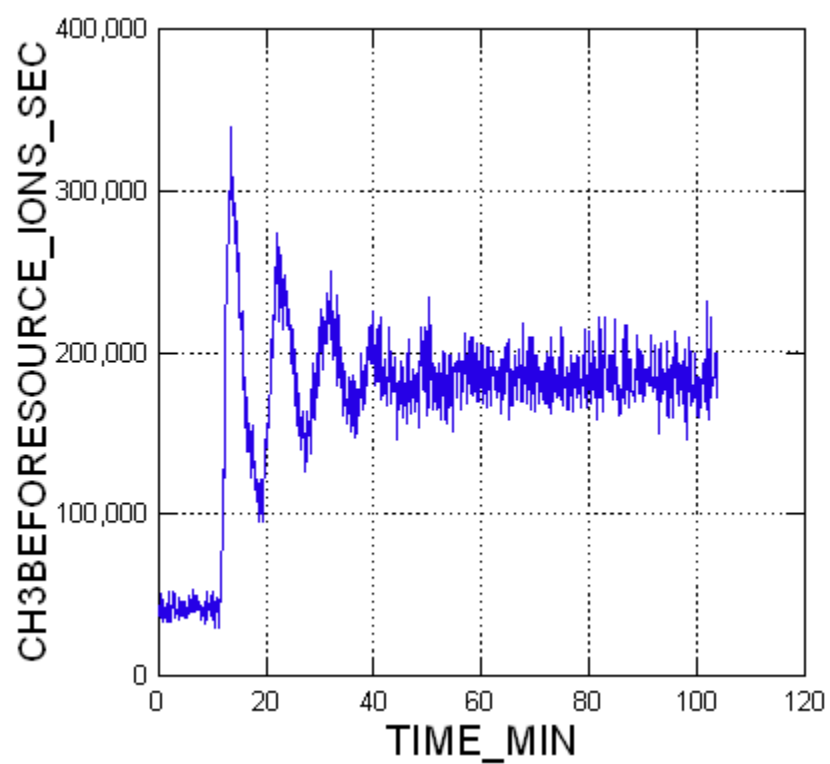


```
> LINE CH3BEFORESOURCE_IONS_SEC*NUMBERDATA /xgrid ygrid
```



```
> LINE CH3BEFORESOURCE_IONS_SEC*TIME_MIN /xgrid ygrid
```

[▼Line Chart](#)



```
> EXTRACT "C:\Documents and  
Settings\Administrator\Desktop\SystatGraph\Area_Curves\CH1_intermed_SYS_PP_Sep2008TotalFi  
nal.syz"
```

References

- Avrorin V V, Krasikova R N, and Nefedov V D, et al (1982) The chemistry of Radon, Russian Chemical Reviews 51(1) (1982) 12-20.
- Bartnikas R, McMahon E J (1987) Engineering Dielectrics: Electrical properties of solids insulating materials: Measurement techniques, Volume IIB, ASTM(STP926), p241-244.
- Battino R (2006) Critical evaluation of radon solubility of water. Private communication
- BEIR (1999) Health effects of exposure to Radon, Commission on Life Science (CLS), BEIR(VI), the Committee on the Biological Effects of Ionizing Radiation (1999).
- Bhadeshia HKDH (2007) Kinetics and microstructure modeling, Material Science and Metallurgy.
- Cember H(1996) Introduction to Health Physics, 3rd ed, McGraw-Hill, 1996, p132
- Chaplin M (2008) Private communication.
- Cohen, BL(1986) Comparison of nuclear track and diffusion barrier charcoal adsorption methods for measurement of Rn²²² levels in indoor air, Health Physics 50 (1986) p828f
- Combs, L L (2008) Private communication.
- Engineering Tool Box (2005) Private communication.
- Fogg PGT and Sangster JM (2003) Chemicals in the Atmosphere: solubility, sources and reactivity, John Wiley and sons, Inc.
- Galla Y (2007) User Manual of Universal Nuclide Chart and Radioactive Decay Applet, Nuclides.net, Institute of Joint Research Centre of the European Commission.
- Glicksman ME and Lupulescu A (2007) Private communication in Multicomponent diffusion (diffusion in solids).
- Grasty RL and LaMarre JR(2004) Natural sources of ionizing radiation in Canada, Radiation Protection Dosimetry 108(2)(2004) p215-226.
- Green A, Humphreys J and Mackenzie R et al (2000) Atomic diffusion in metals and alloys V2.1, Material science, University of Liverpool, UK.
- Hofmann W and Bergmann R (2000) Stochastic modeling of intra-subject variability in particle deposition: Implication for ICRP model predictions, 10th International Congress of International Radiation Protection Association, 14-19 May 2000, Hiroshima, Japan, P3a-126.
- Hyperphysics (2007) Private communication.
- International Commission on Radiological Protection (ICRP) (1977) ICRP publication 26 Annals of the ICRP (1977) 1(3), Oxford, Pergamon Press.
- International Commission on Radiological Protection (ICRP) (1990) ICRP publication 60 Annals of the ICRP (1990) 21(1-3), Oxford, Pergamon Press.
- International Commission on Radiological Protection (ICRP) (1994) ICRP

- publication 65, Protection against Radon-222 at home and at work, Annals of the ICRP (1994) 23(2), Oxford, Pergamon Press.
- International Commission on Radiological Protection (ICRP) (1995) ICRP publication 66, Human respiratory tract model for radiological protection, Annals of the ICRP (1995) 24(1-3), Oxford, Pergamon Press.
- Ishimori Y, Ito K, and Furuta S (2000) Integrating radon progeny monitor, 10th International Congress of International Radiation Protection Association, 14-19 May 2000, Hiroshima, Japan, P6a-282.
- Jostes RF (1996) Genetic, Cytogenetic, and Carcinogenic effects of radon: a review, Mutation research 340(1996)p125-139
- Jha G, Raghavayya M, and Padmanabhan N (1982) Radon Permeability of some membranes, Health Physics (1982) 42(5) p723-725.
- Keller. G, Hoffmann B., Feigenspan T, (2001) Radon permeability and radon exhalation of building materials, The Science of the total environment 272(2001) pp 85-89.
- Kendall G M, Smith T J (2002) Doses to organs and tissues from radon and its decay products, Journal of Radiological Protection 22(2002) p389-406.
- Khan A, Phillips CR and Duport P (1988) The effect of increase in humidity on the size and activity distributions of radon progeny laden aerosols from hydrocarbon combustion, Radiation Protection Dosimetry 22(1) (1988) p39-44.
- Kim IS (2007) Private communication
- Kim IS, Lee IJ, Appleby A, Christman EA, Liepmann MJ and Sigel Jr GH (1995) A new approach to monitoring radon and radon progeny using a glass scintillator in a fiber bundle structure, Nuclear Instruments and Methods in Physics Research A356 (1995) p537-543.
- Kolomeisky AB and Widom B (1999) Model of the hydrophobic interaction; Faraday Discuss 12(1999) p81-89)
- Kotrappa P, Bhanti D P and Raghunath B(1976) Diffusion coefficients for unattached decay products of Thoron-dependence on ventilation and relative humidity. Health Physics (1976) Vol.31, p376-380.
- Lawrence Clever H (1979) Solubility data series Volume 2: Krypton, Xenon and Radon- Gas solubilities, Pergamon Press.
- Lee B (2008) Air ions Counter, Alpha Laboratory, Inc
- Leonard BE (2007) Examination of underground miner data for radon progeny size reduction as a cause of high radon “inverse” dose rate effect. Journal of Health Physics, 93(2)(2007) p133-150.
- Manakov A. Yu. (2000) Investigation of gas hydrates phase behaviour: Modern State and Tendencies. Proceedings of Indo-Russian Joint Workshop on Gas Hydrates Under ILTP, published by Dept. of Ocean development government of India, March 2000, S-5.
- Mazer J J, Stevenson C M, Ebert W L, and Bates J K (1991) The experimental hydration of obsidian as a function of relative humidity and temperature. American Antiquity, 56(3), July 1991, p504-513.

- Morlier JP, Janot M, and Pineau JF et al (1996) Compared deposition of Radon²²² and Radon²²⁰ (thoron) progeny and nuclear aberrations in the respiratory tract of rats after exposure under different aerosol conditions, 9th International Congress of the international Radiation Protection Association, April 1996 , part 2, p44-46.
- National Institute of Standards and Technology (NIST), Physics Laboratory (2007) Private communication
- National Research Council (NRC) (1999a) Committee on Risk Assessment of Exposure to Radon in Drinking Water, in Risk Assessment of Radon in Drinking Water) p82-123.
- National Research Council (NRC) (1999b) Committee on Health risks of exposure to Radon (BEIR VI): Biological effects of ionizing radiation VI, Health effects of exposure to Radon.
- Nuclear Geophysics Division (2007) Radon transport in porous media, Kernfysisch Versneller Institute, University of Groningen, Netherland.
- Porstendorfer J and Mercer T T (1978) Influence of nuclei concentration and humidity upon the attachment rate of atoms in the atmosphere, in Atmospheric Environment, 12(11), 1978, p2223-2228.
- Porstendorfer J, Robig G , and Ahmed A (1979) Experimental determination of the attachment coefficient of atoms and ions on mono-disperse aerosols. Journal of Aerosol Science 10 (1979) p 21-28.
- Roy M (1996) Dosimetry of the respiratory tract, 9th International Congress of the international Radiation Protection Association, April 1996, part 1, p153-159.
- Satomi K and Kruger P (1982) Radon emanation mechanism from finely ground rocks, Stanford Geothermal Program Interdisciplinary Research in Engineering and Earth Sciences, Stanford University, Stanford, California SGP-TR-63, October 1982.
- Scharlin P, Battino R, and Silla E, et al (1998) Solubility of gases in water: Correlation between solubility and the number of water molecules in the first solvation shell., Pure & Appl.Chem. 70(10)(1998) p1895-1904.
- Sonntag D (1990) Important new values of physical constants of 1986, vapour pressure formulations based on the ITS-90 and Psychrometer Formulae; Z. Meteroly 70(1990) 5, p340-344.)
- Stein L (1983) The chemistry of Radon, Radiochimica Acta 32 (1983) 163-171.
- Surbeck H (1996) A Radon-in-water monitor based on fast gas transfer membranes, in Int. Conf. on Technologically Enhanced Natural Radioactivity (TENR) caused by non-uranium mining, October 16-19,1996, Szczyrk, Poland.)
- Tsoufanidis N, Measurement and detection of Radiation., Hemisphere Publishing Corp. 1983 p126-128)
- Tsymbal E Y (2008) Private communication.
- Valentin B (2002) Deposition in the respiratory tract; Annals of ICRP 32, March (2002) p41.

- Vojtek T, Skoupil T, Fiala P, and Bartusek K (2006) Accuracy of Air Ion Field Measurement, Progress in Electromagnetics Research Symposium 2006, Cambridge, USA, March 26-29, 2006, p412-415.
- Welch K M (2001) Capture Pumping Technology, Elsevier
- Wikipedia (2007) Private communication.
- Wilson CTR (1900) Philos.Trans.Soc.(London) A193 (1900) p289.
- Yamada Y, Furukawa M, and Fukutsu K et al (2004) Performance of radon/aerosol chamber at NIRS, Japan. 11th International Congress of the International Radiation Protection Association, 23-28 May, 2004, Madrid, Spain.
- Yu C, Loureire C and Cheng JJ et al (1993a) Effective radon diffusion coefficient in Data collection handbook to support modeling impacts of radioactive material in soil, Chapter 7, US DOE
- Yu C, Loureiro C, and Cheng JJ (1993b) Data collection handbook to support modeling: Impacts of radioactive material in soil, US Department of Energy, Argonne National Laboratory, Argonne, Illinois

VITA
Sombun Reantragoon

1952	Born Bangkok, Thailand
1971	Diploma (Science), Bangkok Christian College, Bangkok, Thailand
1976	B.Sc. (Physics), Mahidol University, Bangkok, Thailand
1979	Postgraduate Diploma (Medical Physics) University of Surrey, Guildford, England
1985	M.Phil (Medical Physics) University of Leeds, Leeds, England
1986-1989	employed as Research and Teaching Specialist Robert Wood Johnson Medical School, UMDNJ, New Brunswick, New Jersey
1989-1995	employed as Clinical and Teaching Specialist University Hospital, UMDNJ, Newark, New Jersey
1997-2005	employed as Radiation Oncology Physicist/Medical Physicist Ocean Radiation Therapy Center, Toms River, New Jersey
1997-2005	employed as Radiation Oncology Physicist/Medical Physicist NJ Diagnostic and Therapy, Brick, New Jersey
2003	licensed as Medical Physicist-Therapeutic Radiological State of New York
2005	qualified as Radiological Medical Physicist- Therapeutic State of New Jersey
2005	employed as Radiation Oncology Physicist/Medical Physicist Center for Advanced Radiation Oncology, Toms River, New Jersey
2005-Present	employed as Radiation Oncology Physicist/Medical Physicist Medical Physics of New Jersey, Consulting at Radiation Oncology Department, James J Peters Veterans Affairs Medical Center, Bronx, New York